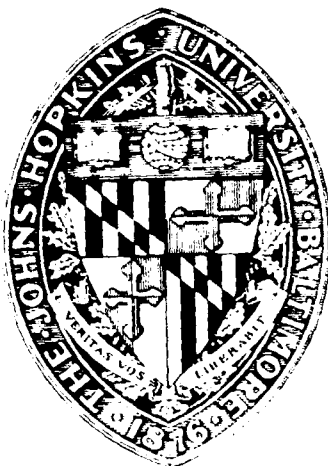


2



THE INVESTIGATION OF THE FUNDAMENTAL LIMITS
OF HETERODYNE HOLOGRAPHIC INTERFEROMETRY
WITH THE APPLICATION OF
IMAGING LASER GENERATED LAMB WAVES

Louis C. Phillips and James W. Wagner, Ph.D. of the
Materials Science and Engineering Department
The Johns Hopkins University
Baltimore, Maryland 21218

TECHNICAL REPORT

ONR CONTRACT N00014-82-K-0741-PO4

FULL FIELD VISUALIZATION OF
SURFACE ACOUSTIC WAVES

September 1986

Prepared for

The Office of Naval Research

Physics Division, Code 1112

Arlington, Virginia 22217-5000

DTIC
ELECTE
AUG 9 1989
S B D



| REPORT DOCUMENTATION PAGE | | | | Form Approved OMB No. 0704-0188 | |
|---|-------|---|--|------------------------------------|-------------------------------------|
| 1a. REPORT SECURITY CLASSIFICATION Unclassified | | | 1b. RESTRICTIVE MARKINGS | | |
| 2a. SECURITY CLASSIFICATION AUTHORITY ELECTED AUG 09 1989 | | | 3. DISTRIBUTION/AVAILABILITY OF REPORT Approved for public release; distribution unlimited | | |
| 2b. DECLASSIFICATION/DOWNGRADING SCHEDULE | | | 5. MONITORING ORGANIZATION REPORT NUMBER(S) | | |
| 4. PERFORMING ORGANIZATION REPORT NUMBER(S) | | | 5. MONITORING ORGANIZATION REPORT NUMBER(S) | | |
| 6a. NAME OF PERFORMING ORGANIZATION The Johns Hopkins University | | 6b. OFFICE SYMBOL (If applicable) | 7a. NAME OF MONITORING ORGANIZATION Office of Naval Research | | |
| 6c. ADDRESS (City, State, and ZIP Code) Dept. of Materials Science & Engineering 102 Maryland Hall Baltimore, Maryland 21218 | | 7b. ADDRESS (City, State, and ZIP Code) Physics Division, Code 1112 800 North Quincy Street Arlington, Virginia 22217-5000 | | | |
| 8a. NAME OF FUNDING/SPONSORING ORGANIZATION | | 8b. OFFICE SYMBOL (If applicable) | 9. PROCUREMENT INSTRUMENT IDENTIFICATION NUMBER N00014-82-K-0741-P04 | | |
| 8c. ADDRESS (City, State, and ZIP Code) | | 10. SOURCE OF FUNDING NUMBERS | | | |
| | | PROGRAM ELEMENT NO. 61153N.11 | PROJECT NO. | TASK NO. 4126-813 | WORK UNIT ACCESSION NO. |
| 11. TITLE (Include Security Classification) The Investigation of the Fundamental Limits of Heterodyne Holographic Interferometry with the Application of Imaging Laser Generated Lamb Waves | | | | | |
| 12. PERSONAL AUTHOR(S) Louis C. Phillips and James C. Wagner | | | | | |
| 13a. TYPE OF REPORT Technical | | 13b. TIME COVERED FROM 8706 TO 8904 | 14. DATE OF REPORT (Year, Month, Day) 4/89 | | 15. PAGE COUNT 151 |
| 16. SUPPLEMENTARY NOTATION | | | | | |
| 17. COSATI CODES | | | 18. SUBJECT TERMS (Continue on reverse if necessary and identify by block number) | | |
| FIELD | GROUP | SUB-GROUP | | | |
| 11 | 11/06 | 11/06/01 | Holography; Holographic Interferometry; High Resolution Interferometry; High Speed Holography; Surface Acoustic Waves; Acoustic Wave Visualization | | |
| 19. ABSTRACT (Continue on reverse if necessary and identify by block number) | | | | | |
| <p>Currently, the field of ultrasonic nondestructive testing uses primarily piezoelectric transducers for both the generation and detection of acoustic waves. However, contact transducers have several shortcomings that have inhibited their use in some applications. The major weakness of piezoelectric transducers is that they must be in physical contact with the specimen. There are many situations where direct contact is not desirable, and in some cases, not possible. An alternate technique which has been explored and developed in this manuscript is the application of holographic interferometry to imaging acoustic waves.</p> <p>Past acoustic studies, involving holographic interferometry as the inspection tool, have been restricted to large amplitude waves with displacements on the order of the wavelength of light. In this treatise, heterodyne and quasi-heterodyne phase measurement techniques were employed to achieve the necessary resolution in order to image sub-fringe events. As previous researchers have shown, heterodyne holographic interferometry (HHI) can be a</p> | | | | | |
| 20. DISTRIBUTION/AVAILABILITY OF ABSTRACT <input checked="" type="checkbox"/> UNCLASSIFIED UNLIMITED <input type="checkbox"/> SAME AS RPT <input type="checkbox"/> DTIC USERS | | | 21. ABSTRACT SECURITY CLASSIFICATION UNCLASSIFIED | | |
| 22a. NAME OF RESPONSIBLE INDIVIDUAL L. E. Hargrove, ONR Physics Division | | | 22b. TELEPHONE (Include Area Code) (202) 696-4221 | | 22c. OFFICE SYMBOL ONR Code 1112 |

Block 19 continued powerful technique in the accurate measurement of imaging full field object displacements. However, previous experimental obstacles have made HHI an impractical method for ultrasonic measurement on a diffusely reflecting surface, a requirement to make HHI a practical method in ultrasonic nondestructive testing. In this body of work, theoretical obstacles were investigated and preliminary experiments were conducted to make the final experiment possible - demonstrating the imaging of a laser generated acoustic wave with sub-fringe displacements amplitudes. This treatise demonstrates that it is possible to use heterodyne holographic interferometry as a broad range non-contact ultrasonic measurement technique with the ability to image standard acoustic source events.

| | |
|--------------------|--|
| Accession For | |
| NTIS GRA&I | <input checked="checked" type="checkbox"/> |
| DTIC TAB | <input type="checkbox"/> |
| Unannounced | <input type="checkbox"/> |
| Justification | |
| By | |
| Distribution/ | |
| Availability Codes | |
| Avail and/or | |
| Dist | Special |
| A-1 | |



**THE INVESTIGATION OF THE FUNDAMENTAL LIMITS
OF HETERODYNE HOLOGRAPHIC INTERFEROMETRY
WITH THE APPLICATION OF
IMAGING LASER GENERATED LAMB WAVES**

**Louis C. Phillips and James W. Wagner, Ph.D. of the
Materials Science and Engineering Department
The Johns Hopkins University
Baltimore, Maryland 21218**

TECHNICAL REPORT

ONR CONTRACT N00014-82-K-0741-PO4

**FULL FIELD VISUALIZATION OF
SURFACE ACOUSTIC WAVES**

September 1986

Prepared for

The Office of Naval Research

Physics Division, Code 1112

Arlington, Virginia 22217-5000

Abstract

Currently, the field of ultrasonic nondestructive testing uses primarily piezoelectric transducers for both the generation and detection of acoustic waves. However, contact transducers have several shortcomings that have inhibited their use in some applications. The major weakness of piezoelectric transducers is that they must be in physical contact with the specimen. There are many situations where direct contact is not desirable, and in some cases, not possible. An alternate technique which has been explored and developed in this manuscript is the application of holographic interferometry to imaging acoustic waves.

Past acoustic studies, involving holographic interferometry as the inspection tool, have been restricted to large amplitude waves with displacements on the order of the wavelength of light. In this treatise, heterodyne and quasi-heterodyne phase measurement techniques were employed to achieve the necessary resolution in order to image sub-fringe events. As previous researchers have shown, heterodyne holographic interferometry (HHI) can be a powerful technique in the accurate measurement of imaging full field object displacements. However, previous experimental obstacles have made HHI an impractical method for ultrasonic measurement on a diffusely reflecting surface, a requirement to make HHI a practical method in ultrasonic nondestructive testing. In this body of work, theoretical obstacles were investigated and preliminary experiments were conducted to make the final experiment possible - demonstrating the imaging of a laser generated acoustic wave with sub-fringe displacements amplitudes. This treatise demonstrates that it is possible to use heterodyne holographic interferometry as a broad range non-contact ultrasonic measurement technique with the ability to image standard acoustic source events.

TABLE OF CONTENTS

| | |
|--|-----|
| Abstract | ii |
| Acknowledgements | iii |
| 1. Introduction | 1 |
| 2. Laser Generation of Ultrasound | 9 |
| 3. Holography | 22 |
| .1 Holographic Interferometry | 27 |
| .2 Heterodyne Holographic Interferometry | 32 |
| .3 Quasi-heterodyne Interferometry | 40 |
| 4. Imaging a Diffuse Object | 45 |
| .1 Experimental Measurement of Intensity | 54 |
| 5. Interferometry of Diffuse Objects | 59 |
| .1 Heterodyne Intensity | 62 |
| .2 Statistical Phase Intensity | 64 |
| 6. Misalignment of the Holographic Images | 70 |
| 7. Film Effects | 80 |
| .1 Exposure Characteristics | 80 |
| .2 Non-Linear Considerations | 83 |
| .3 Resolution Limitations | 87 |
| 8. Experimental Design | 91 |
| .1 Real Time Heterodyne Holographic Interferometry | 92 |
| .2 CW Double Exposure Heterodyne Holographic Interferometry | 94 |
| .3 Double Exposure Pulsed Holographic Interferometry | 97 |
| .4 Interferometric Detection of a Laser Generated Ultrasound | 100 |
| .5 Full Field Imaging of a Laser Generated Lamb Wave | 103 |

| | |
|---|-----|
| 9. Experimental Results | 112 |
| .1 Real Time Heterodyne Holographic Interferometry | 112 |
| .2 CW Double Exposure Heterodyne Holographic Interferometry | 113 |
| .3 Double Exposure Pulsed Holographic Interferometry | 117 |
| .4 Interferometric Detection of Laser Generated Ultrasound | 117 |
| .5 Full Field Imaging of Laser Generated Lamb Wave | 119 |
| 10. Conclusion | 129 |
| 11. References | 131 |
| 12. Appendix | 134 |
| Vita | 145 |

1 Introduction

Currently, the field of ultrasonic nondestructive testing uses primarily piezoelectric transducers for both the generation and detection of acoustic waves. Ferroelectric crystals and natural piezoelectrics are typically employed in such techniques since they offer excellent sensitivity at a reasonable price. These transducers can be widely applied in a variety of configurations to make ultrasonic attenuation and velocity measurements. Data from these measurements leads directly to information concerning the material properties of a specimen. This information would include an accurate assessment of the integrity of the material along with the size and location of defects. However contact transducers have several shortcomings that have inhibited their use in some applications.

The common reason for most these shortcomings is that a piezoelectric transducer must be in physical contact with the specimen. There are many situations where direct contact is not desirable, and in some cases, not possible. The bonding or coupling of piezoelectric transducers is generally the root of most of these problems. The glues, gels or oils used in the acoustical connection between the specimen and the transducer can lead to incorrect attenuation and time of flight measurements. For velocity measurements, the time of arrival is very critical, and variations in the coupling thickness between successive measurements can be a large source of error. Also, the couplant can alter the nature of the waveform because of reflections and refractions in this layer. This could adversely affect both velocity measurements but especially the attenuation measurements. It is probably for these reasons most people in this field find the transducer coupling process to be as much an art as a science. Secondly, the local transducer environment presents a formidable problem. There may be occasions where direct contact with the specimen is not possible because of contamination considerations or because of an environment

hostile to the transducer. For example, from a manufacturing stand point, it would be advantageous to locate flaws and defects while a part was still at an elevated temperature facilitating an easy correction. However, such temperatures are typically above the acceptable operating temperature of piezoelectric transducers. More and more, the need for a remote non-contact generation and detection schemes are needed to provide on line inspection while also avoiding the coupling problems.

The benefits of a laser generation and detection system have long been realized for this application and made the goal of many research efforts (Bonderanko et.al. 1976; Scruby et.al. 1982; Calder & Wilcox 1980). It offers the ability to perform remote ultrasonic inspection without making actual contact with the specimen. A high energy pulsed laser is focused on to a specimen, where rapid local thermal expansion generates an acoustic pulse (Hutchins 1988). Detection of the pulse has been accomplished by numerous groups using a variety of interferometry techniques (Cielo 1985; Palmer & Green 1977 ; Jungerman et.al 1983; Monchalin 1986). The sensitivity for most of these techniques is approximately $10^{-15} \text{ mHz}^{-\frac{1}{2}}$, which is adequate for acoustic detection. This is not to say, however, that optical detection is on par with piezoelectric transducers for ease of operation or expense. Most interferometers have tedious alignment procedures and only a few do not require some type of surface preparation (Monchalin 1986. Jungerman et.al. 1983). Despite some of these shortcomings, it still seems to offer a promising solution to remotely measuring ultrasound. Other remote detection schemes such as capacitance transducers or EMAT's have been employed, but must remain in close proximity to the sample surface, solving the coupling problem in some instances, but not truly remote. A technique which has been explored and developed in this manuscript is the application of holographic interferometry to imaging acoustic waves.

Holographic interferometry has long been applied to deformation analysis and nondestructive testing. In these areas, holography has excelled because it is able to image object deformations in the full field and provide valuable information in complex analysis problems where typical displacement transducer techniques are inappropriate. Through holography, a spatial position of a deformed object can be recorded and then interferometrically compared to a previously recorded reference state. When a single hologram plate is used for both recordings, it is referred to as a double exposure hologram. After developing the double exposure hologram, the reconstructed images are formed by illuminating the film plate with coherent light from a laser. The resultant coherent image is a superposition of the two states of the object. Constructive and destructive interference will occur corresponding to the amount of displacement that has occurred in a particular region. This produces the characteristic fringe pattern often observed in holographic interferometry. This fringe pattern is equivalent to a contour map where successive contours or fringes are a measure of elevation changes of half-wavelength increments. For the purpose of acoustic studies, a double exposure hologram is produced using a high energy pulsed laser that freezes the motion of the propagating acoustic wave (Aprahamian et.al. 1971, Gogosz 1974, Holloway et.al 1977). Mapping the acoustic disturbance is as simple as observing the fringe pattern formed in the reconstructed image. This fringe pattern is a full field mapping and is a measure of the out-of-plane displacements of the propagating wave on the object surface. An elementary analogy would be that of throwing a pebble into a pond and then watching the ripples move outward. From this ripple pattern, information about a material's homogeneity and elastic properties could be ascertained. Anisotropic materials would produce an irregular shaped fringe pattern corresponding to the respective symmetry axes. If

the wavefront or ripple were to encounter a defect, the defect would alter the propagation characteristics of the wave either through diffraction, reflections, or mode conversion. Hence, such analysis could greatly aid in the study of defect interaction with acoustic waves, materials characterization, mode conversions at interfaces, and standardization of acoustic sources.

Much of the stimulus behind this manuscript has been the interest to develop a full field imaging technique to assist in the study of acoustic wave propagation. However, past acoustic studies, involving holographic interferometry as the inspection tool, have been restricted to large amplitude waves with displacements on the order of the wavelength of light, $> 600\text{nm}$. These large amplitude waves were needed since the resolution of normal holographic interferometry is about a quarter of a wavelength or approximately 150nm . A sensitivity that would be too coarse to resolve standard acoustic sources with displacements ranging $0.001\text{-}10.0\text{nm}$. Hence, the impetus in this project has been to improve the sensitivity of holographic interferometry enough to quantitatively map laser generated acoustic waves. The use of heterodyne and quasi-heterodyne signal processing techniques have been shown to achieve an out of plane displacement resolution of 0.25nm for holographic interferometry. This sensitivity limit would enable the imaging of acoustic waves in the full field using holographic interferometry. Feasibility for such an experiment has been shown by Wagner, but accomplishing this goal proved to be difficult mainly owing to poor optical components and a wavelength shift introduced by the different lasers needed for the hologram construction and reconstruction process (Wagner 1984). The thrust behind this treatise has been to directly address and solve these experimental difficulties as well as investigate the fundamental design limits of heterodyne holographic interferometry.

Heterodyne and quasi-heterodyne methods are precise phase measurement

techniques that greatly improve the sensitivity of holographic interferometry. This improvement is accomplished by introducing a phase shift between the two interfering images with the addition of a few optical elements to the original holographic system. In the heterodyne case, the phase shift is continuous and the two images are modulated at the particular beat frequency. A detector is scanned across the image measuring the relative phase shifts with respect to a fixed reference signal. These measured phase shifts corresponds to the out of plane displacements that have occurred. The accuracy of this type of phase measurement using off the shelf electronics is better than 0.3 degrees. A displacement of $\lambda/2$ corresponds to a full fringe of deformation or 360 degrees, so 0.3 degrees of phase accuracy establishes a displacement resolution of better than $\lambda/2000$. Quasi-heterodyne is a computed phase measurement technique. The relative phase between the two interfering images is changed step wise in equal increments and the intensity patterns are recorded with a TV camera. The actual phase difference, or displacement, between the two images can be calculated out of solving a few trigonometric identities. The advantages of quasi-heterodyne is that it can grab intensity data at TV frame rates and does not require any scanning mechanism. However, it does suffer from a small reduction in sensitivity, a resolution of approximately $\lambda/200$. Both methods have been shown to be successful at imaging acoustic disturbances.

The resolution limit of heterodyne holographic interferometry has been found to be approximately $\lambda/2000$. However, this limit is not a restriction of the electronic instrumentation, but is rather an optical engineering design problem that is a function of three parameters: the optical resolution of the imaging system, the maximum acceptable spatial dimension of the optical detector, and the degree of registry between the two superimposed images. The optical resolution determines a

quantity called the average speckle size. The speckle size is analogous to the minimum resolvable spot size from incoherent imaging. However, coherent imaging produces an image that is granular in appearance rather than smooth and uniform. This speckle pattern is really an interference phenomenon owing to the coherent nature of the light. The average size of these speckles or grains is dependent upon the f-number or resolution of the imaging system; a smaller f-number leads to a smaller speckle size. The average speckle size is an important parameter because it directly effects the phase error or the certainty of the displacement measurement. A statistical analysis reveals that the phase error is reduced when the number of speckles on the active detector area is increased. This could be accomplished by increasing the detector area or by decreasing the speckle size. Obviously, when the detector area is increased one tends to forfeit spatial resolution. The other alternative would be to reduce the speckle size using larger optics. However, the phase error is also dependent upon the registry of the two granular images. Proper alignment requires that identical speckles from the respective images be overlapped in order to produce interference. Decreasing the speckle size eventually results in reducing the image registry and thus increasing the phase error. Optimization becomes a series of trade offs in order to achieve the proper balance for the desired displacement resolution. Experimentally, one could expect to experimentally achieve an image correlation of 70% for a $f/\#5$ imaging system, which results in a minimum detector diameter of 0.5mm. So, the rms phase error for such a system would be approximately 0.36 degrees, which corresponds an out of plane displacement resolution of 0.26nm for a working wavelength of 514.5nm. Combined these three parameters dictate the certainty of the displacement measurement and altering one parameter can adversely change another.

This design process, however, is complicated by the necessity to employ two

different optical configurations for the hologram construction and reconstruction processes. The application of holographic interferometry to imaging high speed events required the use of a pulsed Nd:YAG laser for the hologram construction and a continuous wave Argon ion laser for the read-out system. The wavelength difference between these two lasers resulted in a lateral image shift as well as image magnification which caused the reconstructing wavefronts to be improperly matched. It was discovered that these obstacles could be overcome if the proper attention was given to the collimating optics and reference beam quality. This required the deviation in wavefront curvatures to be less than $\lambda / 10$. This wavefront matching requirement places a premium on optical component quality and laser beam uniformity. Most theory involving the reconstructing optics assumes perfectly collimated wavefronts. If this were truly the case, no experimental problems would occur. However, anytime a switch in lasers or optical set-ups is necessary the wavefront quality becomes paramount. As was demonstrated in this study, particular attention must be paid to congruency of the respective optical configurations in order to sufficiently meet the design criteria; in this case, it was imaging laser generated ultrasound.

Laser generation of ultrasound was chosen as a complement to the remote detection capabilities of heterodyne holographic interferometry. Laser generation mechanisms have been well established and characterized at various power levels. The amplitudes of the different generated modes depends upon which mechanism is operational and the particular specimen geometry. In laser generation, the three modes that are produced in a semi-infinite half space are the longitudinal wave, the shear wave and the Rayleigh wave spike. The Rayleigh wave is present owing to the free surface constraint on the boundary conditions. Lamb waves are another wave type that are precipitated from the boundary conditions and are found to propagate

in plates. These waves were particularly applicable for this study owing to their dispersive nature and the variable amplitudes that are found at different frequencies. The higher frequency Lamb waves tend to travel at higher velocities and smaller amplitudes. Thus, for a single laser excitation, one could produce numerous waves of different wavelengths and amplitudes providing an excellent means by which to calibrate the holographic system.

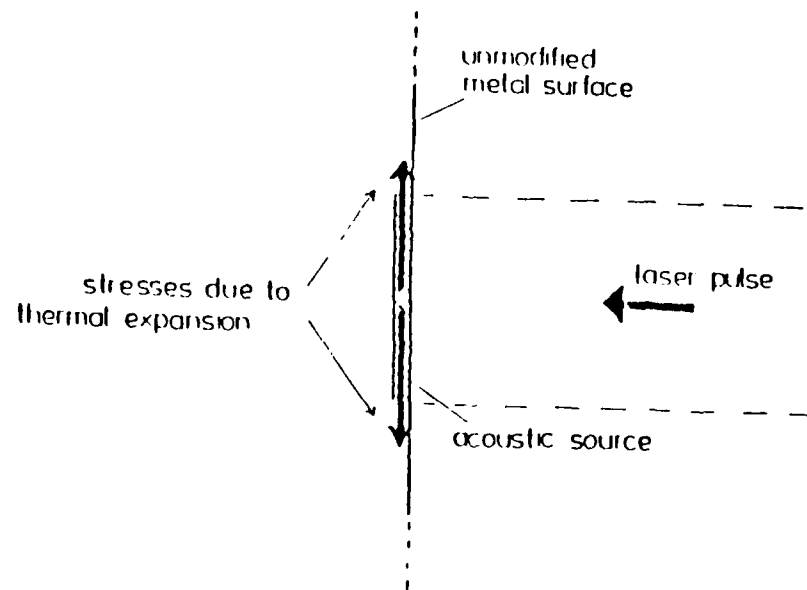
The underlying objective behind any ultrasonic detection scheme is to measure or map the propagating acoustic wave. The behavior of this propagating acoustic wave reveals information about a specimens integrity and material properties. In this treatise, for the first time, heterodyne holographic interferometry has been successful at imaging purely sub-fringe acoustic events. The acoustic source in this study was a laser generated acoustic wave demonstrating the feasibility for remote a generation and detection of low amplitude transient events. While this technique is not likely to replace the piezoelectric transducer, it does provide an attractive alternative in some situations. One clear advantage is that it is a non-contact method, eliminating any coupling problems, and could operate in hostile environments. As in other interferometric detection techniques, it measures faithfully and accurately the acoustic wave displacements with nearly a single point (100 microns) spatial resolution. Furthermore, heterodyne holography has the added ability of performing a full field acoustic mapping on optically rough surfaces, thus eliminating the need for surface preparation and multiple transducers in wave propagation studies.

2 Laser Generation of Ultrasound

A simple technique for remotely producing ultrasound is by irradiating a small region of a sample with a laser of sufficient power to produce local heating. A rapid rise in the local temperature and thus a rapid thermal expansion can initiate the propagation of an acoustic wave. The use of lasers for the generation of ultrasound in solids was first reported by White, who analyzed the case of a one dimensional thermal diffusion problem (White 1963). Since that work, a number of authors have gone on to examine the physical mechanisms involved with laser generation of ultrasound (Ready 1965, Scruby et al. 1980, Rose 1984, reviewed by Hutchins 1988). The analysis is a complicated one since the generation of acoustic waves in a solid infinite half-space will inevitably support several different wave modes: longitudinal, transverse, and surface waves. Ledbetter and Moulder were the first to demonstrate experimentally the simultaneous existence of the longitudinal, shear, and Rayleigh wave components for a single high powered laser excitation (Ledbetter & Moulder 1979). In their experiment, they focused a .3-1.0 J laser on to a block of aluminum and monitored the wave arrivals with a quartz transducer. A group at the University of Hull in the United Kingdom has conducted similar experiments at various laser power levels studying the effects of working below and above the threshold of plasma formation on generation efficiency (Aindow et al. 1981). As may be expected, the onset of plasma formation changes the generation mechanisms, as does constraining the free surface. The constrained surface changes the boundary conditions which greatly effects any wave propagation problem. Early investigators of acoustic wave phenomena like Rayleigh and Lamb have provided some insight into the complex influence of the specimen geometry. These guided wave modes have played an important part in ultrasonic inspection. Researchers studying laser

generation techniques have attempted to take advantage of these modes to investigate specific geometries that give rise to efficient generation schemes (Dewhurst et al. 1987, Hutchins 1988). These studies of laser generation mechanisms of ultrasound have greatly aided the field of nondestructive testing in developing useful noncontact inspection techniques.

In laser generation of ultrasound, there are two operative regimes dependent upon the incident laser energy. The low energy case is called the thermoelastic regime, where no surface damage or plasma formation is evident. The acoustic wave that is generated arises from the local thermal expansion caused by absorption of the incident laser beam. The acoustic amplitudes produced by laser generation under these conditions are directly proportional to the incident laser energy (Aindow et al. 1981). For the case of aluminium, about 6-10% of the incident energy is absorbed and the remainder is reflected. The absorbed energy causes a local temperature rise and a local expansion of the specimen. For fast rise time pulses, thermal diffusion is neglected and the expanded region is assumed to be localized in a small region near the surface. One can then model the stress from this volume change as two orthogonal horizontal force dipoles (Dewhurst et al. 1982). Physically, this is similar to inserting a thin volume of material at the surface (Fig. #2.1). Since a free surface is involved, the boundary conditions dictate that the tractions at the surface be equal to zero. The shear volume just below the surface is of sufficient size to support a strong dipole force in the in-plane direction. Thus a strong shear wave component is detected directly on axis with the production of the longitudinal component being related by an expression involving Poissons ratio (Rose 1984). However, both waves are highly directional and detecting off of the epicenter position will depend of the angle of propagation and the wave type. The research done by Dewhurst's group and Rose shows reasonably good agreement to the theoretical



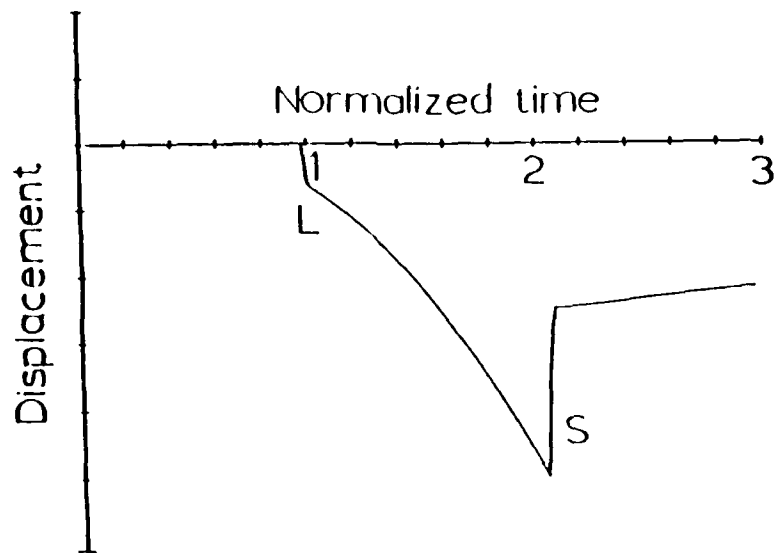
Thermoelastic laser generation mechanism
(Hutchins et al., 1986).

FIGURE #2.1

predictions (Fig. #2.2a&b) (Dewhurst et al. 1982, Rose 1984). The generation efficiency for the shear step arrival was 4.67 pm per mJ of incident energy at 1024nm and the longitudinal step arrival was 1.22 pm per mJ, both for on epicenter detection position. A modification to explain the positive going longitudinal spike at the onset of the arrival would have to take into account the effects of thermal diffusion. Even though the diffusivity in aluminium is such that the region of expansion is less than 10 microns for a 50 ns pulse, it still results in a small vertical force that satisfies the theory to account for the observed result. So, the thermoelastic generation regime is characterized by two orthogonal force dipoles in the plane of the material with a small normal force owing to the minor thermal expansion in that direction.

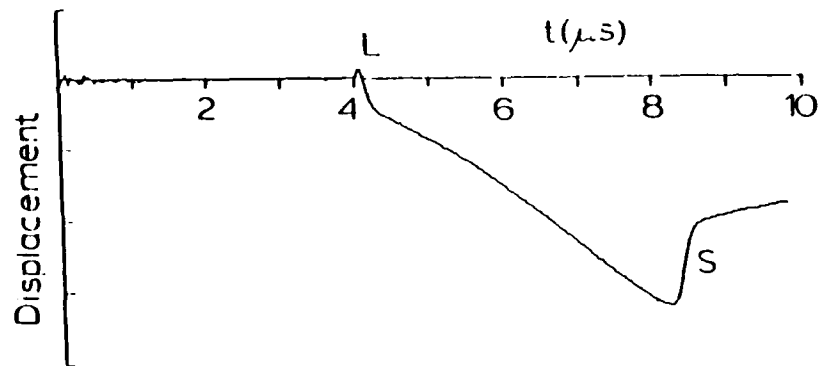
Ablation occurs when the incident power is great enough to cause melting at the surface and/or to evaporate the surface layer. The ablated particles produce a strong force normal to the surface through a complex momentum transfer mechanism. Modeling the effects of this normal force requires knowledge about the plasma interaction with the surface, which is not easily explained from first principles. This phenomenon is not well understood and its development will not be undertaken in this treatise. However, the physical effects are easily observed both acoustically and in terms of damage. It is known that the hot plasma contributes to the thermal expansion and to a normal force as evident by the strong longitudinal signal observed on epicenter, however understanding the physics of plasma formation is not a necessary requirement to obtain information about the acoustic wave generation.

Several authors have applied wave propagation theory in conjunction with the observed waveforms to estimate the stresses involved (Dewhurst et al. 1982, Rose 1984, Hutchins 1988). From this back calculation or deconvolution the generation



Theoretical, normal-displacement wave form for thermoelastic generation within an Al plate ($\nu=1/3$). Source modelled as orthogonal, horizontal force dipoles, with a step-function time dependence. (Hutchins et al., 1986)

Figure #2.2a



Thermoelastic, normal-displacement wave form in a 25.4 mm thick Al sample, generated by a 30 nsec, 120 mJ pulse from a frequency-doubled Q-switch ruby laser. The vertical scale is uncalibrated. (Hutchins et al., 1986)

Figure #2.2b

mechanism observed to be a combination of normal forces and thermoelastic expansion. Results have shown that by increasing laser power the thermoelastic and therefore shear wave contribution is reduced and an increasing normal force is observed. The normal force has a rapid rise time and longer time decay response that increases with incident laser energy (Hutchins 1986). The ablation process therefore accounts for a significantly larger longitudinal pulse on epicenter and in general larger displacement amplitudes.

Increasing the force components can also be achieved by constraining the free surface with a transparent material (Hutchins et al. 1981). The resulting acoustic wave is similar to that produced by ablation except that surface damage is avoided. The draw back is that some type of constraining material must be in contact with surface. A transparent overlay alters the stress relationships at the surface such that the normal force becomes dominant compared to the thermoelastic generation mechanism. For a solid overlay, such as a glass cover slip or cellophane tape, the boundary conditions are such that the tractions across the boundary are continuous rather than zero. This results in a significantly stronger normal force owing to the backing material or overlay. A similar improvement is also found in applying a liquid coating. An oil or water layer acts to constrain the surface. In addition, it can also contribute additional forces to the specimen by absorbing more of the light energy, causing a larger thermal expansion. Additionally the liquid layer itself may be evaporated, adding a different type of momentum transfer. The difference in generation mechanisms between the constrained layer case and the ablation case contributes to the differences in the rise times associated with the resultant forcing function observed in the acoustic signature. The slow decay time associated with ablation is absent in the constrained layer scheme.

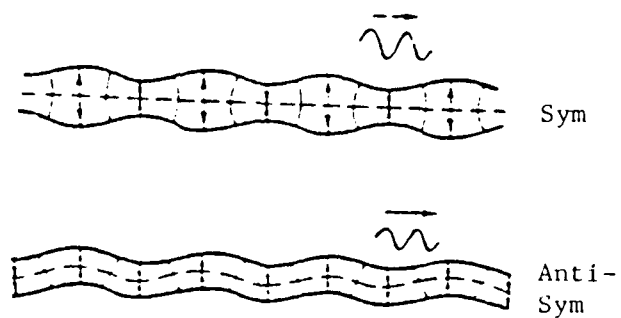
In terms of efficiency, the shear wave is more prominent than the longitudinal wave in the thermoelastic regime for an on epicenter observation. At the onset of ablation or with a constraining surface layer, the longitudinal wave amplitude becomes the larger of the two. Increased laser power will eventually result in the longitudinal wave dominating the acoustic signal at epicenter in the ablation regime, although it may be difficult to consider this regime as a purely nondestructive test. If the minor surface damage encountered in this regime would be acceptable, the gain in generated acoustic amplitude is an attractive benefit. However, an important aspect which has not been stressed here, is that the laser generated longitudinal and transverse wave are highly directional. That is to say that the amount of surface displacement detected on the opposite side of a thick plate varies as one moves off of the point of epicenter. In fact, in aluminum, the maximum longitudinal displacement is observed to be at an angle of 60 degrees from epicenter and the maximum shear displacement is found to be at an angle of 30 degrees from epicenter in the thermoelastic regime. This is a function of Poisson's ratio and the generation mechanism. For a more thorough treatment of the subject, one should consult Scruby or Schleichert (Scruby et al. 1982, Schleichert et al. 1988).

The third acoustic wave that is laser generated at a free surface of a semi-infinite plate is the Rayleigh wave (Ledbetter & Moulder 1979). The fact that the free surface constrains the boundary condition gives rise to the existence of the Rayleigh spike. This comes from applying the boundary conditions to the elastic wave equations. The resultant surface wave is a combination of longitudinal and transverse components and only exists at the surface. It propagates with an elliptical particle motion and with a wave speed near the shear wave velocity. It has been

observed to exist in all of the generation schemes thus discussed. Also, the amplitude appears to be enhanced with the onset of ablation and by the addition of a constraining layer (Hutchins 1986). Theoretical formulations by Rose in the thermoelastic regime model this phenomena by inserting a small thin volume of material into the surface. Rose predicted that the energy radiated into the Rayleigh wave would have an out of plane displacement amplitude greater than that of either the longitudinal or the shear wave for typical engineering materials (Rose 1984). Aindow had earlier substantiated the claim of increased Rayleigh wave amplitudes experimentally on a qualitative basis (Aindow et al. 1981). Further amplitude improvements can be achieved by focusing the laser beam to a line source using a cylindrical lens. This generates a highly directional Rayleigh wave. The wave front remains parallel to the line and propagates in the normal direction with minimal amount of energy reduction owing to propagation spreading. Cielo's group capitalized on this concept by using an axicon lense to focus the laser into an arc or circle (Cielo et al. 1985). This beam pattern produced a convergent Rayleigh wave. He then optically detected the convergent Rayleigh wave, which showed significant *amplitude enhancement at the center of the circle*. Cielo went on to show how the technique could be applied to the measurement of material properties. Laser generated Rayleigh waves have also been proven to be useful tool in locating and sizing surface breaking cracks (Aindow et al 1984, Hutchins et al. 1986). If a Rayleigh wave encounters a surface breaking defect reflections occur as do mode conversions giving a good indication of the size and location of the crack. As to the depth of inspection, the Rayleigh wave penetration is capable of extending about a wavelength below the surface. In remote generation and detection techniques, Rayleigh waves present an attractive inspection tool, since they can be made to be highly directional and offer greater displacement amplitudes than bulk acoustic waves.

Any constraining geometry will have considerable influence on the wave propagation characteristics in engineering structures as evidenced by Rayleigh waves. Surface waves are but a single example of a guided wave at the free surface of a semi-infinite half space. Plates or shells are another important and common structure that exhibits a strong guided wave phenomena. Wave propagation in plates was first described by Lamb in the early 1900's. Again, using the elastic wave equations and applying the traction free boundary conditions for the two sides of a plate, one is able to solve for the various Lamb or normal modes that exist in a plate (Viktorov 1967). As shown by Viktorov, the transverse and longitudinal waves are coupled in a thin plates to form two distinct types of Lamb waves. These symmetric and anti-symmetric waves exist simultaneously and independently of each other and the names are descriptive of the particle motions about the median plane of the plate. For the zero order modes, the symmetric waves are dilatational waves in the plate and the antisymmetric waves have a flexural motion as illustrated in Fig. #2.3. Laser generation schemes discussed so far have been shown to produce both types of Lamb modes (Dewhurst et al. 1987, Sontag & Tam 1986). The expressions for the respective phase velocities of the various modes comes about from solving the characteristic wave equations. It has been found to yield some rather ominous looking expressions for the symmetric phase velocities (Eq. #2.1) and the antisymmetric phase velocities (Eq. #2.2).

$$\text{symmetric:} \quad \frac{\tanh \pi f d \sqrt{\frac{v_s^2 - v^2}{v_s^2 v^2}}}{\tanh \pi f d \sqrt{\frac{v_l^2 - v^2}{v_l^2 v^2}}} = \frac{4 \sqrt{\left(1 - \frac{v^2}{v_l^2}\right) \left(1 - \frac{v^2}{v_s^2}\right)}}{\left(2 - \frac{v^2}{v_s^2}\right)^2} \quad (2.1)$$

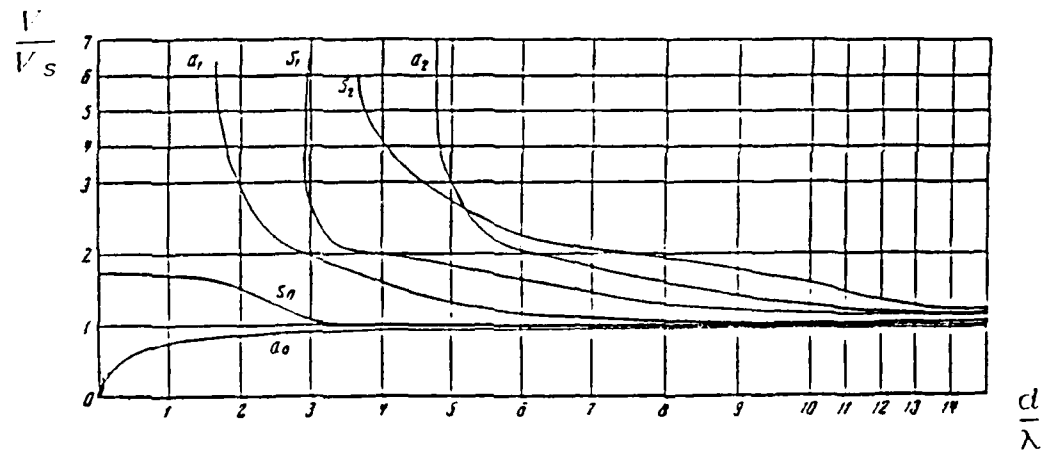


Symmetric and anti-symmetric wave motions (Viktorov, 1967)

FIGURE #2.3

$$\text{antisymmetric: } \frac{\tanh \pi f d \sqrt{\frac{V_s^2 - V^2}{V_s^2 V^2}}}{\tanh \pi f d \sqrt{\frac{V_l^2 - V^2}{V_l^2 V^2}}} = \frac{\left(2 - \frac{V^2}{V_s^2}\right)^2}{4 \sqrt{\left(1 - \frac{V^2}{V_l^2}\right) \left(1 - \frac{V^2}{V_s^2}\right)}} \quad (2.2)$$

These expressions written in this manner do not provide immediate insight, but with a little scrutiny can be easily deciphered. The Lamb wave velocity V has been expressed in terms of the shear wave velocity V_s , longitudinal velocity V_l , frequency f , and thickness d . Physical understanding is found by plotting the Lamb wave velocity with respect to the fd product (Fig. #2.4). The highly dispersive nature is directly related to the thickness and acoustic frequency product, fd . It is observed that for a given fd product there are a fixed number of modes that can exist. As the plate thickness increases two events occur. One, the wave speeds of the existing modes tend to approach the Rayleigh wave velocity, and second, the existence of new modes begin to appear. In this treatise, only the cases of thin plates, less than a couple of millimeters thick, will be investigated. For a constant plate thickness in this regime and considering the frequency content of laser generated waves, the only modes that can be sustained are the zero order modes (Dewhurst 1987). Of these, the asymmetric mode produces the largest in-plane displacements. Several authors have used these zero order modes to estimate plate thickness as well as determine material properties (Dewhurst et al. 1987, Hutchins & Lundgren 1988). Lamb waves, as would be expected, are extremely sensitive to any nonhomogeneous imperfections in a plate such as voids, inclusions, or surface defects. Such waves can also be made directional by focusing the laser with a cylindrical lens to form a line source similar to the Rayleigh wave case. This directionality can then be used to



Symmetric and antisymmetric Lamb wave phase velocity dispersion curves for the three lowest order modes (Victorov, 1967).

FIGURE #2.4

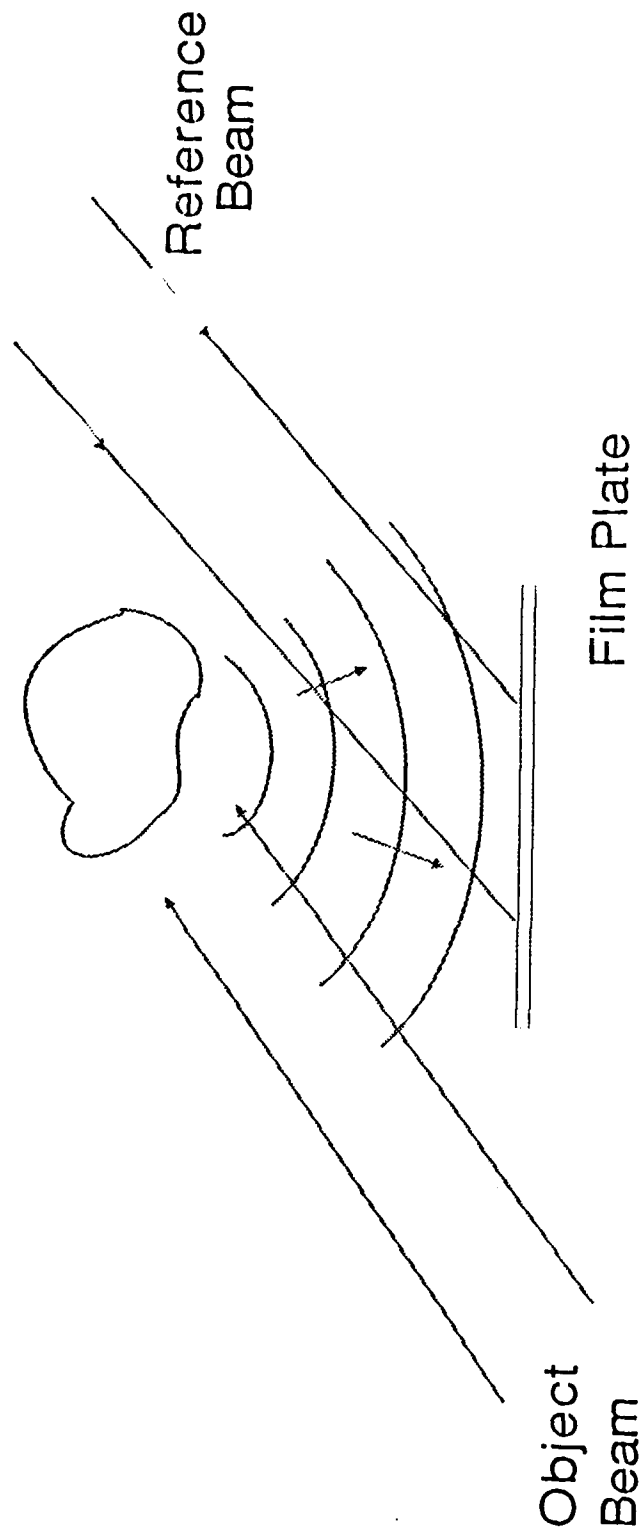
inspect local areas. One can envision that the tailoring of different modes and frequencies would enable the inspector to discriminate between different defect types and sizes (Rose & Pilarski 1988, Viktorov 1967).

The application of laser generated acoustic waves to ultrasonic nondestructive testing has become an attractive alternative to traditional transducer techniques in some cases (Aindow et al. 1984, Jungerman et al. 1984, Scurby et al. 1982). The source mechanisms have been well characterized and have been proven to provide calibration quality reliability (Hutchins et al. 1981). In addition, the specimens need not be flat, so complex geometries do not pose any problems. In some cases, the specimen geometries can actually enhance the out of plane displacements amplitudes. Also, the remote nature of the technique provides the opportunity to work in hostile environments. An advantage not easily accomplished with contact transducer techniques. However, laser generation of ultrasound is still in its infancy and needs further development work. Specifically, the development of a complementary remote detection capabilities is essential in order to take full advantage of the remote laser generation schemes. To this end, this treatise attempts to engage the problem of imaging laser generated acoustic wave in the full field on diffusely reflecting specimens that would normally not be interrogated with standard interferometry systems. It is shown in a latter section that imaging these amplitude displacements is possible with holography using the described phase measurement techniques in order to achieve the necessary sensitivity.

3 Holography

Holography is an imaging technique similar to photography in that it produces a lifelike image of the original subject. Both use a silver halide film as the recording medium with similar development procedures. However, holography differs from conventional photography in that the image formed is 3-dimensional rather than 2-dimensional. The term "hologram" is a derivative from the Greek language meaning "total recording". The image produced in the holographic process is a coherent image possessing both phase and amplitude information, hence a total recording. A normal photograph records only amplitude information. The added phase information recorded in holographic process allows an object's position in space to be completely specified. Since the image is coherent, this facilitates an interferometric comparison with respect to some initial state of the object of interest. The imaging of acoustic waves using holographic interferometry is formulated on just such a basis.

Gabor was the first to recognize this unique imaging process and he suggested that an image possessing both phase and amplitude information could be recorded on photographic film (Gabor 1948). This was a most unique discovery since photographic emulsions are only capable of recording an intensity pattern. Gabor postulated that the phase information could be converted into an intensity mapping that a film plate would be able to capture. This was accomplished by adding a second reference wavefront of known amplitude and phase with the original wavefront of interest (Fig. #3.1). A film plate, as seen in figure #3.1, is placed at the intersection of these two wavefronts recording the interference pattern. Assuming both of these wavefronts to be coherent, the resultant exposure will be spatially modulated dependent upon the incident angles and propagation paths of the respectful beams at the



Hologram Construction Configuration
Figure #3.1

film plate. The holographic process can be described mathematically from scalar diffraction theory where the complex amplitudes of the respective wavefronts are expressed using the direction cosines with respect to the axis normal to the hologram (Goodman 1968). The complex sum of amplitudes of the light arriving at the film plate is dependent upon the phase and amplitude of these wavefronts. The two interfering wavefronts are typically referred to as the reference wave and the object wave with the following phasor notation.

$$\begin{aligned} O &= A_o e^{j(\omega t - k \cdot r)} \\ &= A_o e^{j\phi} \end{aligned} \quad (3.1)$$

$$\begin{aligned} R &= A_r e^{j(\omega t - k' \cdot r)} \\ &= A_r e^{j\psi} \end{aligned} \quad (3.2)$$

Assuming the exposure range falls on the linear portion of the transmittance vs. exposure curve for the film plate, a linear mapping of the intensity can be expected; and the amplitude transmittance will be directly proportional to the squared magnitude of the sum of the two incident wavefronts.

$$\begin{aligned} T \propto I &= |O + R|^2 = (O + R)(O^* + R^*) \\ &= OO^* + RR^* + OR^* + RO^* \\ &= |A_o|^2 + |A_r|^2 + A_o A_r e^{j(\phi - \psi)} + A_r A_o e^{j(\psi - \phi)} \end{aligned} \quad (3.3)$$

The first two terms of equation #3.3 contain only amplitude information, but the last two terms retain both the amplitude and relative phase information, demonstrating that a film plate can indeed record the relative phase information. It still remains to reconstruct the desired image with the phase information intact.

The reconstruction process is performed after the photographic development process is completed. The film transparency is illuminated with another coherent wavefront. The light propagating away from the film plate, owing to the incident beam, is the product of the transmittance function of the film plate and the incident reconstruction wavefront (Fig. #3.2).

$$U = BT \propto = BOO^* + BRR^* + BOR^* + BRO^* \quad (3.4)$$

If this wavefront is a replica of the original reference wave, then a virtual image will be observed by an individual viewing the hologram.

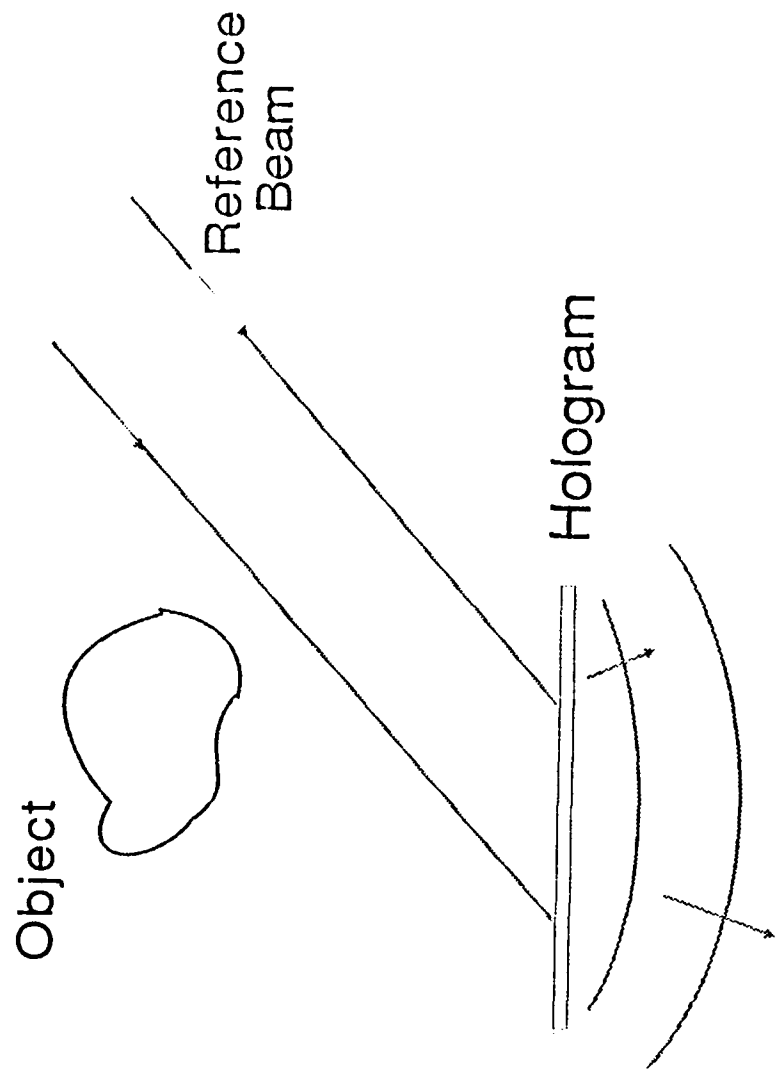
$$\begin{aligned} B &= A_r e^{j(\omega t - k \cdot r)} \\ &= A_r e^{j\psi} \end{aligned} \quad (3.5)$$

$$U = |A_o|^2 A_r e^{j\psi} + |A_r|^2 A_r e^{j\psi} + |A_r|^2 A_o e^{j\phi} + A_r A_r A_o e^{j(2\psi - \phi)} \quad (3.6)$$

It is the third term of this expression which replicates the image. Assuming that the reference and reconstructed wavefronts provide uniform illumination, then the third term

$$U_3 = |A_r|^2 A_o e^{j\phi} \quad (3.7)$$

is the original wavefront proportionality constant dependent on the incident laser power. Thus, part of the light incident on the hologram during reconstruction is diffracted in such a manner that it duplicates the wavefront that was diffusely reflected from the object. To an observer, a coherent virtual image of the object would



Hologram Reconstruction
Figure #3.2

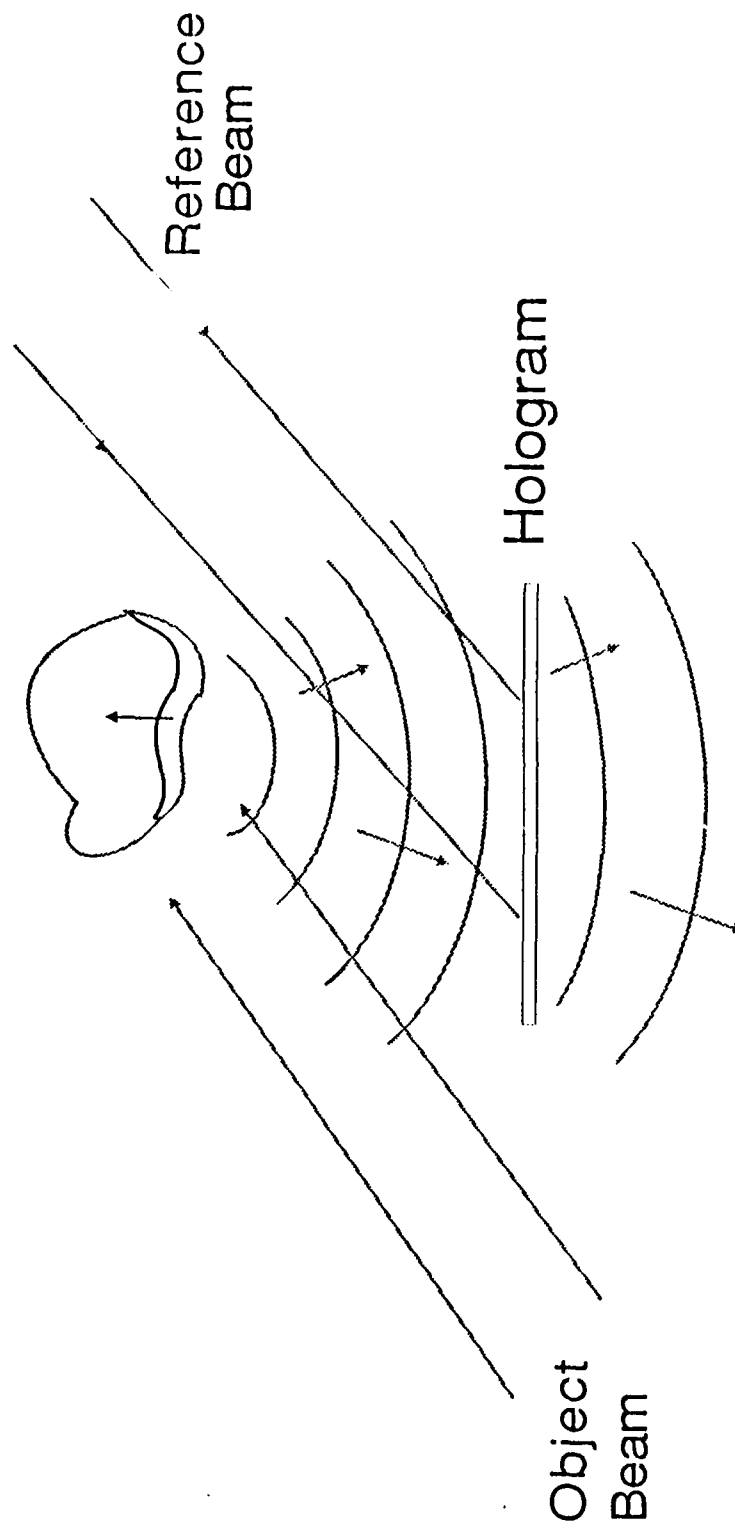
appear to be located in the object's original position.

3.1 Holographic Interferometry

The fact that the image formed in the holographic process is a coherent one, facilitates the application of interferometric techniques of optically rough objects. Evaluation of the surface displacements is typically made by either a real time process or a double exposure process. The real time process involves coherently illuminating the object and superimposing the reconstructed image with the real object (Fig. #3.3). One then observes an interference pattern as a stress is continually applied. Probably the more common technique is making a double exposure hologram. A double exposure hologram simply records two successive images on the same film plate. In this sense, holography is a linear process that can record multiple exposures and then reconstruct the images simultaneously. The first holographic exposure acts as the image reference state and the second exposure occurs after some type of mechanical disturbance has occurred. Upon reconstruction, the two images are superimposed and perfectly matched so that the interference pattern appears directly on the reconstructed image. The real time process sometimes requires tedious realignment procedures in order to properly superimpose the images for interference measurements.

From either case, however, the intensity pattern one observes when viewing the interferogram is known to be the squared magnitude of the summed amplitudes of the reconstructed images:

$$I = |U_3 + U_3'|^2. \quad (3.8)$$



Real Time Holographic Interferometry

Figure #3.3

The reconstructed images U_3' and U_3 have been shown to be directly proportional to the original object wavefronts respectively corresponding to the stressed and unstressed positions (Eq. #3.7). The quantity of interest in these original wavefronts is the relative phase difference between the two reconstructed wavefronts:

$$I \propto |O_1 e^{j(\omega t - k \cdot r - \phi_1(x, y))} + O_2 e^{j(\omega t - k \cdot r - \phi_2(x, y))}|^2. \quad (3.9)$$

Between the two exposures the amplitudes are assumed to be constant and the phase differences are separated into ϕ_1 and ϕ_2 to account for the out of plane displacements:

$$\begin{aligned} I &\propto 2O^2 + O^2 e^{j(\phi_2 - \phi_1)} + O^2 e^{-j(\phi_2 - \phi_1)} \\ &= 2O^2 \{1 + \cos(\phi_2(x, y) - \phi_1(x, y))\} \\ &= 2O^2 \{1 + \cos(\Delta\phi(x, y))\}. \end{aligned} \quad (3.10)$$

Equation #3.10 shows that the reconstructed image intensity is spatially modulated by the sinusoidal fringe pattern. For a coaxial illumination and viewing direction, the phase difference $\Delta\phi$, or interference term, is known to be twice the propagation constant times the out of plane displacement, $2kD$, where $k = \frac{2\pi}{\lambda}$. Thus, the observed intensity of the interference pattern goes as the cosine of the displacement and successive fringe contours correspond to a deformation of $\frac{\lambda}{2}$. Any object displacement or change will show up as bright or dark fringes corresponding to constructive and destructive interference. The resultant image is a topographic map of the object displacement.

However, most holographic systems use an off axis illumination and viewing angle for the object which reduces the displacement sensitivity somewhat. In order

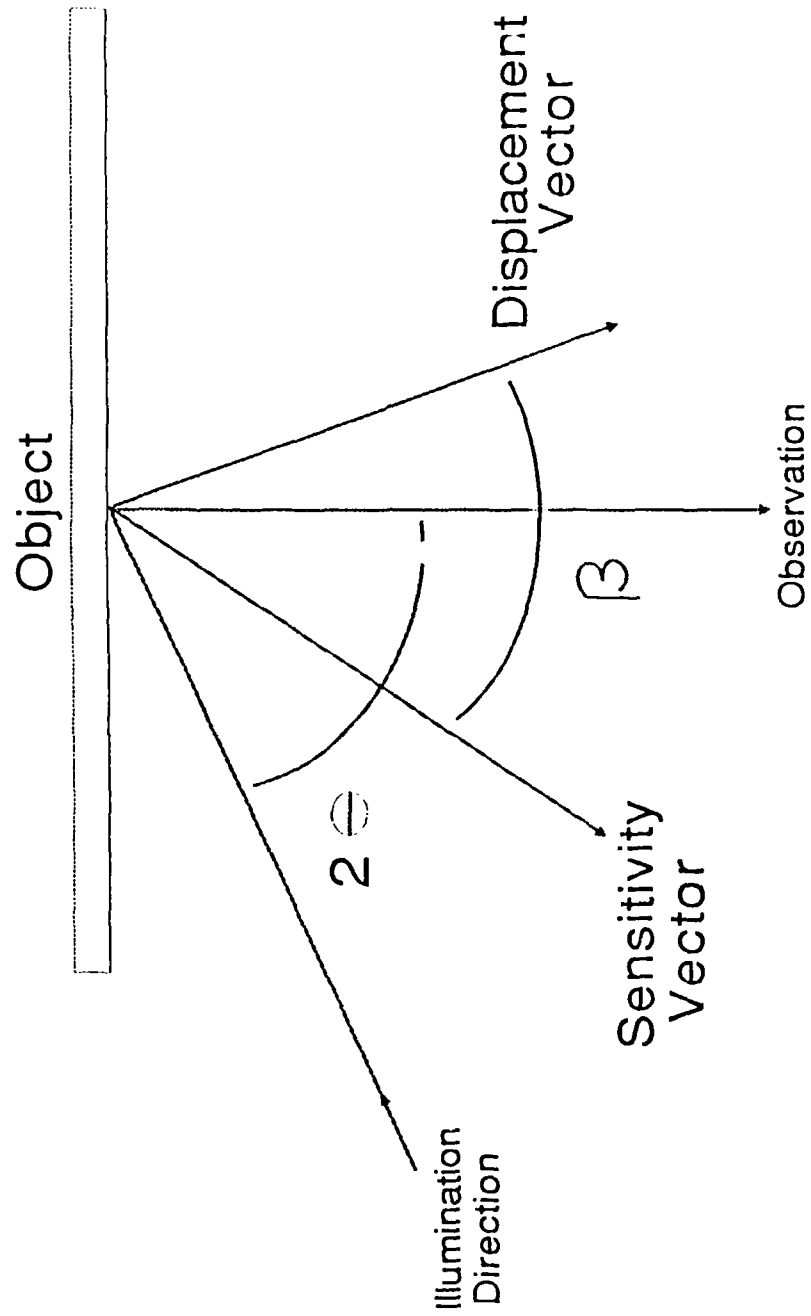
to be able to completely specify the object motion the sensitivity vector for the hologram must be known or determined (Vest 1979). The trigonometric argument, $\Delta\phi$, in equation #3.10, is actually the dot product of the sensitivity vector and the displacement vector for the general illumination and viewing case.

$$\Delta\phi = \vec{K} \cdot \vec{u} \quad (3.11)$$

The sensitivity vector is the vector bisecting the illumination direction and the observation direction, where this angle is defined to be 2θ (Fig. #3.4). The magnitude of the sensitivity vector is given as $|\vec{K}| = 2k \cos\theta$ and is in the direction of the angle bisector. The observed fringe pattern is measure of the amount of displacements that has occurred along that direction. So, when the displacement vector is known a priori, the measured phase change can be expressed as

$$\Delta\phi = 2k \cos\theta \cos\beta \quad (3.12)$$

where β is the angle between the displacement vector and the sensitivity vector. When the illumination and viewing angles are both on axis with the hologram and the displacement is also along this direction then the fringe spacing corresponds to the value $\frac{\lambda}{2}$. If the deformation is an unknown three dimensional disturbance then three independent views or observations must be made in order to establish both the direction and magnitude of the displacement. Fortunately however, most holographic configurations have the illumination and viewing angle nearly normal to the surface resulting in a maximum sensitivity to out of plane displacements, which is sufficient for many applications.



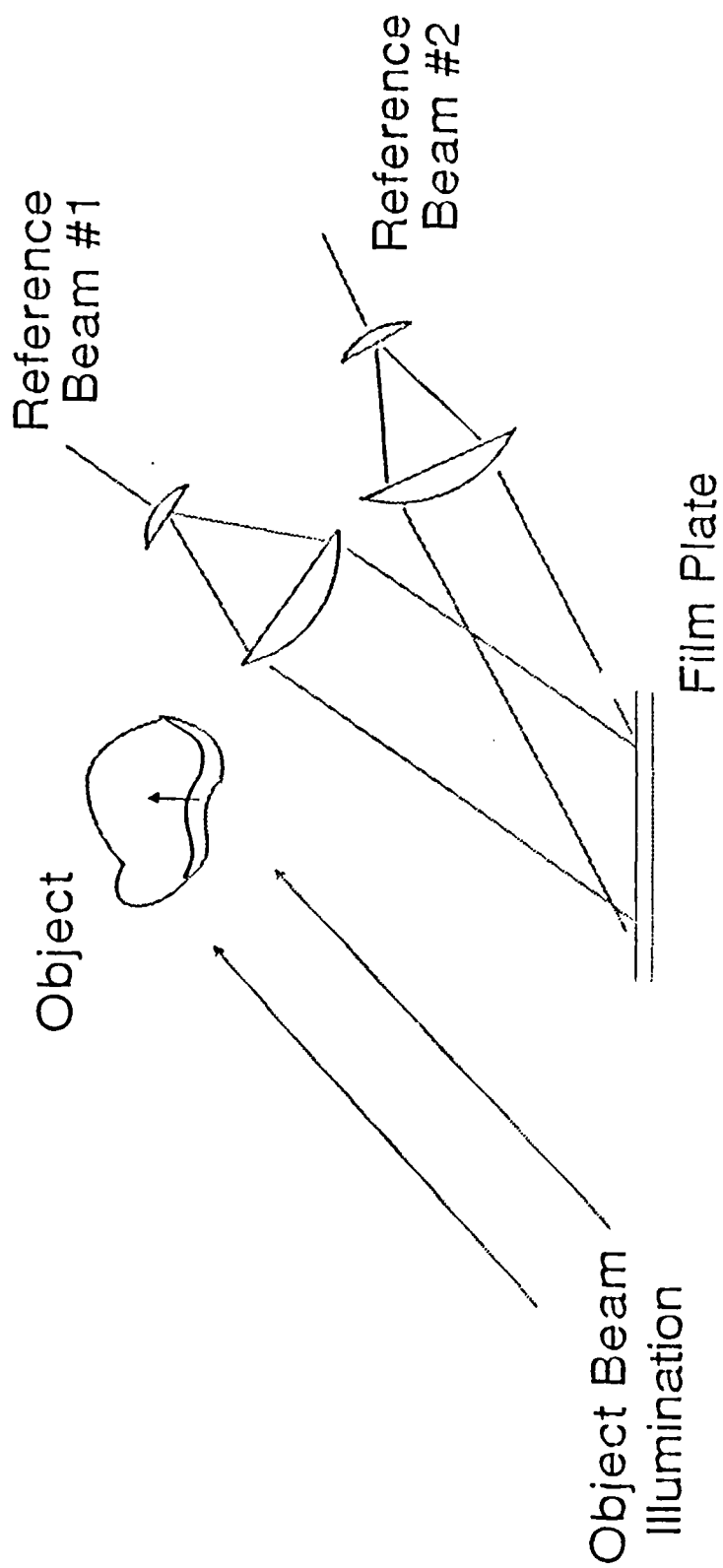
Schematic showing the relationship between the sensitivity vector and the displacement vector

Figure #3.4

3.2 Heterodyne Holographic Interferometry

Retrieving the phase information from the interference fringes on a holographic image is greatly enhanced by the application of heterodyne analysis. Heterodyne interferometry is a precise phase measurement technique that was originally applied in broad beam interferometry systems for inspecting large optical components (Crane 1969). Dandliker and his colleagues later applied this technique to holographic interferometry of diffusely reflecting objects (Dandliker 1973). This technique is based on the interjection of a small frequency shift between the two interfering images. This imposed frequency difference modulates the reconstructed images producing a time varying fringe pattern rather than a static fringe pattern. Static fringe analysis techniques have been shown to suffer from a loss of sensitivity in the dark field portions of the interferogram. However, heterodyne analysis avoids this signal-to noise ratio caveat by detecting a time varying intensity, the phase of which is still dependent upon the local path length changes of the two object states. In this way, heterodyne analysis is able to precisely measure the phase difference and thus determine the displacement that has occurred.

Constructing a double exposure hologram that is suitable for heterodyne analysis requires the addition of a second reference beam as shown in Fig. #3.5. The two positional states of the object are independently recorded by the respective reference beams. Reference beam #1 records the initial position while reference beam #2 records the deformed state. This facilitates separate reconstruction control of the two interfering images, a necessary process in order to introduce the desired frequency shift between the two images. After the holographic plate is developed, the new transmittance function produced in this configuration is expressed in equation #3.13 (review by Dandliker 1980).



Holographic Recording Scheme
for Heterodyne Analysis
Figure #3.5

$$T \propto O_1 O_1^* + R_1 R_1^* + O_1 R_1^* + R_1 O_1^* + O_2 O_2^* + R_2 R_2^* + O_2 R_2^* + R_2 O_2^* \quad (3.13)$$

The first four terms of this expression are represent the first exposure and the last four terms represent with the second exposure. Upon reconstruction, the only two terms that will be propagated in the desired observation direction are the $O_1 R_1^*$ and the $O_2 R_2^*$ components. The frequency shift needed in the reconstructed images O_1 and O_2 in order to perform heterodyne analysis is achieved by frequency shifting the reconstruction wavefronts at slightly different frequencies, ω_1 and ω_2 (Eq #3.14a&b).

$$B_1 = A_r e^{j(\omega_1 t + \psi_1)} \quad (3.14a)$$

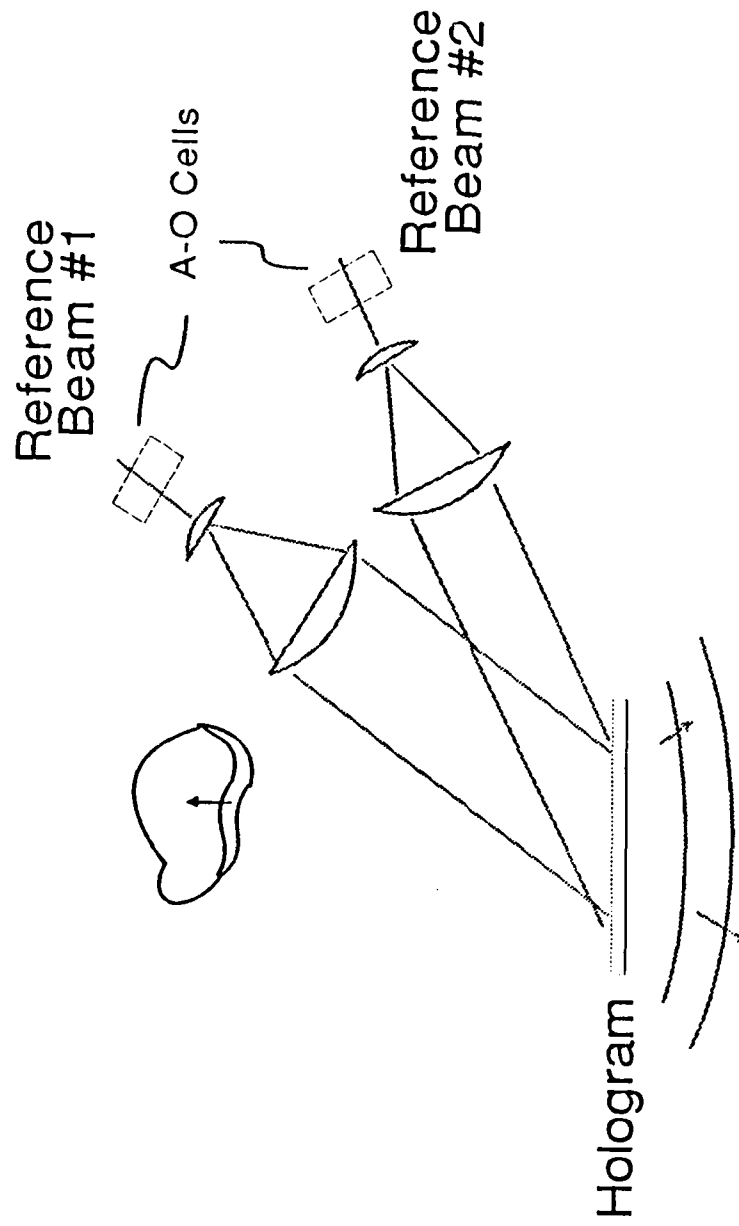
$$B_2 = A_r e^{j(\omega_2 t + \psi_2)} \quad (3.14b)$$

This is accomplished by inserting an acousto-optic modulator in to each reference beam as shown in Fig. #3.6. This will in turn impart a frequency shift to the images of interest. First, however, consideration should be given to the consequences of using two well separated reference beams in the hologram construction.

$$\begin{aligned} U_3 + U_3^* &= B_2 R_1^* O_1 + B_1 R_2^* O_2 + B_1 R_1^* O_1 + B_2 R_2^* O_2 \\ &= R_2 R_1^* O_1 + R_1 R_2^* O_2 + |R_1|^2 O_1 + |R_2|^2 O_2 \end{aligned} \quad (3.15)$$

$$= O_1 A_r^2 e^{j(\omega_2 t + \psi_1 - \psi_2)} + O_2 A_r^2 e^{j(\omega_1 t + \psi_2 - \psi_1)} + O_1 A_r^2 e^{j\omega_1 t} + O_2 A_r^2 e^{j\omega_2 t} \quad (3.16)$$

As is observed in equations #3.15 and 3.16, each reference beam reconstructs a pair of images in or near the desired image plane. The last two terms are the two



Heterodyne Reconstruction Configuration

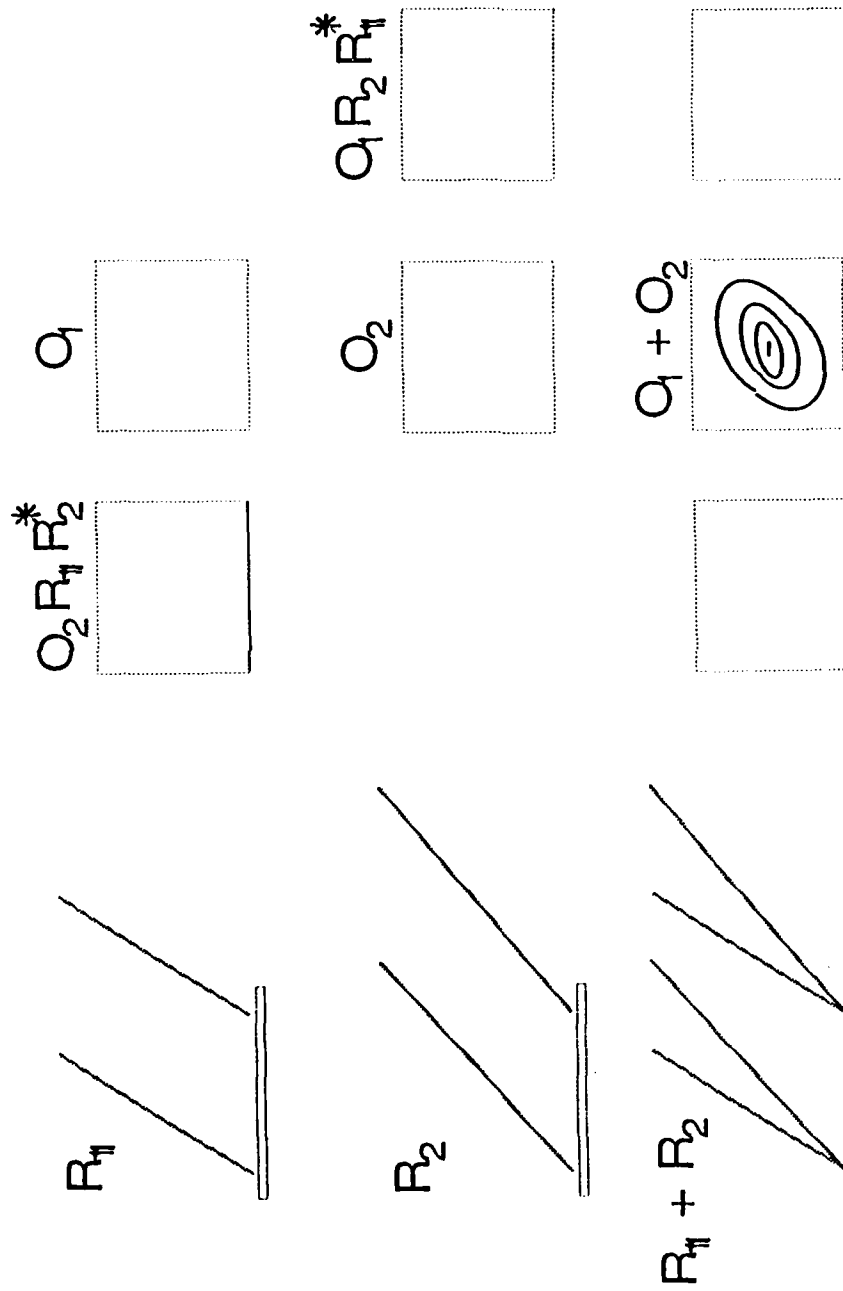
Figure #3.6

virtual images of interest that propagate in the direction of the original wavefronts. The first two terms in equation #3.15 are artifacts of dual reference beam holography that can be detrimental to the phase sensitivity if they should overlap the region of interest (Fig. #3.7). Their relative spatial positions are dependent upon the angular separation of the two reference beams, $\psi_1 - \psi_2$. Ideally, to achieve maximum phase sensitivity, the angular separation should be large enough so that the area of interest, in the interferogram, would not have any overlapped portions of the unwanted images, $R_1 R_2^* O_2$, $R_2 R_1^* O_2$. Proceeding then with this assumption, the mathematical development of heterodyne analysis need only consider the two image terms of interest.

These two wavefronts that arrive at the image plane are observed to have two different frequencies owing to the respective reconstructing wavefronts, B_1 and B_2 (Eq. #3.16 & #3.17).

$$U_{3,3} = O_1 A_r^2 e^{j\omega_1 t} + O_2 A_r^2 e^{j\omega_2 t} \quad (3.17)$$

The intensity measured by a photo-detector in the image plane is proportional to the squared magnitude of this incident field. For this development, the reference and reconstruction wavefronts are defined to have unity amplitude and the object waves are considered to be real valued.

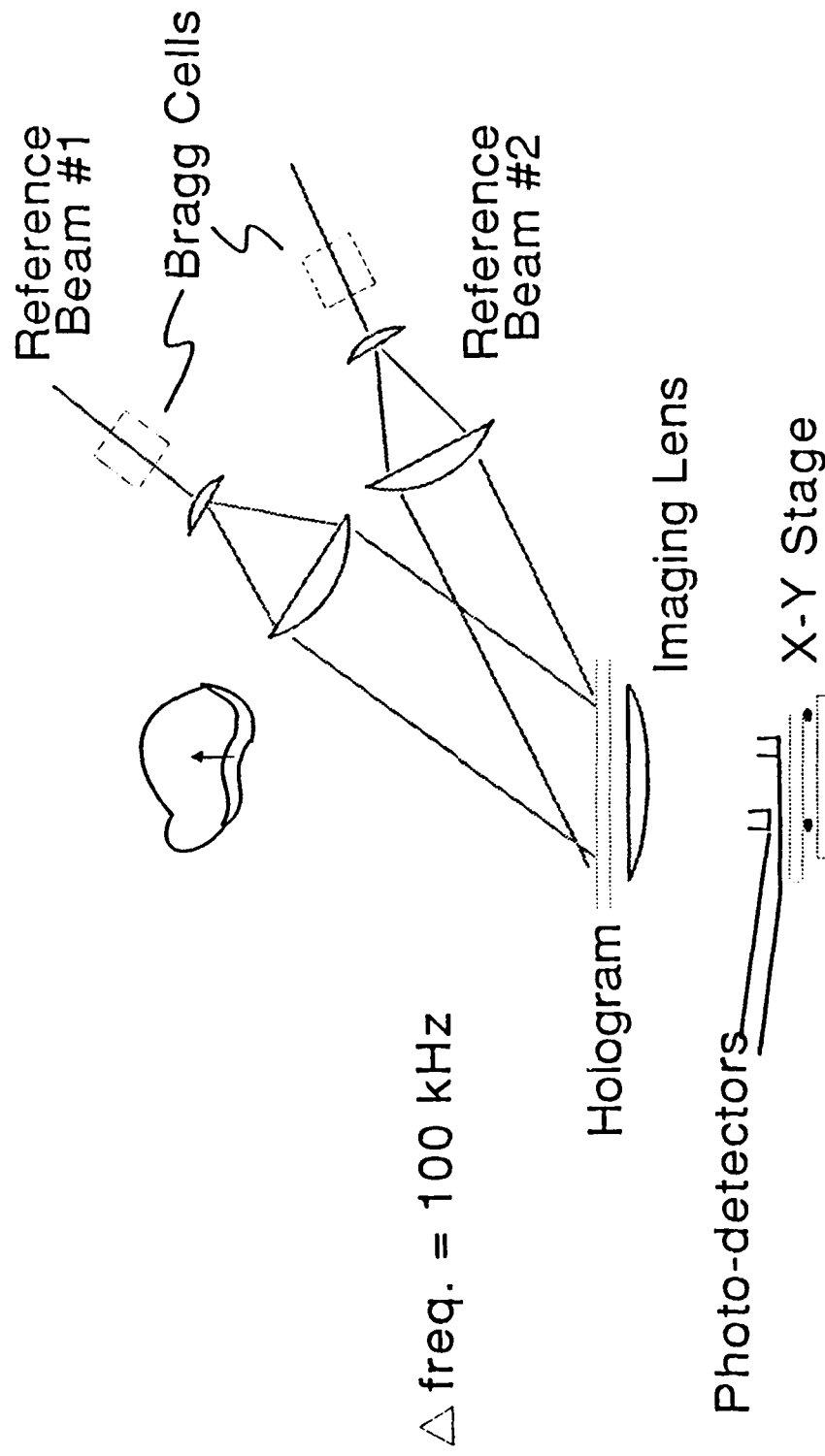


Overlapping Image Situation
Figure #3.7

$$\begin{aligned}
I &\propto |O_1 e^{j(\omega_1 t + \phi_1)} + O_2 e^{j(\omega_2 t + \phi_2)}|^2 \\
&= O_1^2 + O_2^2 + O_1 O_2 e^{j((\omega_1 - \omega_2)t + \phi_1 - \phi_2)} + O_1 O_2 e^{-j((\omega_1 - \omega_2)t + \phi_1 - \phi_2)} \\
&= O_1^2 + O_2^2 + 2O_1 O_2 \cos(\Delta\omega t + \Delta\phi) \\
&= (O_1^2 + O_2^2)(1 + M \cos(\Delta\omega t + \Delta\phi)) \tag{3.18}
\end{aligned}$$

$$\text{where } M = \frac{2O_1 O_2}{O_1^2 + O_2^2}.$$

As expressed in equation #3.18, a photo-detector in the image plane will measure a time varying intensity. The frequency of this signal is found to be the difference frequency between ω_1 and ω_2 , while the displacement information is still contained in the phase difference $\Delta\phi$ term of the cosine argument. Precise discrimination of this phase difference is accomplished through heterodyne analysis comparing the measured photo-detector signal to a reference signal of the same frequency. Typically, this reference signal is derived from a stationary photo-detector in the same image plane. The phase difference measured between the signal detector and a stationary reference signal is the phase difference between the two interfering electric fields and hence a direct scale of the deformation that has occurred. Electronic phase measurement techniques, like a lock-in amplifier, can readily differentiate phase differences of 0.1 degrees, providing sufficient sensitivity to observe sub-fringe displacements. By monitoring this phase difference and using a scanning stage to position a photo-detector, a direct mapping of the object deformation is possible (Fig #3.8). Heterodyne analysis of holographic interferometry has changed the analysis from a normally qualitative analysis to a precise quantitative technique of the resulting fringe pattern and facilitating the investigation of sub-fringe displacement phenomenon.



Heterodyne Reconstruction
Figure #3.8

3.3 Quasi-heterodyne Interferometry

Quasi-heterodyne analysis is another phase measurement technique that was employed in this study. Similar to its' close relative, heterodyne analysis, the application to holographic interferometry was first born in the area of interferometric wavefront analysis for testing optical components (Bruning et al. 1974). This technique in particular has been attractive to the optics manufacturers for quality control purposes owing to the rapid acquisition of data while maintaining adequate phase sensitivity. This is evidenced by the commercial success of companies such as Zygo, Tropel, and Wyco in producing these instruments. In particular, one of systems from Tropel uses a computer generated hologram as the optical reference element for interferometric comparison. Holographic interferometry benefits from this analysis technique for similar reasons. Data is acquired in a timely fashion using a photo-detector array; the displacement sensitivity has been to be on the order of $\frac{\lambda}{200}$. Heterodyne analysis offers better displacement sensitivity, $\frac{\lambda}{2000}$, but suffers from a lengthy scanning process that acquires data on a point by point basis.

Quasi-heterodyne analysis has been referred to as digital interferometry and phase step interferometry, both of which are indicative of the technique that involves computer aided analysis from the measured phase states of the image to determine the relative surface displacements. Implementing quasi-heterodyne analysis in holographic interferometry uses the same dual reference beam configuration in the hologram construction as did heterodyne analysis (Fig #3.5). From equation #3.18, the intensity measured by a photo-detector array at the image plane of the reconstructed interferogram is a function of the background intensity I_0 , the fringe

contrast M , and the relative phase difference $\Delta\phi$. In this analysis technique, there is no frequency shift between the reference beams, but rather a controlled phase step that is accounted for by θ_i .

$$I_i = I_o(1 + M \cos(\Delta\phi + \theta_i)) \quad (3.19)$$

Quasi heterodyne analysis is an arithmetic calculation of the desired phase term, $\Delta\phi$, from multiple intensity measurements. This phase determination is accomplished by performing successive phase steps of known quantity and recording the interference pattern. This is exemplified through equations #3.20a-c, where one will notice that there are three equations and three unknowns.

$$I_1 = I_o(1 + M \cos(\Delta\phi + \theta_1)) \quad (3.20a)$$

$$I_2 = I_o(1 + M \cos(\Delta\phi + \theta_2)) \quad (3.20b)$$

$$I_3 = I_o(1 + M \cos(\Delta\phi + \theta_3)) \quad (3.20c)$$

From basic algebra principles and a few trigonometric identities, the phase difference can be analytically determined. For the specific shifts of $\theta_i = 0^\circ, 90^\circ, 180^\circ$, the solution is readily solved as shown in equation #3.21 (Hariharan 1985, Frantz et al. 1979).

$$I_1 = I_o(1 + M \cos(\Delta\phi))$$

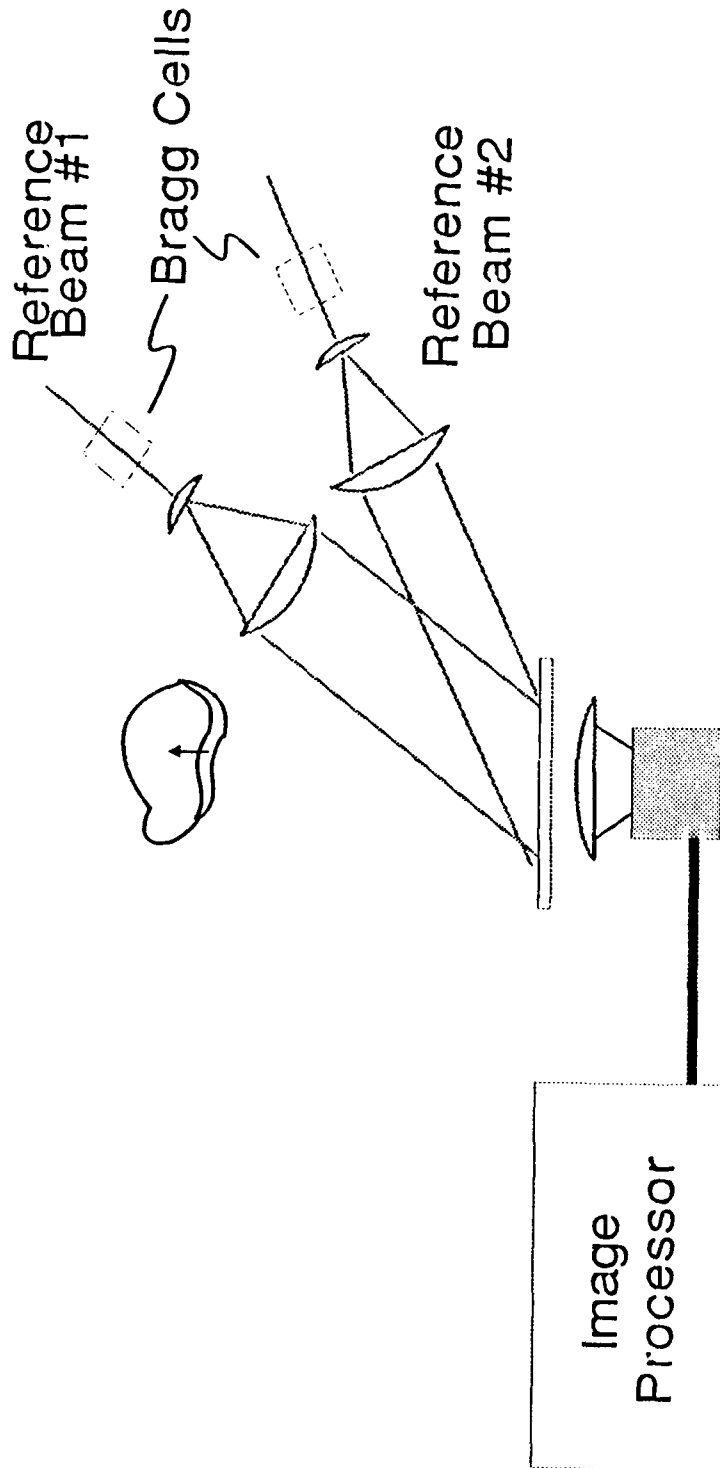
$$I_2 = I_o(1 + M \sin(\Delta\phi))$$

$$I_3 = I_o(1 - M \cos(\Delta\phi))$$

$$\Delta\phi = \tan^{-1} \frac{2I_2 - I_1 - I_3}{I_1 - I_3} \quad (3.21)$$

The task of acquiring the intensity data corresponding to the three phase shifts is accomplished by the set-up shown in figure #3.9. The configuration is similar to the heterodyne reconstruction set-up, but with a few changes. The the Bragg cells are driven at the same frequency, shifting the diffracted light by the same amount, however one Bragg cell has a drive signal that is phase delayed compared to the other. It can be shown that by phase shifting the drive signal to the acousto-optic cell corresponds to the same relative phase delay in the first diffracted order (Ehrlich et al. 1988). Most quasi-heterodyne configurations employ mirror mounted on a pusher to physically control the path length change and hence the phase shift. The purpose behind this configuration is to facilitate an easy change between heterodyne and quais-heterodyne read-out systems with out any additional optical components nor any optical realignment. As shown in figures #3.8 and #3.9, the only change that is necessary, to go from the heterodyne analysis to quasi-heterodyne analysis, is the substitution of the appropriate detection system behind the film plate.

For quasi-heterodyne holographic interferometry, a CCD camera is typically used for the data acquisition. Here, the three images can be detected and recorded at TV frame rates with an image processing board interfaced with a computer, thus eliminating the mechanical scanning process. The displacement information is calculated in the period of time needed for the computer processing. Harihan's group reports a processing time of as little as 10sec for a 100 by 100 array (Harihan et al. 1983). However the increased processing time comes at the expense of sensitivity when compared to heterodyne analysis. This relative reduction for quasi-heterodyne analysis to $\frac{\lambda}{200}$ can be accounted for in the uncertainty involved with



Quasi-heterodyne Reconstruction Configuration
Figure #3.9

the phase stepping and variations in the local intensity (Wyant 1975, Schwider et al. 1983). If an out of plane displacement sensitivity of $\frac{\lambda}{200}$ would be acceptable then the gain from reduced processing time makes holographic interferometric techniques more than just a laboratory curiosity where it becomes well suited for industrial applications and nondestructive testing techniques.

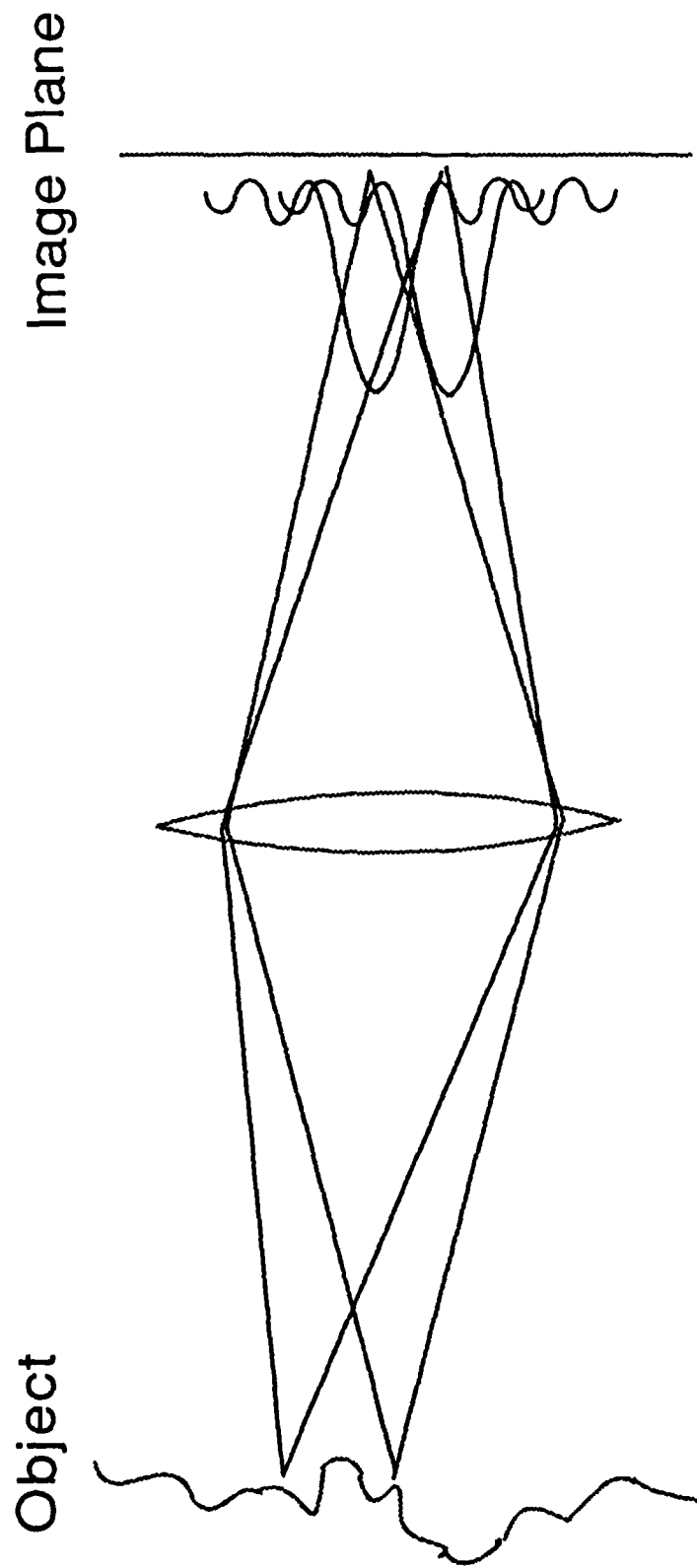
4 Imaging a Diffuse Object

Anyone that has observed a coherent image of a diffuse object will recall that the image appeared to be granular or speckled in nature. This chaotic pattern is really an interference phenomenon owing to the coherent nature of the light, the surface roughness, and the limited aperture of the imaging optics; and bears no resemblance to the overall macroscopic shape of the object. An object is considered to be a diffuse reflector "or rough" if the microscopic detail is on the scale of the optical wavelength. The light, then scattered from the object and observed a reasonable distance away, will have numerous contributions from other areas that are coherent, but dephased. These delayed or dephased components will be superimposed and interfere resulting in the described speckle pattern.

Imaging this coherent reflection is a similar process. Fourier optics predicts that an individual object point will be imaged as an amplitude spread function owing to diffraction effects of the finite aperture (Hecht & Zajac 1979). Neighboring points will be phase delayed due to the surface irregularities and the amplitude spread functions will be superimposed interfering in a similar fashion (Fig. #4.1). The resulting image will have a speckle pattern imposed upon it degrading image quality.

This phenomena is not unique to holography and has been studied in other coherent interactions such as radar astronomy, electrical noise, synthetic aperture radar, and acoustic imaging to name a few. The chaotic nature of the speckle pattern can best described with probability and statistics (Goodman 1976).

A statistical analysis of the far-field speckle pattern was first developed by Goldfischer for a uniformly illuminated diffuse object (Goldfischer 1965). Lowenthal and Arsenault subsequently wrote a classic paper from a systems analysis



Coherent Image Formation
Figure #4.1

approach on the same topic (Lowenthal & Arsenault 1970). Included in their approach were image formation and non-uniform illumination. From these statistical approaches, information concerning the speckle size, system impulse response, and the noise in the image can all be deduced. A definitive treatise has been written by Goodman "Statistical Properties of Laser Speckle Patterns", which this development will closely follow, along with that of Dandliker (Goodman 1970, Dandliker 1980).

From wave propagation phenomenon and scalar diffraction theory, the image amplitude can be represented as a linear space-invariant filtering operation. The superposition integral describing this process is given in equation #4.1 (Goodman 1968). Here, the space variables x_i, x_o are really two dimensional space variables simplified for the sake of notation.

$$V(x_i) = \int_{-\infty}^{\infty} O(x_o) h(x_i - Mx_o) d^2 x_o \quad (4.1)$$

It becomes useful to expand the object term $O(x_o)$, so that it separately takes into account the macroscopic surface shape $\bar{O}(x_o)$ and the microscopic surface roughness $\rho(x_o)$ (Dandliker 1980).

$$V(x_i) = \int_{-\infty}^{\infty} \bar{O}(x_o) \rho(x_o) h(x_i - Mx_o) d^2 x_o \quad (4.1a)$$

The variable $\rho(x_o)$ is a circular complex Gaussian variable describing the surface roughness. The statistics of this variable are assumed to have independent real and imaginary parts, wide-sense stationary, zero mean and the same variance. This term

accounts for the random phase condition for a diffuse object, thus producing the speckle pattern. The last expression in this equation is the impulse response $h(x_i - Mx_o)$ which is related to the aperture of the imaging system and the propagation distances. In satisfying the geometric lens law, the expression for the impulse response is shown to be:

$$h(x_i - Mx_o) = \frac{1}{\sqrt{A_p \lambda d_o d_i}} \int_{-\infty}^{\infty} P(x_p) e^{-\frac{ik}{d_i}(x_i - Mx_o)x_p} d^2 x_p \quad (4.2)$$

$$P(x_p) = 1 \text{ for } x_p < \text{radius aperture}$$

$$= 0 \text{ for } x_p > \text{radius aperture}$$

$$M = \text{image magnification}$$

$$x_p = \text{spatial coordinates in the}$$

pupil plane

$$k = 2\frac{\pi}{\lambda}$$

One will notice that this integral is observed to be the Fraunhofer diffraction pattern centered about the points $x_i = Mx_o$. For this development, it will be normalized by the effective aperture area.

$$A_p = \frac{1}{\lambda d_o d_i} \int_{-\infty}^{\infty} |P(x_p)|^2 d^2 x_p \quad (4.3)$$

Calculation of the intensity distribution in the image plane is simply the squared magnitude of the image amplitude.

$$I(x_i) = V(x_i) V^*(x_i) \quad (4.4)$$

As has been stated, the intensity in the image plane is really a Gaussian random process and can best be described statistically. For the analysis of random signals, determination of the mean and autocorrelation are necessary for a linear system.

The mean of the system comes directly from the ensemble average of equation #4.4.

$$\langle I(x_i) \rangle = \langle V(x_i) V^*(x_i') \rangle \quad (4.5)$$

$$\begin{aligned} &= \langle \int \int_{-\infty}^{\infty} \bar{O}(x_o) \bar{O}^*(x_o') \rho(x_o) \rho^*(x_o') \\ &\quad \times h(x_i - Mx_o) h^*(x_i' - Mx_o') d^2x_o d^2x_o' \rangle \\ &= \int \int_{-\infty}^{\infty} \langle \bar{O}(x_o) \bar{O}^*(x_o') \rangle \langle \rho(x_o) \rho^*(x_o') \rangle \\ &\quad \times h(x_i - Mx_o) h^*(x_i' - Mx_o') d^2x_o d^2x_o' \end{aligned} \quad (4.6)$$

Two terms which have a significant effect on resulting speckle pattern are the surface roughness and the impulse response. The ensemble average of the surface roughness is observed to be the autocorrelation of the fine microstructure. Imaging this fine microstructure is not a possibility for most optical systems. Hence, a comparison of the autocorrelation of the surface roughness and the optical transfer function reveals that the optical transfer function is a much broader function. This leads to approximating the autocorrelation of the surface roughness as a Dirac delta function.

$$\begin{aligned} \langle \rho(x_o) \rho^*(x_o') \rangle &= R_\rho(x_o - x_o') \\ &\cong \delta(x_o - x_o') \end{aligned} \quad (4.7)$$

Applying the sifting property of delta functions further simplifies equation #4.6 to a convolution of the intensity with the autocorrelation of the impulse response.

$$\langle I(x_i) \rangle = \int_{-\infty}^{\infty} |\bar{O}(x_o)|^2 h(x_i - Mx_o) h^*(x_i' - Mx_o) d^2 x_o \quad (4.8)$$

Most instances, the macroscopic surface shape is assumed to be constant, since the value does not typically change over the photo-detector aperture.

$$\langle I(x_i) \rangle = |\bar{O}(x_o)|^2 \int_{-\infty}^{\infty} h(x_i - Mx_o) h^*(x_i' - Mx_o) d^2 x_o \quad (4.9)$$

$$|\bar{O}(x_o)|^2 \cong \text{constant}$$

Substitute the expression for the impulse response equation #4.2 into equation #4.9 and the result becomes (Dandliker 1980)

$$\langle I(x_i) \rangle = K^2 |\bar{O}(x_o)|^2 \int_{-\infty}^{\infty} \left\{ \int_{-\infty}^{\infty} |P(x_p)|^2 e^{-\frac{ik}{d_i}(x_i - Mx_o)x_p} e^{\frac{ik}{d_i}(x_i' - Mx_o)x_p} d^2 x_p \right\} d^2 x_o$$

$$K = \frac{1}{\sqrt{A_p} \lambda d_o d_i}$$

$$\langle I(x_i) \rangle = K^2 |\bar{O}(x_o)|^2 \int_{-\infty}^{\infty} \left\{ \int_{-\infty}^{\infty} |P(x_p)|^2 e^{-\frac{ik}{d_i}(x_i - x_i')x_p} d^2 x_p \right\} d^2 x_o \quad (4.10)$$

Solving the integration with respect to the spatial variable x_o is found to yield a constant related to the object size and illumination.

$$\int_{-\infty}^{\infty} \{ \} d^2 x_o = \text{constant} \quad (4.11)$$

The other second integration with respect to x_p is recognized to be a two dimensional Fourier transform.

$$\begin{aligned} \langle I(x_i) \rangle &= K^2 |\bar{O}(x_o)|^2 \int_{-\infty}^{\infty} |P(x_p)|^2 e^{-\frac{ik}{d_i}(x_i - x_o)x_p} d^2 x_p \\ &= |\bar{O}(x_o)|^2 \gamma(\Delta x) \end{aligned} \quad (4.12)$$

For the special case of a circular aperture, the solution is a first order Bessel function divided by its' argument.

$$\gamma(\Delta x) = \frac{2J_1\left(\frac{\pi \Delta x D}{\lambda d_i}\right)}{\left(\frac{\pi \Delta x D}{\lambda d_i}\right)} \quad (4.13)$$

D = diameter of the lens

$$\Delta x = x_i - x_o$$

First order statistics provide amplitude distributions, but are inadequate for completely specifying the system. A complete description of the statistical properties of the speckle phenomenon requires the calculations of the second order statistics. For Gaussian statistics, the process is completely specified by the second order statistics, which is not necessarily true of other random processes (Lathi 1968). Calculating the autocorrelation function of the intensity becomes a four fold correlation problem of the amplitude.

$$\begin{aligned}
 R_I(x_i, x'_i) &= \langle I(x_i) I(x'_i) \rangle \\
 &= \langle V(x_i) V^*(x'_i) V(x''_i) V^*(x'''_i) \rangle
 \end{aligned} \tag{4.14}$$

$$\begin{aligned}
 R_I(x_i, x'_i) &= \int \int \int \int_{-\infty}^{\infty} |\bar{O}(x_o)|^2 |\bar{O}(x''_o)|^2 \langle \rho(x_o) \rho^*(x'_o) \rho(x''_o) \rho^*(x'''_o) \rangle \\
 &\quad h(x_i - Mx_o) h^*(x'_i - Mx'_o) h(x''_i - Mx''_o) h^*(x'''_i - Mx'''_o) \\
 &\quad d^2 x_o d^2 x'_o d^2 x''_o d^2 x'''_o
 \end{aligned} \tag{4.15}$$

As before in equation #4.5, the first step is to calculate the correlation function for the surface roughness. This time, however, it is a four fold correlation problem.

Using the fact that the function $\rho(x)$ obeys circular Gaussian statistics, this problem becomes simply the summation of all possible permutations (Reed 1962, Goodman 1985).

$$\begin{aligned}
 \langle \rho(x_o) \rho^*(x'_o) \rho(x''_o) \rho^*(x'''_o) \rangle &= \langle \rho(x_o) \rho^*(x'_o) \rangle \langle \rho(x''_o) \rho^*(x'''_o) \rangle \\
 &\quad + \langle \rho(x_o) \rho^*(x'''_o) \rangle \langle \rho(x''_o) \rho^*(x'_o) \rangle \\
 &= \delta(x_o - x'_o) \delta(x''_o - x'''_o) + \delta(x_o - x'''_o) \delta(x''_o - x'_o)
 \end{aligned} \tag{4.16}$$

Once again applying the sifting property of the delta function equation #4.15 becomes:

$$\begin{aligned}
R_I(x_i, x_i'') &= \int \int_{-\infty}^{\infty} \{ |\bar{O}(x_o)|^2 |\bar{O}(x_o'')|^2 \\
&\quad h(x_i - Mx_o) h^*(x_i' - Mx_o) h(x_i'' - Mx_o'') h^*(x_i''' - Mx_o'') \\
&\quad + |\bar{O}(x_o)|^2 |\bar{O}(x_o'')|^2 \\
&\quad h(x_i - Mx_o) h^*(x_i''' - Mx_o) h(x_i'' - Mx_o'') h^*(x_i' - Mx_o'') \} \\
&\quad d^2 x_o d^2 x_o'' \quad (4.17)
\end{aligned}$$

After substituting the expression for the impulse response Eq.#4.2 into Eq.#4.17, the first summation of this equation is seen to be just the average intensity squared.

$$\begin{aligned}
&= K^4 \int \int_{-\infty}^{\infty} |\bar{O}(x_o)|^2 |\bar{O}(x_o'')|^2 \quad (4.18) \\
&\quad \times \left\{ \int_{-\infty}^{\infty} |P(x_p)|^2 e^{-\frac{jk}{a_i}(x_i - x_i')x_p} |P(x_p)|^2 e^{-\frac{jk}{a_i}(x_i'' - x_i''')x_p} d^2 x_p \right. \\
&\quad \left. + \int_{-\infty}^{\infty} |P(x_p)|^2 e^{-\frac{jk}{a_i}(x_i - x_i''')x_p} |P(x_p)|^2 e^{-\frac{jk}{a_i}(x_i'' - x_i')x_p} d^2 x_p \right\} d^2 x_o d^2 x_o'' \\
&\quad \text{let } x_i = x_i' \\
&\quad \text{and } x_i'' = x_i'''
\end{aligned}$$

$$= \langle I(x_i) \rangle \langle I(x_i'') \rangle \left(1 + \int_{-\infty}^{\infty} |P(x_p)|^2 e^{-\frac{jk}{a_i}(x_i - x_i'')x_p} d^2 x_p \right) \quad (4.19)$$

Goodman refers to the squared magnitude term as the mutual intensity of the field and is analogous to the terminology in classical coherence theory.

$$= \langle I(x_i) \rangle^2 (1 + |\gamma(\Delta x)|^2) \quad (4.20)$$

Both the autocorrelation of the amplitude and intensity will become important in determining the speckle size and phase error determination.

4.1 Experimental Measurement of Intensity

In actual measurement schemes, the statistics may differ somewhat from the ideal. The intensity measurements made in holographic interferometric will typically be an integrated effect over a large number of speckles with a detector of finite size. The current output by a photo-detector turns out to be directly proportional to the incident power.

$$i = \frac{\eta q P}{h \nu} \quad (4.21)$$

P = is the incident power

q = electron charge

η = detector efficiency

h = Planck constant

ν = frequency of the light

The average power seen by the detector is an integration of the intensity over the illuminated detector area.

$$\langle P \rangle = \langle \int_{-\infty}^{\infty} D(x_i) I(x_i) d^2 x_i \rangle \quad (4.22)$$

$D(x_i)$ = weighting function of the detector aperture

$$A_D = \int_{-\infty}^{\infty} D(x_i) d^2 x_i$$

= detector area

The result, as may be expected, for the average power is simply the average intensity times the detector area.

$$\langle P \rangle = A_d \langle I(x_i) \rangle \quad \text{average detector power} \quad (4.23)$$

Again, the second statistical property to determine is the second moment of the optical power. This quantity is similar to the expression for the second moment of the intensity in equation 4.14.

$$\langle P^2 \rangle = \langle \int \int_{-\infty}^{\infty} D(x_i) D(x'_i) I(x_i) I(x'_i) d^2 x_i d^2 x'_i \rangle$$

$$\langle P^2 \rangle = \int \int_{-\infty}^{\infty} \langle D(x_i) D(x'_i) \rangle \langle I(x_i) I(x'_i) \rangle d^2 x_i d^2 x'_i \quad (4.24)$$

Since, the autocorrelation function is only dependent upon the spatial coordinate differences, a substitution of variables is appropriate.

$$\Delta x = x_i - x'_i$$

The term $R_I(\Delta x)$ is the autocorrelation of the intensity taken from the earlier development (Eq. #4.20) and $R_D(\Delta x)$ represents the autocorrelation of the binary detector function.

$$R_D(\Delta x) = \int_{-\infty}^{\infty} D(x_i) D(x_i - \Delta x) d^2 x_i \quad (4.25)$$

$$R_I(\Delta x) = \langle I \rangle^2 \{1 + |\gamma(\Delta x)|^2\}$$

Substituting these two expressions (Eq. #4.20 & Eq. #4.25) into Eq. #4.24 produces the following:

$$\langle P^2 \rangle = \int_{-\infty}^{\infty} R_D(\Delta x) R_I(\Delta x) d^2 \Delta x \quad (4.26)$$

where

$$\langle P^2 \rangle = \langle I \rangle^2 \int_{-\infty}^{\infty} R_D(\Delta x) d^2 \Delta x + \langle I \rangle^2 \int_{-\infty}^{\infty} R_D(\Delta x) |\gamma(\Delta x)|^2 d^2 \Delta x \quad (4.27)$$

Further examination of the two terms in Eq. #4.27 reveals that the integral in the first term reduces to the square of the detector area. Closely examining the second integral, one finds that the optical transfer function rapidly falls to zero for small variations of the spatial parameter Δx and is much more narrow than the autocorrelation of the detector function. In this narrow region, $R_D(\Delta x)$ remains practically constant and can be factored out of the integral.

$$\int_{-\infty}^{\infty} R_D(\Delta x) d^2 \Delta x = A_D^2 \quad (4.28)$$

$$R_D(0) = A_D$$

$$\begin{aligned} \langle P^2 \rangle &= A_D^2 \langle I \rangle^2 + \langle I \rangle^2 R_D(0) \int_{-\infty}^{\infty} |\gamma(\Delta x)|^2 d^2 \Delta x \\ \langle P^2 \rangle &= A_D^2 \langle I \rangle^2 + \langle I \rangle^2 A_D \int_{-\infty}^{\infty} |\gamma(\Delta x)|^2 d^2 \Delta x \\ &= A_D^2 \langle I \rangle^2 \left\{ 1 + \frac{\sigma_s}{A_D} \right\} \end{aligned} \quad (4.29)$$

$$\text{where } \sigma_s = \int_{-\infty}^{\infty} |\gamma(\Delta x)|^2 d^2 \Delta x$$

In Gaussian statistics, the variance can be considered to be the AC portion of the output and is expressed by the second central moment.

$$\sigma_P^2 = \langle P^2 \rangle - \langle P \rangle^2 \quad (4.30)$$

$$\sigma_P^2 = \langle I \rangle^2 A_D \int_{-\infty}^{\infty} |\gamma(\Delta x)|^2 d^2 \Delta x \quad (4.31)$$

This quantity is commonly used in the expression for the RMS signal-to-noise ratio, where the square root of the second central moment of the power is divided by the mean power squared. Goodman refers to the reciprocal of the *SNR* as the contrast,

which is of considerable experimental interest.

$$SNR_{rms} = \sqrt{\frac{\sigma_p^2}{\langle P \rangle^2}} = \sqrt{\frac{\int_{-\infty}^{\infty} |\gamma(\Delta x)|^2 d^2 \Delta x}{A_D}} \quad (4.32)$$

$$\text{contrast}^2 = SNR_{RMS}^{-2} = \frac{\langle P \rangle^2}{\sigma_p^2} = \frac{A_D}{\int_{-\infty}^{\infty} |\gamma(\Delta x)|^2 d^2 \Delta x} = \frac{A_D}{\sigma_s} = N \quad (4.33)$$

Understanding equation #4.33 brings some physical significance to the nature of the phenomenon. The numerator, obviously, is the detector area with the appropriate units; the denominator also has units of area and can be taken as the area of a single correlation cell. This correlation cell is really an expression for the average speckle size and the average speckle diameter is defined to be the value when autocorrelation function first goes to zero. This measure of average speckle size is used in determining the average number of individual speckles on the active detector area. As seen in equation #4.33, the signal-to-noise ratio is indirectly proportional to the number of speckles N . In a later section, the number of speckles N will also be shown to be critical in the phase error determination.

5 Interferometry of Diffuse Objects

In holographic interferometry, the hologram stores one or both of the images to be interferometrically compared. The desired result is to image the object deformation as contour fringes owing to the constructive and destructive interference of the overlapping object waves. The output image is the superposition of these two coherent images. Since both are coherent, the measured intensity in the image plane is given by the squared magnitude of the amplitude sum.

$$\begin{aligned} \langle |V_1 + V_2|^2 \rangle &= \langle I_1 \rangle + \langle I_2 \rangle + 2 \operatorname{Re} \langle V_1 V_2^* \rangle \\ &= \langle I_1 \rangle + \langle I_2 \rangle + 2 \langle I_{12} \rangle \cos(\phi + \delta\phi) \end{aligned} \quad (5.1)$$

The first two terms of this expression can be considered as simply DC offsets or mean background illumination about which the interference term fluctuates. The last term in equation #5.1 is the interference term in which the useful phase or displacement information is contained. This mutual intensity term is the cross-correlation of the two image amplitudes.

$$\begin{aligned} \langle I_{12}(x_i) \rangle &= \langle V_1(x_i) V_2^*(x_i') \rangle \\ &= \int \int_{-\infty}^{\infty} \langle \bar{O}_1(x_o) \bar{O}_2^*(x_o') \rangle \langle \rho_1(x_o) \rho_2^*(x_o') \rangle \\ &\quad \times h(x_i - Mx_o) h^*(x_i' - Mx_o') d^2 x_o d^2 x_o' \end{aligned} \quad (5.2)$$

Performing interferometry of diffuse objects requires that the two interfering wavefronts be identical wavefronts, or at least similar on a microscopic level

$\langle \rho_1(x_o) \rho_2^*(x_o') \rangle \neq 0$ in order to observe macroscopic interference. That is to say that the two speckle patterns from the respective images must be correlated to successfully produce fringe contours. Coherent light will always interfere on a microscopic level producing speckle, but the degree to which the two images correlate will dictate the ability to measure the deformation. Insufficient correlation will degrade the fringe contrast reducing the accuracy of the displacement measurement.

The first assumption in calculating the mutual intensity is that the surface morphology remains the same and that a reduction in image correlation is solely due to an image translation or shift. The image amplitude of the deformed object can then be represented by an in-plane translation u_i and an optical path length change $\phi(x_i)$.

$$V_2(x_i) = V_1(x_i + u_i) e^{-i\phi(x_i)} \quad (5.3)$$

$$\phi(x_i) = \vec{u} \cdot \vec{k} \quad (5.4)$$

\vec{k} = sensitivity vector

\vec{u} = object displacement vector

$$u_i = M(\vec{u} \cdot \vec{x}_o) \quad (5.5)$$

\vec{x}_o = in-plane object motion

M = image magnification

The in-plane object motion corresponds to speckle translation and can be accounted for in the impulse response of the imaging system.

$$V_2(x_i) = e^{-j\phi(x_i)} \int_{-\infty}^{\infty} \bar{O}(x_o) \rho(x_o) h(x_i + u_i - Mx_o) d^2 x_o \quad (5.6)$$

The amplitude cross-correlation is determined in the same manner as the autocorrelation that was shown in equation #4.6.

$$\begin{aligned} \langle I_{12}(x_i) \rangle = & e^{j\phi(x_i)} \int \int_{-\infty}^{\infty} \langle \bar{O}(x_o) \bar{O}^*(x_o') \rangle \langle \rho(x_o) \rho^*(x_o') \rangle \\ & \times h(x_i - Mx_o) h^*(x_i' + u_i - Mx_o') d^2 x_o d^2 x_o' \quad (5.7) \end{aligned}$$

$$\langle I_{12}(x_i) \rangle = e^{j\phi(x_i)} \int_{-\infty}^{\infty} |\bar{O}(x_o)|^2 h(x_i - Mx_o) h^*(x_i' + u_i - Mx_o) d^2 x_o \quad (5.8)$$

Making the appropriate substitutions and manipulations as was done in equations 4.8 and 4.10, the mutual intensity takes on the form in equation (5.9). Here, the intensity measurement is shown to be a function of the object illumination, optical path length change $\phi(x_i)$ and the in-plane object motion u_i .

$$= |\bar{O}|^2 e^{j\phi(x_i)} \gamma(u_i) \quad (5.9)$$

Ideally, it would be nice if the measured intensity, equation (5.10), could directly determine the object displacement or optical path length change. However, any object motion that is not directly along the viewing direction is going to degrade fringe contrast, thus reducing the ability to accurately determine $\phi(x_i)$. Fringe interpolation techniques such as heterodyne or quasi-heterodyne holographic interferometry eliminate the dependence on this contrast term.

$$\langle |V_1 + V_2|^2 \rangle = 2 \langle I \rangle \{ 1 + \gamma(u_i) \cos(\phi + \delta\phi) \} \quad (5.10)$$

$$\gamma(u_i) = \frac{2J_1\left(\frac{\pi u_i D}{\lambda d_i}\right)}{\left(\frac{\pi u_i D}{\lambda d_i}\right)} \quad (5.11)$$

The fringe contrast or modulation term has been examined previously in section 4. For circular optics, the correlation term is a first order Bessel function divided by its' argument. The average speckle size or diameter is defined by this quantity and takes on the value of the distance to the first zero crossing of the first order Bessel function. Physically, this means that if the in-plane object motion were one speckle diameter, then the correlation or fringe visibility $\gamma(u_i)$ in the image plane would be reduced to zero. This image motion can be manifested through optical misalignment, wavelength change, imaging aberrations, and object movement.

$$\begin{aligned} \frac{\pi u_i D}{\lambda d_i} &= 3.83 \\ u_i &= \frac{1.22 \lambda d_i}{D} \\ &= \text{avg. speckle diameter} \end{aligned} \quad (5.12)$$

5.1 Heterodyne Intensity

Heterodyne holographic interferometry offers the ability to accurately determine the phase or displacement information to within 2000th of a wavelength independent of illumination and depth of fringe modulation. A considerable advantage

owing to the interference of two correlated images of slightly different wavelengths. The interferogram, which is formed, is no longer a static fringe pattern, but rather is modulated at the difference frequency of the two mixed images.

$$\begin{aligned}
 I_{12} &= e^{-j\Delta\omega t} I_{12}(x_i) \\
 &= |\bar{O}|^2 e^{-j\{\Delta\omega t + \phi(x_i)\}} \gamma(u_i)
 \end{aligned} \tag{5.13}$$

Acousto-optic modulators provide the fixed and controllable frequency shift for the respectful images. The difference frequency is chosen so that the modulated intensity can be easily measured with a photo-detector. Processing the photo-detector signal is performed with an electronic phase meter that has the ability of accurately measuring the phase variations $\phi(x_i)$ independent of the amplitude variations. Such off the shelf electronics can easily operate at a frequency of 100kHz with a phase accuracy of 0.1 degrees.

$$\langle I \rangle = A(x_i) \{ 1 + m(x_i) \cos(\Delta\omega t + \phi(x_i) + \delta\phi) \} \tag{5.14}$$

Hence, if the electronics were the only limiting factor, the out-of-plane displacement resolution would be 3600th of a wavelength or about 1.4 angstroms.

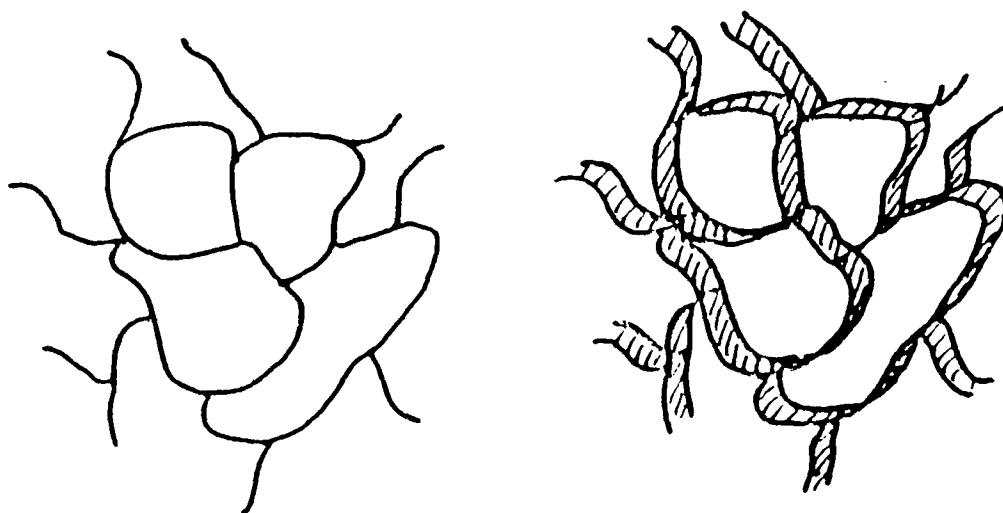
5.2 Statistical Phase Error

As was shown in intensity section, one of the limiting aspects to holographic interferometry is the translation of the interfering speckle images causing a reduction in the fringe contrast and inhibiting an accurate phase measurement. Heterodyning offers a technique for measuring the phase independent of the intensity fluctuations. However, heterodyne techniques are not ideal solutions without inherent statistical errors. Again, it is observed that the uncorrelated speckle pattern has a detrimental effect on the phase accuracy measurement. The random phase error encountered in heterodyning is also present in the straight forward case of holographic interferometry, but normal intensity measurements lack the resolution for it to be problem. However, in the heterodyne case, the phase sensitivity is great enough so that the statistical phase error owing to the uncorrelated speckle pattern has a detrimental effect.

Ideally, the output of the photo-detector would be just the true ensemble average of the incident power (Eq. #5.15).

$$\begin{aligned} \langle P_{12} \rangle &= \left\langle \int_{-\infty}^{\infty} D(x_i) I_{12}(x_i) d^2 x_i \right\rangle \\ &= \langle I_{12} \rangle A_D \gamma(u_i) \end{aligned} \quad (5.15)$$

However, the output current, processing both phase and amplitude information, is slightly deviated due to the imperfect registry of the speckle pattern. As illustrated in figure #5.1, the overlap region of neighboring speckles, owing to an image translation, introduces the random phase term in the measurement process. This power deviation measurement can be expressed as the difference between the detected



Overlapping regions of neighboring speckles
caused by an image translation (Wagner, 1984).

FIGURE #5.1

intensity and ideal ensemble average. The difference arises since there are only a finite number of speckles on the detector area. Like before, the speckle is a random process and the phase error that is introduced is also a random error (Fig. #5.2).

$$\delta P = P_{12} - \langle P_{12} \rangle \quad (5.16)$$

$$\langle \phi(x_i) \rangle = 0$$

Since only the perpendicular component of the power deviation contributes to the phase error, an approximation (Eq. #5.17) for the phase error can be written assuming an average overall phase of $\langle \phi(x_i) \rangle = 0$.

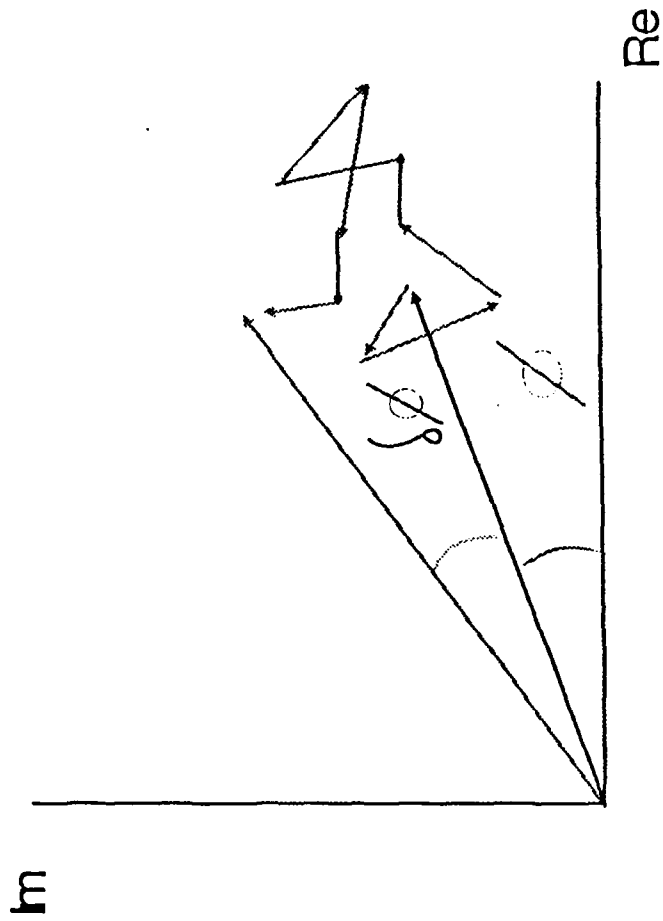
$$\delta \phi \cong \tan(\delta \phi) = \frac{\text{Im}(P_{12})}{\text{Re}(P_{12})} \cong \frac{\text{Im}(P_{12})}{\langle P_{12} \rangle} \quad (5.17)$$

$$\text{where } \langle P_{12} \rangle \cong P_{12}$$

The mean square phase error in the heterodyne signal is then given in equation #5.18.

$$\langle \delta \phi^2 \rangle = \frac{\langle \text{Im}^2 P_{12} \rangle}{\langle P_{12} \rangle^2} = \frac{1}{2} \frac{\langle |P_{12}|^2 \rangle - \langle P_{12}^2 \rangle}{\langle P_{12} \rangle^2} \quad (5.18)$$

Drawing from the fundamentals in the intensity measurement section, the three terms $\langle P_{12}^2 \rangle$, $\langle |P_{12}|^2 \rangle$, $\langle P_{12} \rangle^2$ can be determined. The expression for $\langle P_{12} \rangle$ has been given in equation #5.15. The other two terms can be determined from past understanding of the autocorrelation of the intensity.



Interference phase measurement error resulting
from the speckle misalignment
Figure #5.2

$$\begin{aligned}
\langle P_{12}^2 \rangle &= \int \int_{-\infty}^{\infty} R_D(\Delta x) R_I(u_i) d^2 \Delta x \\
&= \langle I \rangle \left(1 + \frac{\sigma_s}{A_D} |\gamma(u_i)|^2 \right)
\end{aligned} \tag{5.19}$$

$$\begin{aligned}
\langle |P_{12}^2|^2 \rangle &= \int \int_{-\infty}^{\infty} R_D(\Delta x) R_I(\Delta x) d^2 \Delta x \\
&= \langle I \rangle \left(1 + \frac{\sigma_s}{A_D} \right)
\end{aligned} \tag{5.20}$$

For a real valued crosscorrelation function, the mean square phase error can be written as:

$$\begin{aligned}
\langle \Delta \phi^2 \rangle &= \frac{1}{2} \frac{\sigma_s}{A_D} \frac{1 - \gamma^2(u_i)}{\gamma^2(u_i)} \\
&= \frac{1 - \gamma^2}{2N\gamma^2}.
\end{aligned} \tag{5.21}$$

This agrees with the value given by Dandliker in his review paper in 1980. Subsequently, Thalman has published a paper with a slightly different value (Eq. #5.22) (Thalman et al. 1986).

$$\langle \Delta \phi^2 \rangle = \frac{1 - \gamma(2u_i)}{2N\gamma^2(u_i)} \tag{5.22}$$

However, for an image correlation of 70%, Thalman's method in equation #5.22 predicted a phase error 25% higher. For this study, it was assumed that either

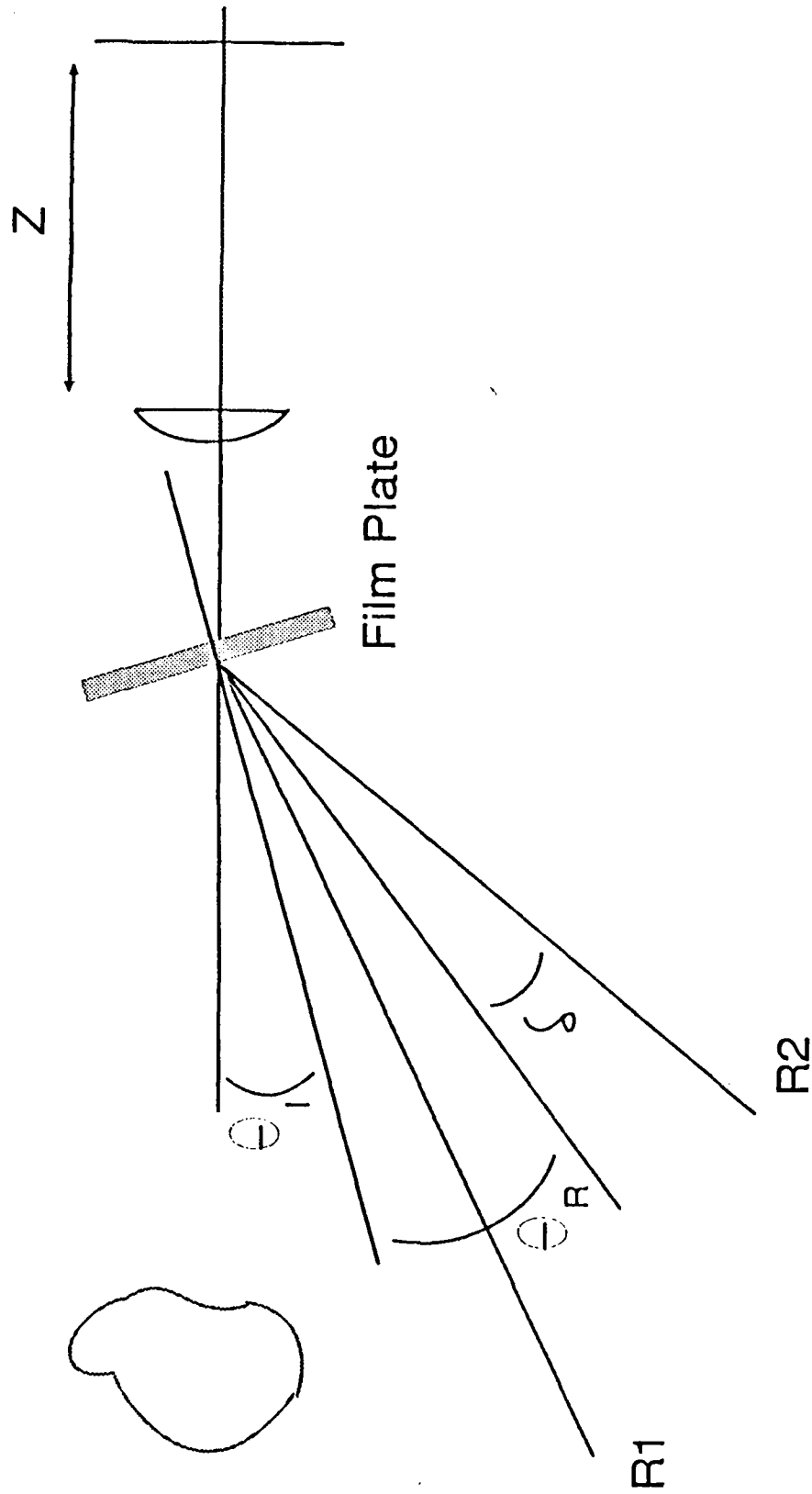
method would pose no serious experimental changes or difficulties, since the differences were minor.

6 Misalignment of the Holographic Images

The degree of registry or correlation between the two interfering images has been determined to be a major factor in minimizing the phase error in heterodyne analysis. Proper registry of the two reconstructed images depends upon the equivalence of the constructing and reconstructing wavefronts. While the two reference beam configuration for constructing a double exposed hologram facilitates heterodyne analysis, it also complicates the system by imposing stringent alignment restrictions. A common design constraint of a 70% correlation factor mandates that the in-plane image misalignment be less than half a speckle diameter. Achieving this design goal becomes an opto-mechanical configuration problem. The design of the system must take into account the speckle size, the object distance, the wavelength change, the angle separation between the dual reference beams, and the collimation quality. All these variables have a direct effect on the image location and hence the associated measurement resolution.

The angular misalignment between the two reference beams is something to which all heterodyne holographic configurations are susceptible. Dandliker goes through an analysis based on a wave vector approach to describe the tolerances involved (Dandliker et al. 1976). However, the approach taken in this treatise will follow the development of Wagner (Wagner 1984). Both are equally well founded.

In Wagner's analysis, the hologram is treated as a complex diffraction grating, where two separate gratings have been recorded holographically. The reconstructed images are merely the first order diffraction patterns obeying Bragg's law (Fig. #6.1). The angular position of the image is a function of the wavelength λ , the



Dual Reference Beam Holographic Set-up
Figure #6.1

median angle of the reference beams θ_r and the grating spacing α_1 and α_2 (Eq. #6.1). The angular separation of the reference beams is defined to be 2δ , and θ_o is the direction of the object beam.

$$\lambda = \alpha_1 \{ \sin(\theta_r - \delta) + \sin \theta_o \} \quad (6.1a)$$

$$\lambda = \alpha_2 \{ \sin(\theta_r + \delta) + \sin \theta_o \} \quad (6.1b)$$

When a heterodyne holographic system is designed for maximum sensitivity this necessitates that the angle between the two reference beams, 2δ , be greater than the angular extent of the reconstructed image. This ensures that there are no unwanted images superimposed on the interfering images of interest. However, for stability purposes, a smaller angle between the reference beams is more favorable. This can be shown by introducing a small angular deviation $\Delta\delta$ between the reference beams and solving for the resultant perturbation in the object beam angle.

$$\sin \theta_o - \sin(\theta_o + \Delta\theta_{o1}) = \left\{ \frac{\lambda}{\alpha_1} - \sin(\theta_r - \delta) \right\} - \left\{ \frac{\lambda}{\alpha_1} - \sin(\theta_r - (\delta + \Delta\delta)) \right\}$$

$$\sin \theta_o - \sin(\theta_o + \Delta\theta_{o2}) = \left\{ \frac{\lambda}{\alpha_2} - \sin(\theta_r - \delta) \right\} - \left\{ \frac{\lambda}{\alpha_2} - \sin(\theta_r + (\delta + \Delta\delta)) \right\}$$

$$\Delta\theta_{o1} = \Delta\delta \frac{\cos(\theta_r - \delta)}{\cos \theta_o}$$

$$\Delta\theta_{o2} = \Delta\delta \frac{\cos(\theta_r + \delta)}{\cos \theta_o}$$

$$\begin{aligned}
 \Delta\theta_o &= \Delta\theta_{o1} + \Delta\theta_{o2} \\
 &= 2\Delta\delta \cos\delta \frac{\cos\theta_r}{\cos\theta_o}
 \end{aligned} \tag{6.2}$$

To simplify this expression further, it will be assumed that the angular deviation of the object beam $\Delta\theta_o$ is small and that $\theta_r = \theta_o$.

$$u_i \cong z\Delta\theta = 2z\Delta\delta \cos\delta \tag{6.3}$$

The expression in equation #6.3 relates the in plane image translation u_i to the allowable angular deviation $\Delta\delta$. For an image distance of $z = 30\text{cm}$, optics diameter of 7.5cm , a correlation of $\gamma \cong 0.7$, $\delta = 8^\circ$, $\lambda = 0.5145\mu\text{m}$, the allowable angular misalignment allowed between the reference beams is

$$\Delta\delta \cong 0.0001^\circ$$

Commercially available optical mounts are able to meet this type of tolerance range, but at this level regular optical realignment is necessary to compensate for temperature fluctuations in the laboratory. Many researchers in the field accept a reduction in sensitivity by using a small separation angle 2δ allowing the images to overlap somewhat, but in the process achieving better optical stability.

A similar angular misalignment is encountered when a change in wavelength is necessary. This is typically confronted when a pulsed laser is used in creating the hologram and a cw laser is needed for the reconstruction process. The difference in

wavelengths is enough to cause an image translation, the amount of which is dependent on the separation angle between the two reference beams. Determining the positional change for the object employs the same mathematical development as was done to determine the angular stability. This analysis introduces a perturbation in the wavelength to observe the effect on the angular position of the object.

$$\sin \theta_o - \sin(\theta_o + \Delta \theta_o) = \left\{ \frac{\lambda_1}{a_1} - \sin(\theta_r - \delta) \right\} - \left\{ \frac{\lambda_2}{a_1} - \sin(\theta_r - \delta) \right\}$$

$$\Delta \theta_{o1} = \frac{\lambda_1 - \lambda_2}{a_1 \cos \theta_o}$$

$$\Delta \theta_{o2} = -\frac{\lambda_1 - \lambda_2}{a_2 \cos \theta_o}$$

$$\Delta \theta_o = \Delta \theta_{o1} + \Delta \theta_{o2}$$

$$= \frac{\lambda_1 - \lambda_2}{a_1 \cos \theta_o} - \frac{\lambda_1 - \lambda_2}{a_2 \cos \theta_o}$$

$$= \frac{\lambda_1 - \lambda_2}{\cos \theta_o} \frac{a_1 - a_2}{a_1 a_2}$$

$$\Delta \theta_o = 4 \frac{\lambda_1 - \lambda_2}{\lambda_1} \left(\frac{\cos \theta_r}{\cos \theta_o} \right) \sin \frac{\delta}{2} \quad (6.4)$$

Again the simplification is made where it is assumed that the perturbation $\Delta \theta_o$ is small and that the object and reference angles are equal; there by allowing an expression to be written for the in plane image translation owing to a wavelength change (Eq. #6.5).

$$u_i \cong z \Delta \theta_o \cong 4 \frac{\lambda_1 - \lambda_2}{\lambda_1} \sin \frac{\delta}{2} \quad (6.5)$$

This translation is again dependent upon the angular separation of the two reference beams. Reducing this separation will in return reduce the deviation caused by the wavelength shift. For example, for the same optical set-up of $\gamma \cong 0.7$, $z = 30 \text{ cm}$, $D = 7.5 \text{ cm}$, $\delta = 8^\circ$, $\lambda_1 = 0.532 \mu\text{m}$, $\lambda_2 = 0.5145 \mu\text{m}$, the in plane translation would be 2.75mm. The results in a 0.5° change of the reconstruction beam angle to compensate for the wavelength shift, a tedious procedure that several researchers have avoided by accepting a reduction in phase sensitivity in order to relax the alignment restrictions. In order to achieve this relaxation, the angular separation δ of the reference beams must be less than 0.004° . Obviously, such a small separation angle for the reference beams would produce overlapping images.

Another consideration for proper image registry is the equivalence of the reconstructing wavefronts. The usual assumption is that these wavefronts are both collimated and Gaussian, an ideal situation that may not be achieved experimentally. Deviations from the ideal can cause image magnifications and phase distortions. A image magnification of 1.0001 for an object distance of 300m will result in a usable image area of about a 2cm diameter. Outside this area the image decorrelation will be too severe to permit heterodyne interferometric analysis. Analysis of image magnification was originally formulated for the application of microscopy by Gabor, the father of holography (Gabor 1949,1951). Since then, development of two wavelength holographic contouring has provided insight into this phenomenon (Hildebrand & Haines 1967, Zelenka & Varner 1968). Contouring was the first branch of holography to seriously consider the detrimental effects of image decorrelation with respect to a wavelength shift.

This treatise will follow Goodman's development for the mathematical treatment of wavelength changes, uncollimated reference waves and holographic imaging. The object and reference waves are assumed to be spherical point sources and located at (x_o, y_o, z_o) and (x_r, y_r, z_r) respectively. It is also assumed that these point sources can be approximated in the quadratic form (Eq. #6.6a&b).

$$O = A_o \exp \left\{ j \frac{\pi}{\lambda_1 z_o} [(x - x_o)^2 + (y - y_o)^2] \right\} \quad (6.6a)$$

$$R = A_r \exp \left\{ j \frac{\pi}{\lambda_1 z_r} [(x - x_r)^2 + (y - y_r)^2] \right\} \quad (6.6b)$$

Referring back to the section on holographic construction, the transmittance of the film plate can be expressed as

$$T = \alpha (|O|^2 + |R|^2 + OR^* + RO^*)$$

where α is the proportionality constant owing to the film characteristics. If the hologram is reconstructed with the reference wave

$$B = A_b \exp \left\{ j \frac{\pi}{\lambda_1 z_r} [(x - x_r)^2 + (y - y_r)^2] \right\}$$

then the reconstructed virtual image will have the form

$$\begin{aligned}
 U_3 = & \alpha A_b A_r^* A_o \exp \left\{ j \frac{\pi}{\lambda_2 z_b} [(x - x_b)^2 + (y - y_b)^2] \right. \\
 & - j \frac{\pi}{\lambda_1 z_r} [(x - x_r)^2 + (y - y_r)^2] \\
 & \left. + j \frac{\pi}{\lambda_1 z_o} [(x - x_o)^2 + (y - y_o)^2] \right\}. \quad (6.7)
 \end{aligned}$$

This reconstruction wave has the possibility of a change in wavelength and in point source position. Since the reconstructed image is presumed to be a point source and only linear and quadratic terms are observed in U_3 , then U_3 may be regarded as a quadratic approximation to a spherical wave (Eq. #6.8).

$$U_i = C \exp \left\{ j \frac{\pi}{\lambda z_i} [(x - x_i)^2 + (y - y_i)^2] \right\} \quad (6.8)$$

If the linear and quadratic terms are collected in U_3 and then compared to U_i , the exact location of the image can be determined. First equate the quadratic terms to obtain information as image z_i (6.9).

$$\begin{aligned}
 \frac{\pi}{\lambda_2 z_i} (x^2 + y^2) &= \left\{ \frac{\pi}{\lambda_2 z_b} - \frac{\pi}{\lambda_1 z_r} + \frac{\pi}{\lambda_1 z_o} \right\} (x^2 + y^2) \\
 z_i &= \left\{ \frac{1}{z_b} - \frac{\lambda_2}{\lambda_1 z_r} + \frac{\lambda_2}{\lambda_1 z_o} \right\}^{-1} \quad (6.9)
 \end{aligned}$$

The x_i, y_i image coordinates are obtained by equating the linear terms (6.10a&b).

$$\begin{aligned} \frac{2\pi}{\lambda_2 z_i} (xx_i + yy_i) &= \frac{2\pi}{\lambda_2 z_b} (xx_b + yy_b) \\ &+ \frac{2\pi}{\lambda_1} z_o (xx_o + yy_o) \\ &- \frac{2\pi}{\lambda_1} z_r (xx_r + yy_r) \end{aligned}$$

$$x_i = \frac{z_i}{z_b} x_b + \frac{\lambda_2 z_i}{\lambda_1 z_o} x_o - \frac{\lambda_2 z_i}{\lambda_1 z_r} x_r \quad (6.10a)$$

$$y_i = \frac{z_i}{z_b} y_b + \frac{\lambda_2 z_i}{\lambda_1 z_o} y_o - \frac{\lambda_2 z_i}{\lambda_1 z_r} y_r \quad (6.10b)$$

An important parameter in holographic interferometry is the amount of lateral shift or image magnification. For a given change in the object point location, the corresponding image change is expressed by equation #6.11a&b.

$$\Delta x_i = \frac{\lambda_2 z_i}{\lambda_1 z_o} \Delta x_o \quad (6.11a)$$

$$\Delta y_i = \frac{\lambda_2 z_i}{\lambda_1 z_o} \Delta y_o \quad (6.11b)$$

The magnification is expressed in equation #6.12.

$$M = \left| \frac{\Delta x_i}{\Delta x_o} \right| = \left| \frac{\Delta y_i}{\Delta y_o} \right| = \left| \frac{\lambda_2 z_i}{\lambda_1 z_o} \right| \quad (6.12)$$

For the ideal case of perfectly collimated wavefronts for the reference and recon-

struction beams, $z_r = z_b = \infty$, the lateral magnification is equal to unity, regardless of the change in wavelength. Similarly, if the same optical set-up is used for both the hologram construction and reconstruction process, $z_b = z_r; \lambda_2 = \lambda_1$, then the magnification also results in a unity value. The design goal in the dual reference beam configuration then is to maintain a matching wavefront condition in order to minimize lateral magnification. Citing the same optical example again, for a

$\gamma \cong 0.7$, $z = 30\text{ cm}$, $D = 7.5\text{ cm}$, and $\lambda = 0.5145\mu\text{m}$, the minimum reconstruction point must appear at least 3000m away from the film plate for there to be sufficient image correlation in a circle 20mm diameter in the image plane.

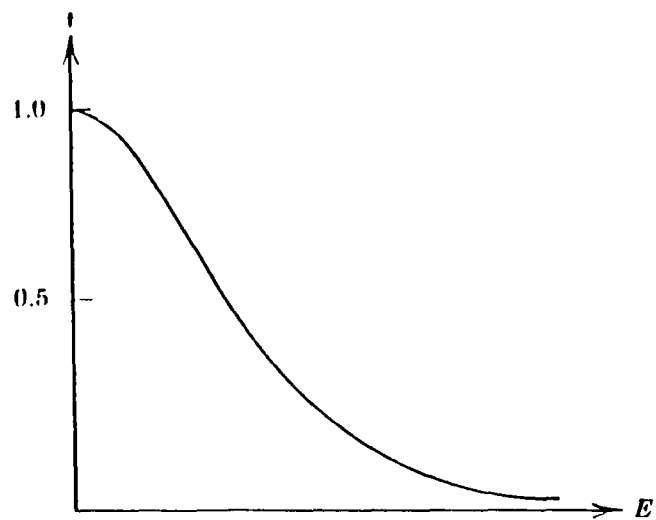
7 Film Effects

In heterodyne holographic interferometry, an accurate recording of the object position is critical in determining relative out of plane displacements. Exposure and resolution considerations are often ignored in the normal homodyne case of holographic interferometry, since these effects may not be detrimental. However, in resolving phase fronts to 0.2 degrees, requires certain details may not be overlooked.

7.1 Exposure Characteristic

Typically, the recording of a hologram is assumed to be a linear process. A film plate is placed in the plane of intersection between the diffusely reflected object wave and the reference wave. The film records this complex interference pattern, which possesses both phase and amplitude information. A useful plot in determining the proper exposure level is the transmittance vs. exposure curve (Fig. #7.1). This curve describes the transmission function of the hologram after development (Kozma 1970). The slope of the linear portion of this curve can be varied with the exposure time and development process (Friesem 1967, Kozma 1966). If the amplitude of the reference beam is much greater than the object beam and the film is biased to an appropriate level on the t-E curve, then it may be possible to assume that the transmittance of the film plate is indeed a linear mapping of the exposure intensity.

$$t \cong t_b + \beta(E - E_b) \quad (7.1)$$



*Typical transmittance-exposure curve
for a negative transparency.*
(Goodman, 1968)

FIGURE #7.1

The equation #7.1 describes the linear portion of the t-E curve, where t is the total transmittance, t_b is the transmittance bias, β is the slope of the curve at the bias point, E_b is the bias exposure, and E is the total energy to which the film was exposed. For double exposure, dual reference beam holographic interferometry, the total energy incident on the film plate is

$$E = T \{ |O_1 + R_1|^2 + |O_2 + R_2|^2 \} \quad (7.2a)$$

$$= T \{ (R_1)^2 + (R_2)^2 + (O_1)^2 + (O_2)^2 + R_1 O_1^* + R_1^* O_1 + R_2 O_2^* + R_2^* O_2 \} \quad (7.2b)$$

where $O_{1,2}$ and $R_{1,2}$ are the amplitudes of the object and reference waves for the respective exposures, T is the exposure time and is assumed constant for both exposures. The first four terms of equation #7.2b contribute to the exposure bias term. When the developed film plate is re-illuminated by the reference beams, the last four terms of this expression form the reconstructed images. Each reference beam will reconstruct four images resulting in a total of eight, of which only two at only one time are of interest and used. The use of two reference beams allows the use of heterodyne techniques to evaluate the phase difference between the two images. Because of the increase in resolution with heterodyne holographic interferometry the linear model may not be adequate in accounting for the additional phase errors that may occur.

7.2 Non-linear Considerations

Taking into account the non-linear nature of photographic film, as evidenced by the t-E curve, is sometimes necessary in HHI (Eq. #7.3).

$$t = t_b + \beta_1 (E - E_b) + \beta_2 (E - E_b)^2 + \dots \quad 7.3$$

However, these non-linear terms can lead to unwanted cross-talk in reconstructed images in dual reference beam holographic interferometry. This cross-talk is manifested in a spurious fringe pattern that produces an undesirable phase error measurement in the detection system. This caveat can be avoided by eliminating any unperturbed regions on the object, which may not always be possible, or by careful control of the object to reference beam ratios. Dandliker and Ineichen have devised a simple experimental method by which the phase error introduced can be measured (Dandliker & Ineichen 1976). The testing method is based on the beam ratios before and after hologram construction.

First consider the reconstruction of the hologram with a transmittance function as proposed in equation #7.3 by reference beam #1. After expanding the various terms, the image amplitude is expressed as shown in equation #7.4. Reconstructing the hologram produces an increased number of terms owing to the non-linearity.

$$U_1 = |R_1|^2 T \{ \beta_1 O_1 + 2T\beta_2 O_1 O_1^* O_1 + 2T\beta_2 O_1 O_2^* O_2 \} \quad (7.4)$$

$$\begin{aligned} \bar{I}_{nm} &= \int O_n(x) O_m^*(x) d^2x \\ &= \gamma_{nm} \bar{I} \end{aligned}$$

Taking into account the statistical properties of the diffuse object results in the

expression shown in equation #7.5.

$$U_1 = |R_1|^2 T \{ (\beta_1 + 4T\beta_2 \bar{I}_{11} + 2T\beta_2 \bar{I}_{22}) O_1 + 2T\beta_2 \bar{I}_{12} O_2 \} \quad (7.5)$$

One will observe that reference beam #1 in this case has reconstructed an image of the second object state O_2 , undoubtedly, resulting in image cross talk proportional to the parameter β_2 . By a similar analysis, the reference beam R_1 reconstructs the alternate reference wavefront propagating in its' original direction (Eq. #7.6).

$$\tilde{R}_2 \cong 2T^2 \beta_2 |R_1|^2 \bar{I}_{12} R_2$$

The presence of O_2 on the reconstructed image U_1 produces the undesired cross-talk or spurious fringe pattern. The contrast of this detrimental fringe pattern can be expressed as a ratio of the reconstructed images (Eq. #7.7). It has been assumed that $\beta_1 \gg \beta_2$ and it is observed that the phase error increases for a greater depth of fringe modulation.

$$\begin{aligned} \kappa &= \left| \frac{4\bar{I}_{12} T \beta_2}{\beta_1} \right| \\ &= 4\alpha |\gamma_{12}| \end{aligned} \quad (7.7)$$

Experimentally, the quantity α can be determined through the comparison of the recorded and reconstructed intensities for object intensities and reference \tilde{R}_2 intensities (Eq. #7.8).

$$\frac{U_1}{O_1} \cong \beta_1 |R_1|^2 \quad \frac{\tilde{R}_2}{R_2} \cong 2T^2 \beta_2 |R_1|^2 \bar{I}_{12}$$

$$\alpha^2 |\gamma_{12}|^2 = \frac{1}{4} \frac{|O_1|^2 |\tilde{R}_2|^2}{|U_1|^2 |R_2|^2} \quad (7.8)$$

The fringe contrast κ can also be shown to be indicative of the phase error introduced because of the non-linear properties of the film. Following equation #7., reconstructing the hologram with both reference beams produces the reconstructed images as

$$U_1 = O_1 e^{j(\omega_1 t + \phi_1)} + \beta_{11} O_1 e^{j(\omega_1 t + \phi_1)} + \beta_{12} O_2 e^{j(\omega_1 t + \phi_2)} \quad (7.9a)$$

$$U_2 = O_2 e^{j(\omega_2 t + \phi_2)} + \beta_{22} O_2 e^{j(\omega_2 t + \phi_2)} + \beta_{21} O_1 e^{j(\omega_2 t + \phi_1)}, \quad (7.9b)$$

$$\beta_{11} = 2T \frac{\beta_2}{\beta_1} (2\bar{I}_{11} + \bar{I}_{22})$$

$$\beta_{22} = 2T \frac{\beta_2}{\beta_1} (2\bar{I}_{22} + \bar{I}_{11})$$

$$\beta_{12} = \beta_{21} = 2T \frac{\beta_2}{\beta_1} \bar{I}_{12}$$

and assuming that the different object states have the same illumination, $O_1 = O_2$, then

$$U_1 = O \left\{ e^{j(\omega_1 t + \phi_1)} + \beta_{11} e^{j(\omega_1 t + \phi_1)} + \beta_{12} e^{j(\omega_1 t + \phi_2)} \right\} \quad (7.10)$$

$$U_2 = O \left\{ e^{j(\omega_2 t + \phi_2)} + \beta_{22} e^{j(\omega_2 t + \phi_2)} + \beta_{21} e^{j(\omega_2 t + \phi_1)} \right\}. \quad (7.11)$$

The ac portion of the intensity distribution in the image plane can be expressed as

$$I_{ac} = 2 \operatorname{Re}(U_1 U_2^*) \\ \cong (1 + \beta_{22} + \beta_{11}) \cos(\Delta \omega t + \Delta \phi) + (\beta_{12} + \beta_{21}) \cos \Delta \omega t, \quad (7.12)$$

where the output is observed to be the summation of two sinusoids of the same frequency, but different phase. The error in the resultant phase measurement ϕ is dependent upon the non-linear amplitude contribution β_{12} (Eq #7.13).

$$\phi = \Delta \phi + \delta \phi_{error} \quad (7.13)$$

An expression for this phase error is found using a trigonometric identity to combine terms (Eq. #7.14).

$$\delta \phi_{error} = \tan^{-1} \frac{B \sin \Delta \phi}{A + B \cos \Delta \phi}, \quad (7.14)$$

$$\text{where } A = 1 + \beta_{11} + \beta_{22}$$

$$B = \beta_{12} + \beta_{21}$$

Also the assumption is made that $A \gg B$, which leads to a reasonable estimation of the phase error (Eq #7.15).

$$\begin{aligned}
\delta \phi_{error} &\cong B \sin \Delta \phi \\
\delta \phi_{error} &\leq (\beta_{12} + \beta_{21}) = \frac{4\beta_2 T \bar{I} \gamma_{12}}{\beta_1} \quad (7.15) \\
&= 2\alpha \gamma_{12}
\end{aligned}$$

Referring to equation #7.8, an experimental measurement of the maximum phase error that could occur can be determined. The two methods that can be employed to minimize this error are the reduction of the fringe contrast γ_{12} by a whole body object motion or by keeping the ratio of the object beam to reference beam intensity small. Thus, the non-linear recording of a hologram can not be avoided, but the effects can be diminished.

7.3 Resolution Limitations

Since the hologram itself is an integral part of the imaging system, the properties of the film plate should be considered in the design of the holographic system. Two ways in which the film plate can effect the reconstructed image resolution are its physical size and the film resolution. The preceding section developed the problems of a non-linear recording. Assuming, however, a perfect film and large optics, the size of the hologram then becomes the limiting parameter in determining speckle size and hence the sensitivity. That is to say that the f-number of the imaging system is dictated by the hologram dimensions. A square holographic plate 25mm on a side and an object distance of 300mm will produce an average speckle size of 44 square microns; increasing the film plate to 75mm on a side decreases the average speckle size to 5 square microns. If the holographic film plate is sufficiently large, then the spatial resolution of the film plate also plays a key role in accurately constructing a holographic image.

In the construction process, the film plate is placed at the intersection of the object beam and the reference beam thus recording the complex interference pattern as was demonstrated in section 3. Previously, it was assumed that the film had sufficient bandwidth to record the interference pattern, however silver halide film has a maximum cut-off above which the recording fidelity suffers. This is modeled as a simple reduction in the modulation depth of the recorded interference pattern. The object and reference wavefronts are represented again by a similar phasor notation. However, this development pays closer attention to the direction cosines, f_x, f_y and α that determine the interference pattern at the film plate:

$$R(x, y) = A_r \exp(-j2\pi\alpha y)$$

$$O(x, y) = A_o \exp(-j2\pi\{f_x x + f_y y\}).$$

Assuming that the total exposure remains in the linear regime, the mapping will remain linear regardless of the film's frequency response. The distribution of the exposure intensity will be:

$$I(x, y) = |O + R|^2$$

$$= A_o^2 + A_r^2 + 2A_r |A_o| \cos\{2\pi(f_x x + f_y - \alpha)y + \phi\}.$$

Including the frequency response of the film,

$$M(f_x, f_y) = M(f_x, f_y) \exp\{-j\Omega(f_x, f_y)\},$$

the effective exposure intensity will be

$$I(x, y) = A_o^2 + A_r^2 + 2A_r |A_o| M(f_x, f_y) \cos\{2\pi(f_x x + (f_y - \alpha)y) + \phi - \Omega(f_x, f_y - \alpha)\}.$$

For off axis-holograms, the modulation rate $f_y - \alpha$ of this interference pattern can be predicted knowing the relative angles of incidence and applying Bragg's law. The film's ability to record this complex pattern is dependent upon the frequency response of the film. The frequency response is determined by the grain size of the film; a smaller grain size results in a higher frequency response, analogous to a higher sampling rate. A film resolution of 1000 lines per millimeter can tolerate an angular separation of the object and reference waves of about 30 degrees. Beyond that limit, the film plate is unable to record a hologram and becomes the limiting element in the optical system. In such a case, the apparent physical size of the hologram is reduced thus making the speckle size larger than acceptable. For this reason, most holographic film plates have a spatial resolution of more than 1500 lines per millimeter. However, the inherent problem with a smaller grain size is the accompanying reduction in sensitivity. The smaller grain size reduces the likelihood that a sufficient quantity of incident photons will be present for a desired grain to form a latent image. This requires a more powerful light source so as not to relax the resolution capabilities.

In heterodyne holographic interferometry, an accurate recording of the object position is critical in determining relative out of plane displacements. The practicality in constructing an off-axis hologram requires that one use a recording media with sufficient bandwidth or resolution and also have adequate photosensitive properties to obtain a linear recording. Typical photographic film is sensitive enough, but lacks the necessary spatial resolution to obtain a high degree of phase accuracy. Special

high resolution silver-halide film plates, such as Kodak 649F or Agfa 10E56, are typically employed because of their large spatial bandwidth, but require the use of high powered laser illumination, particularly in high speed applications. This has been the case in attempting to image the displacements involved with acoustic wave propagation.

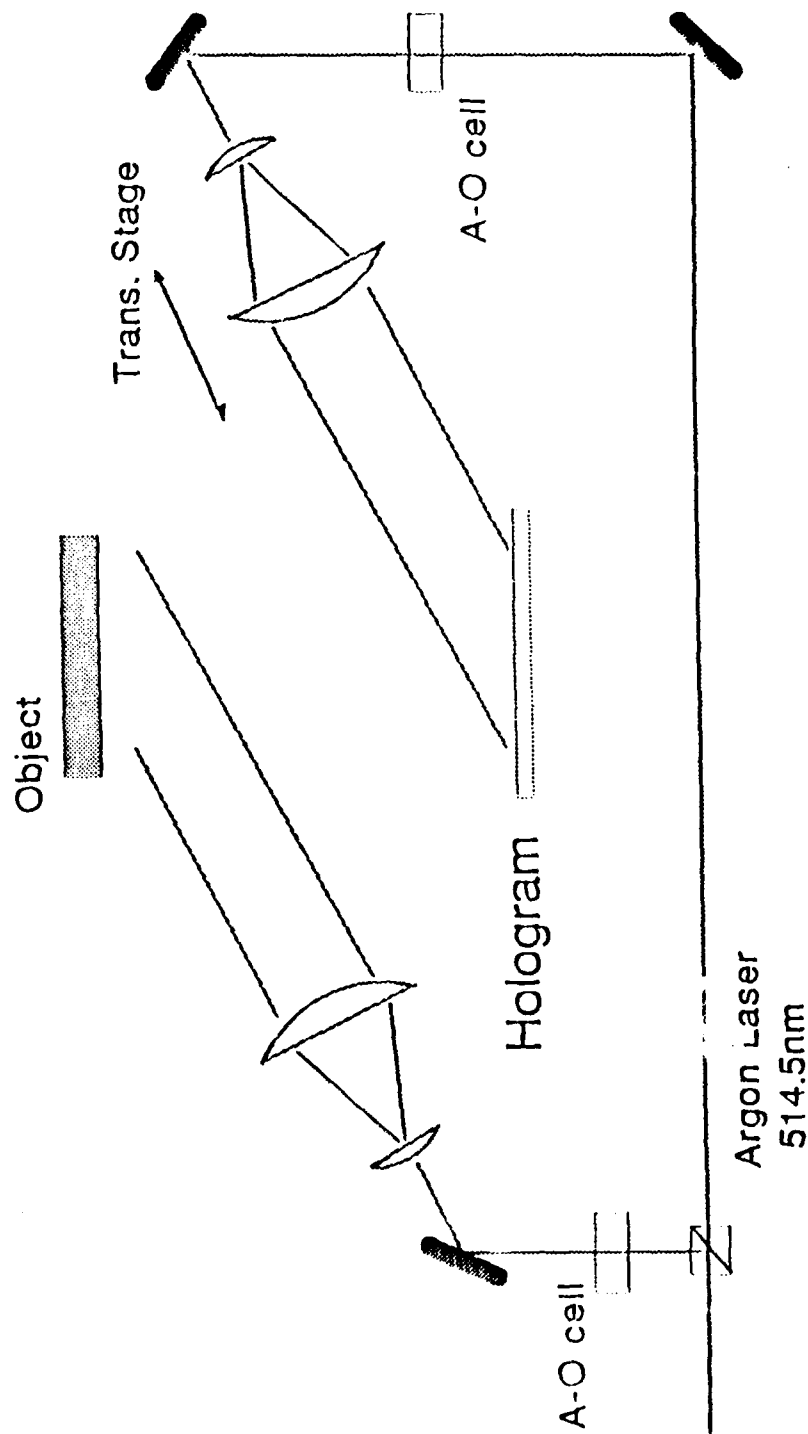
8 Experimental Design

The fundamental goal of this treatise was to successfully image sub-fringe acoustic waves in the full field using heterodyne holographic interferometry, and to demonstrate the ability to identify material defects by mapping acoustic waves. In achieving this end, the underlying resolution limits of heterodyne holographic interferometry came under close scrutiny. Five major experiments were performed to analyze various aspects of the question at hand. The first two experiments were the verified certain theoretical predictions and characterized the noise level in the static heterodyne read-out system. The first experiment addressed the most foreboding problem to overcome - the image decorrelation owing to the wavelength change introduced by the use of two different lasers for the construction and reconstruction process. To this end, wavefront curvatures owing to collimation deviations from the ideal were investigated. The second experiment involved constructing a working read-out system with a resolution design of less than 0.3nm. These static measurements provided the basis for constructing a stable heterodyne read-out system for the pulsed holograms. The third experiment researched the concept of using holography to image wave perturbations resulting from the interaction with a known defect, along with the application of imaging the wave speed anisotropy from a single measurement. The fourth experiment was performed to assist with the fifth; laser generation studies were conducted with a fiber optic interferometer. This lead to the successful completion of the fifth and final experiment, imaging of laser generated Lamb waves in a thin plate. These holograms were recorded with a Nd:YAG laser and then analyzed with a cw Argon laser employing a heterodyne read-out system.

8.1 Real Time Heterodyne Holographic Interferometry

The use of a real time holographic system was employed as a means of verifying the in-plane image translations associated with the misalignment of the collimating optics. The associated phase error resulting from a degradation in the collimating has not been well documented in the literature, and there appeared to be a need to substantiate the predictions made in section 10. The configuration shown in figure #8.1 was used to record a hologram of a rigidly mounted aluminum block measuring 10cm square. The surface was sufficiently diffuse to produce a fully developed speckle pattern. After processing the hologram, the real time object and the reconstructed image were superimposed and the collimating lens was translated in a co-linear fashion while monitoring the fringe contrast in the heterodyne read-out system. The objective was to verify the predicted image decorrelation resulting from improper collimation.

The hologram was recorded using a Spectra-Physics 165 argon ion laser. The light from the laser was split to form the object and reference waves, each passing through separate A-O cells (Fig #8.1). These A-O cells (Isomet 1202E) were driven by the same 40MHz driver (Isomet 221A) during the hologram construction. The hologram was recorded on 4"x5" glass film plate (Agfa 10E56), which was mounted in a liquid gate that permitted in-plane photographic processing. The film plate was exposed to a total energy of $15 \frac{\text{ergs}}{\text{cm}^2}$ with a reference to object beam ratio of 10:1. The development process was similar to any silver halide development process with a 5 min. development time in D-19 Kodak developer and a 5 min. fix time in Kodak rapid fixer. After adequate rinsing, the hologram was reconstructed and coherently interfered with the real time object. Modulating the resulting image intensity was accomplished by changing the drive frequency to the reference beam A-O cell. It



Real Time
Heterodyne Holographic Interferometry
Figure #8.1

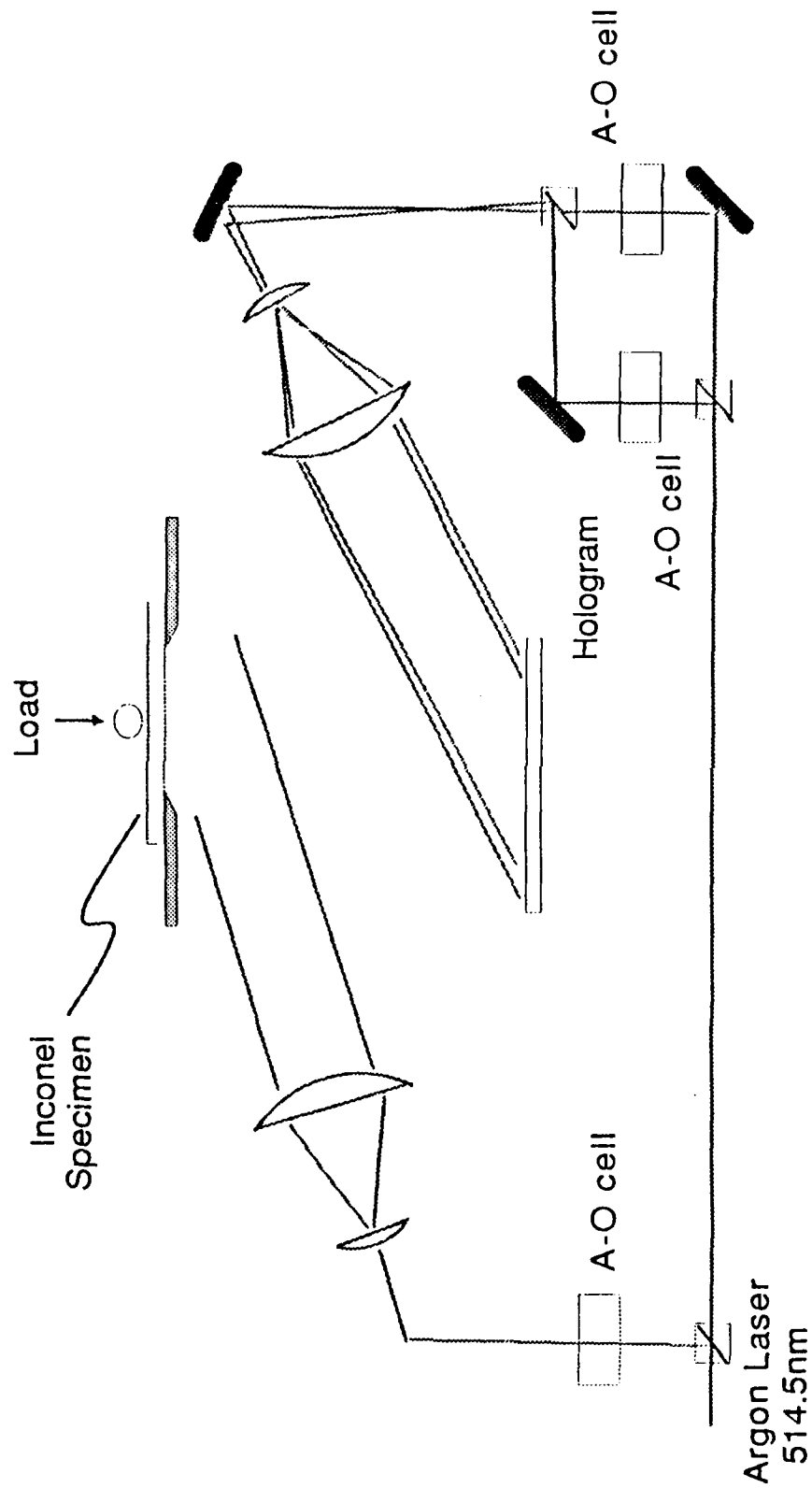
was driven with a crystal oscillator (International Crystal OT-124) at 40.1MHz and boost to the suitable power level with an RF power amplifier from TRW (CA2833). This introduced a modulation of the image intensity at a difference frequency of 100KHz, which was detected by a photomultiplier tube (EMI 9785B) in the image plane. The image was formed with a standard 35mm camera lense (Nikkor 105mm f/#2.5). The output of the PM tube was fed to the input of a lock-in amplifier along with a reference signal for comparison. This reference signal was derived by mixing the signals from the electronic A-O drivers and then running the output through a low pass filter. In this configuration, the lock-in (Ithaco 393-option 03) was used to measure the amplitude or depth of modulation of the interfering images. Monitoring the output signal gave an indication of the image registry as the degree of collimation was varied. Both the position of the collimating lense and the PM tube were mounted on Newport translation stages fitted with controlling actuators (850-1) and digital read-out of the position.

8.2 CW Double Exposure Heterodyne Holographic Interferometry

The purpose of this experiment was to construct a heterodyne holographic read-out system that was appropriate for reconstructing a hologram which had been constructed at a different wavelength. The system was designed to produce a phase error of less than 0.36° . In achieving this goal, a study was conducted on the feasibility of using heterodyne holographic interferometry to detect and size surface breaking cracks in 718 inconel alloy specimens. Test specimens 3"x4"x1/2" thick were subjected to a three point bending stress while a double exposure dual reference beam hologram was recorded. Between holographic exposures, the applied stress was increased by approximately 10% of the initial stress. The corresponding

surface displacements were then mapped through heterodyne analysis of the hologram.

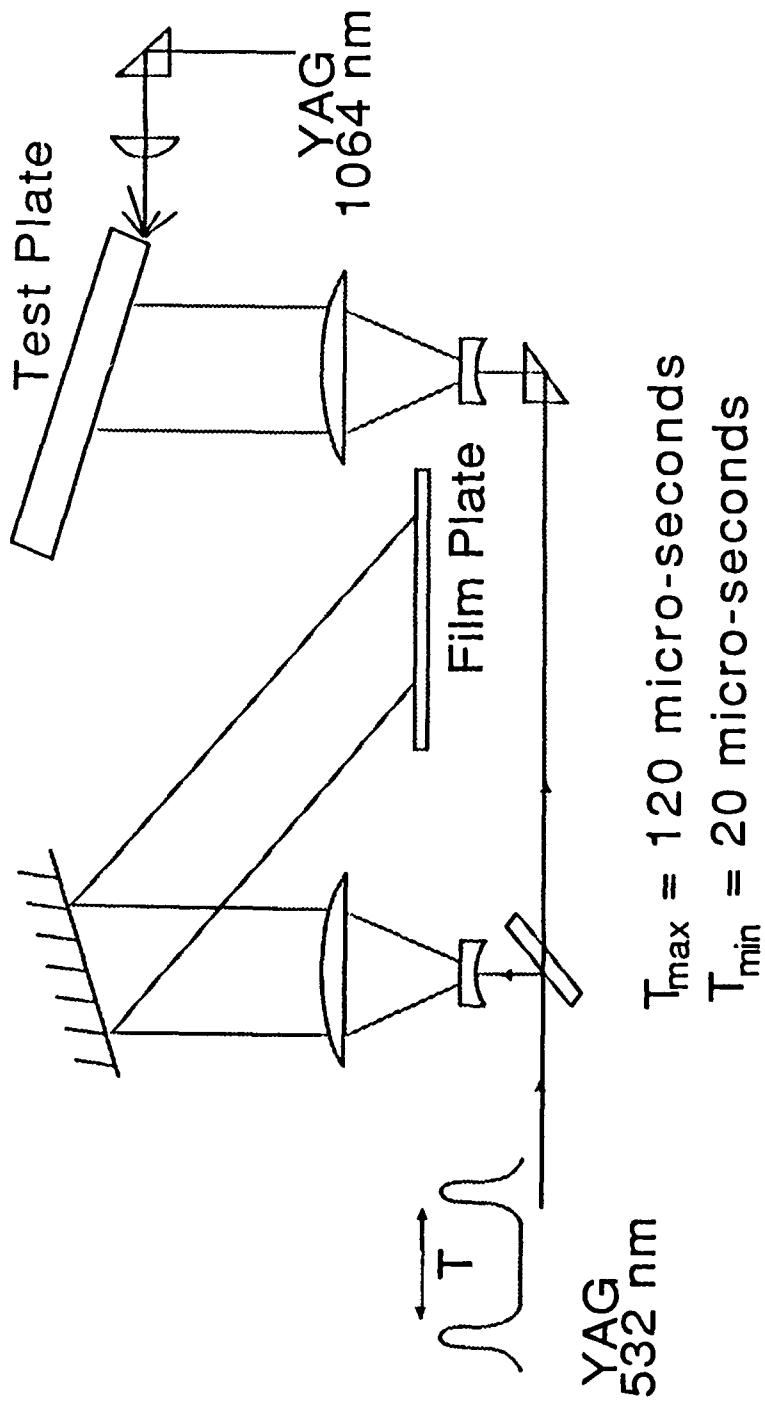
The double exposure hologram was constructed with a Coherent 53 argon ion laser with each of the stress states being recorded by a different reference beam (Fig. 8.2). A erasable thermoplastic film plate (Newport HC-320) was used in lieu of the silver halide film plates and exposed to a total energy of $100 \frac{\text{erg}}{\text{cm}^2}$. One will notice the use of a narrow reference beam angle, in figure #8.2, as an attempt to study the effects overlapping images in the reconstruction process. During the analysis phase, no object beam was used, but instead both reference beams illuminated the hologram simultaneously with a difference frequency of 100KHz corresponding to the A-O cells frequencies of 40MHz and 40.1MHz. A mirror chip was placed in the image plane to split off a portion of the image to a reference photo-detector. This signal was amplified (Tektronix AM502) and bandpass filtered to achieve a peak to peak voltage of 1 volt for the reference input of the lock-in amplifier. Using a portion of the image as the reference signal helped to compensate for atmospheric disturbances such as turbulence and temperature changes. The relative phase difference between the reference signal and the scanning signal was measured with the lock-in. The input signals were obtained for each point in the image plane by scanning a detector over the two interfering images. Scanning was performed using two computer driven electronic micrometers. Computer control of the scanning operation was performed with the Newport controller (855C) and a AT&T 6300 PC with the Metrabyte GPIB interface. Data acquisition was also obtained over GPIB interface using the A/D capabilities of the HP 3478A multimeter connected to the analog phase output from the lock-in amplifier. The scanning programs were written in IBM Fortran and are included as an Appendix.



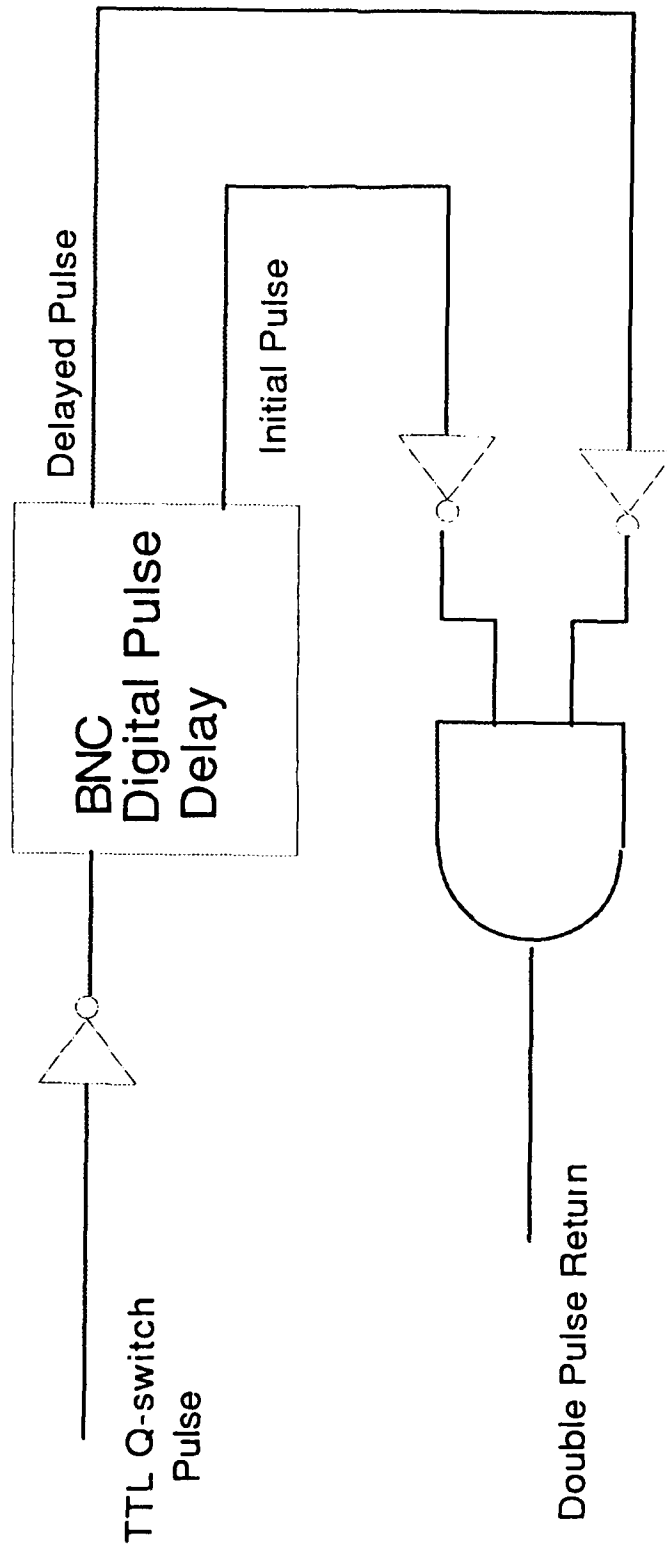
Double Exposure CW
Heterodyne Holographic Interferometry
Figure #8.2

8.3 Double Exposure Pulsed Holographic Interferometry

The purpose of this experiment was to record, in full field, the surface perturbations resulting from the interaction of a surface acoustic wave with a surface defect using a double-pulsed holographic recording system (Fig. #8.3). A Quantel Nd:YAG (580-C) laser with 9ns pulse-width and 500mJ per pulse at 532nm was used to construct the hologram for this high speed application. Double pulsing the laser was accomplished by external modification of the resident logic board in the laser; the resident q-switch logic pulse was redirected to a digital delay generator (BNC 7010) and recombined with the original pulse to provide a simple modification of the pulse control (Fig. #8.4). The first laser pulse recorded the resting position of the object with the 532nm output, as well initiating the acoustic wave generation with a separate 1064nm output port. The 1064nm line was used to detonate a small explosive charge of silver acetylide measuring approximately 2mm x 2mm x 0.5mm. This acoustic source was large enough to produce displacement amplitudes greater than $0.25\mu m$. The delayed second pulse, 40 μs later, captured the surface acoustic wave propagating across the plate. The specimen used was an aluminum plate measuring 25cm x 38 cm x 3.8cm thick with a half-penny defect 1mm wide, 25mm long and 2.5mm deep in the front surface of the plate 12cm from the edge. Since no heterodyne analysis was to be done, the experiment was designed to produce an out-of-plane displacement amplitude of the waves greater than $\frac{\lambda}{2}$ or $0.25\mu m$.



Double Pulsed Single Reference Beam
Holographic Interferometry
Figure #8.3

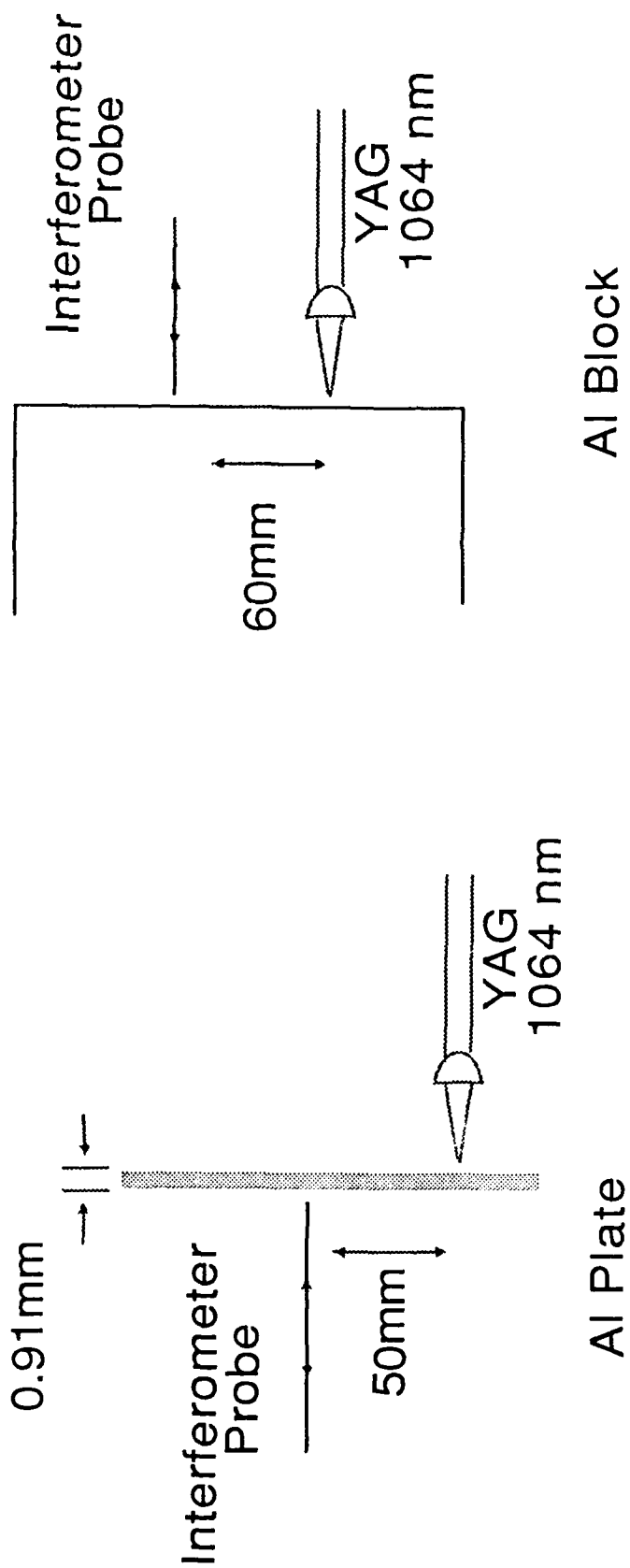


Double Pulse Circuit Diagram
for the Quantel Nd:YAG Laser
Figure #8.4

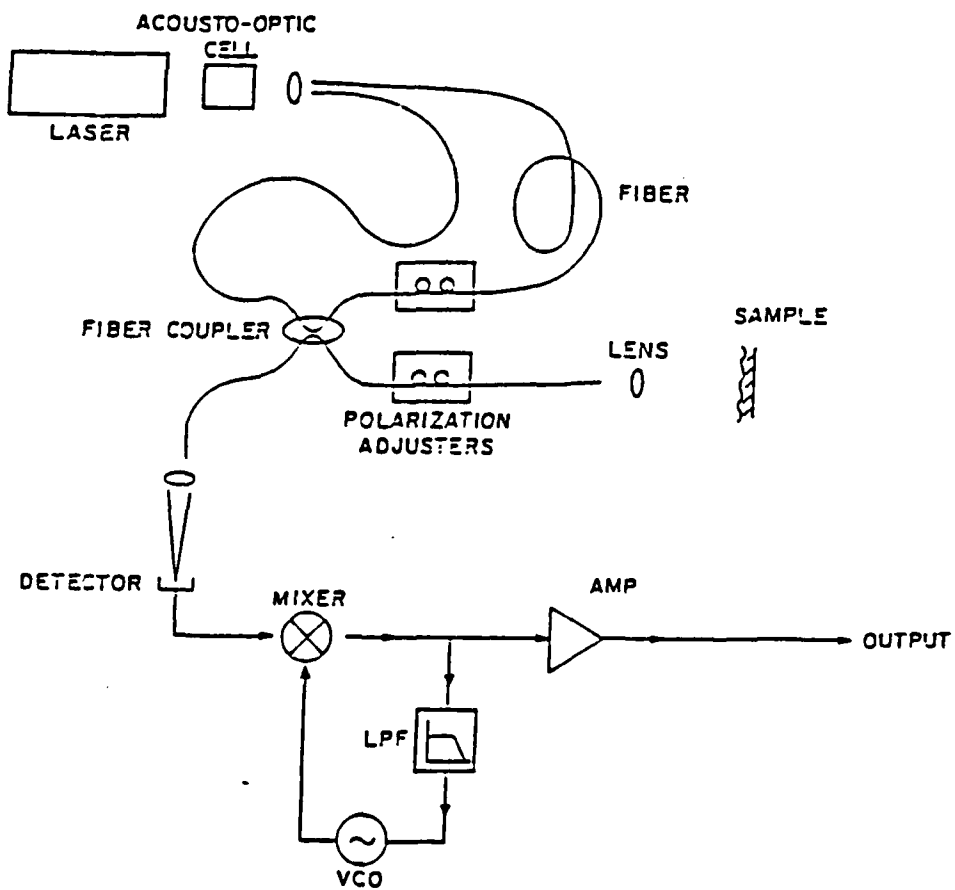
8.4 Interferometric Detection of a Laser Generated Ultrasound

The two types of laser generated acoustic waves thought to be applicable for holographic imaging were Rayleigh waves and Lamb waves. These waves have been shown by researchers to have largest out-of-plane displacement amplitudes for any type of laser wave so were deemed the most likely to be successfully detected with heterodyne holographic interferometry. This portion of the study used a fiber optic interferometer to measure the arrival of the laser generated waves in order to best estimate the timing of the double pulsed holograms. The specimen for the Rayleigh wave study was a 30.5cm x 25.4cm x 20.3cm thick block of aluminum, while the plate for the Lamb wave study was 200mm x 200mm x 0.91mm thick. Both were polished to a mirror finish to obtain a specular reflection for the laser interferometer. The acoustic wave was generated with the 1024nm line from the Quantel Nd:YAG laser. The beam was focused with a cylindrical lens to form an acoustic line source to limit the energy spread as the wave propagated. For maximum generation efficiency a drop of peanut oil was used as a constraining layer in all the studies. The probe beam for the interferometer was situated 50mm away from the laser source and normal to the line source (Fig #8.5). A LeCroy transient recorder with PC interface was used to collect the data. The fiber optic interferometer used in the detection of the laser generated waves was designed and constructed by James B. Spicer, who graciously loaned the instrument for these studies. A diagram of the instrument is shown in figure #8.6.

A unique feature of this fiber optic interferometer is that it only requires a single input coupler between the laser and the fiber thus improving alignment stability and reducing losses. Both the diffracted and undiffracted beams which exit the A-O cell are focused into the appropriate fibers. The directional coupler acts as a



Configuration for Laser Generation Studies
Figure #8.5



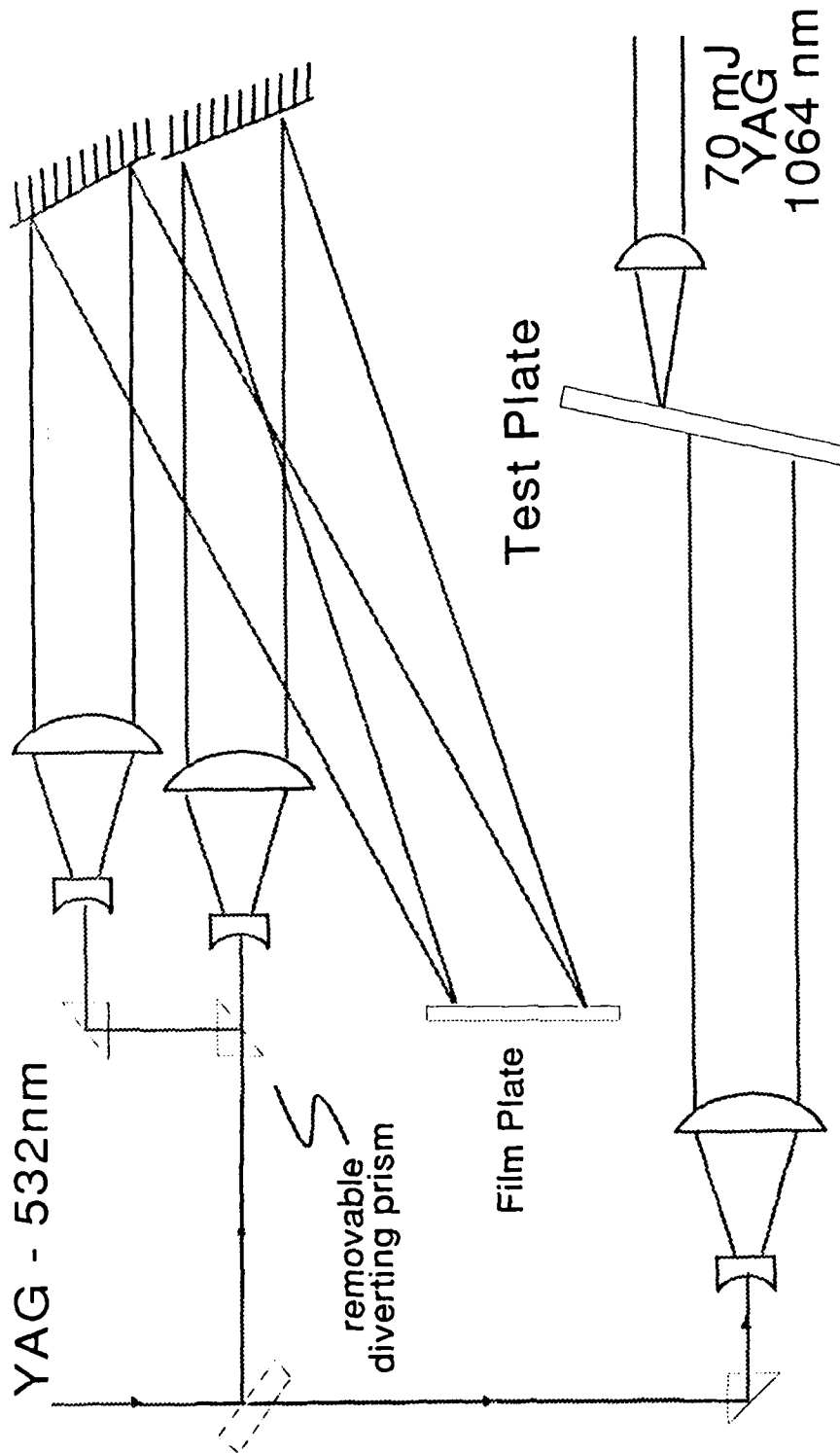
Schematic of the fiber optic interferometer.

Figure #8.6

beam splitter determining both the reference path and the probing path for the interferometer. In the absence of motion, the intensity incident of the photo-detector was modulated at the 40MHz difference frequency. A perturbation of the sample introduced a phase modulated signal at the detector. The detection electronics used a phase locked loop to demodulate and obtain the signal of interest. A 10MHz low pass filter at the output of the double balanced mixer eliminated the frequency doubled carrier and established the upper limit of the detection capabilities.

8.5 Full Field Imaging of a Laser Generated Lamb Wave

The major goal behind this treatise has been the application of heterodyne holographic interferometry to the mapping acoustic wave propagation in the full field. Normal acoustic sources produce sub-fringe displacements, which require the use a heterodyne read-out system for holographic detection purposes. The optics used were similar to the design used in the prior sub-section on double pulsed holography. However, for the purpose of employing a heterodyne read-out system, a second reference beam was added (Fig. #8.7). Separate reference beams were used to record the different positional states of the object, and each reference beam was collimated using a shearing interferometer. Special Fourier transform lenses (SORL 2324) were used to collimate. The delay between the two pulses was $25\mu s$ which was controlled in the same manner as before. The film plate (Agfa 10E56) was exposed to a total energy of about $1.0 \frac{mJ}{cm^2}$ with a reference to object beam ratio of greater than 50:1. The film processing in this experiment included a bleaching step after the silver halide plate had been fixed. The bleaching stage transformed the adsorption hologram into a phase hologram which produced a higher diffraction



Triple Exposure Technique
Heterodyne Holographic Interferometry
Figure #8.7

efficiency. This was achieved by rehalogenating the film by submersing the film plate in a saturated chlorine solution. In a short period of time, the film plate would change from a dark gray to a cloudy white appearance. The bleaching time was dependent upon the relative exposure and was twice the amount of time needed for the plate to clear, usually 20-30 seconds. This technique improved the reconstructed image intensity four to five-fold.

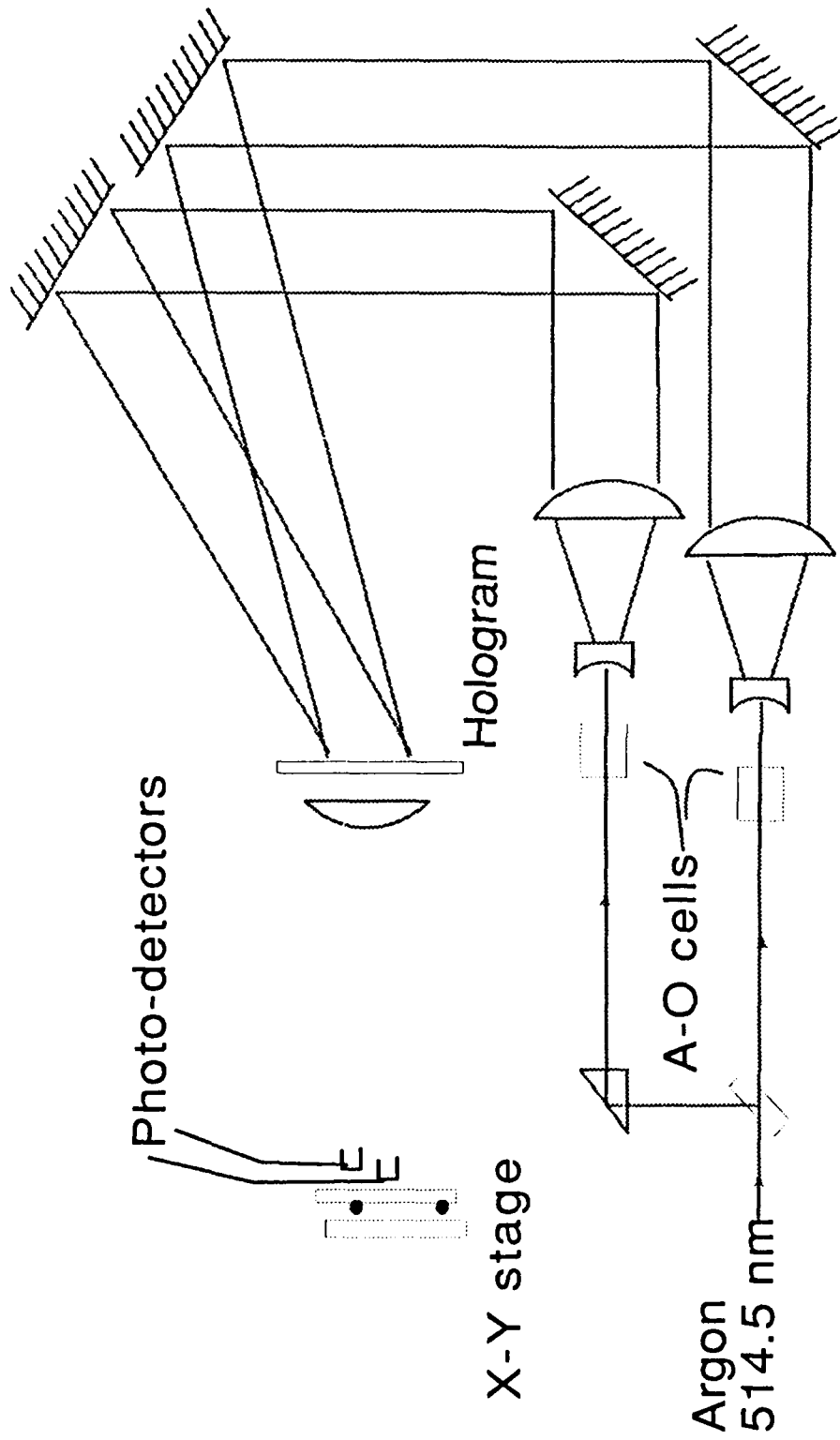
Splitting the pulses along the appropriate reference path would ideally employ an electro-optic switch, however, since no switch was available, a removable diverting prism was simply physically changed between exposures. In doing so a triple exposure hologram was created (as opposed to a double exposure) creating some additional problems. The process called for the laser to remain in the double pulse mode continually. The first exposure was simply the unperturbed object. The prism was then removed and the laser was double pulsed. The first pulse initiated the propagating acoustic wave and a second exposure of the object at rest. The second pulse followed $25\mu s$ later having allowed the acoustic wave to propagate the predicted distance and creating a third image on the hologram, the one of interest. The problem arises since the first pulse of the second reference wave had in actuality recorded a double exposure hologram of the unperturbed object capable of causing unwanted interference fringe artifact. If the displacements were of sufficient amplitude then the resulting fringe pattern would overlap the modulated image reducing the signal to noise ratio in the read-out system. A far more serious effect, however, is the relative intensities of the second and third object exposures on the phase measurement. Wagner has previously investigated this problem and found the measured phase to be a function of the reconstructed object amplitudes O_2 , O_3 and the relative path length difference $\Delta\phi$ (Eq. #8.1):

$$\theta = \tan^{-1} \frac{O_3 \sin \Delta \phi}{O_2 + O_3 \cos \Delta \phi} \quad (8.1)$$

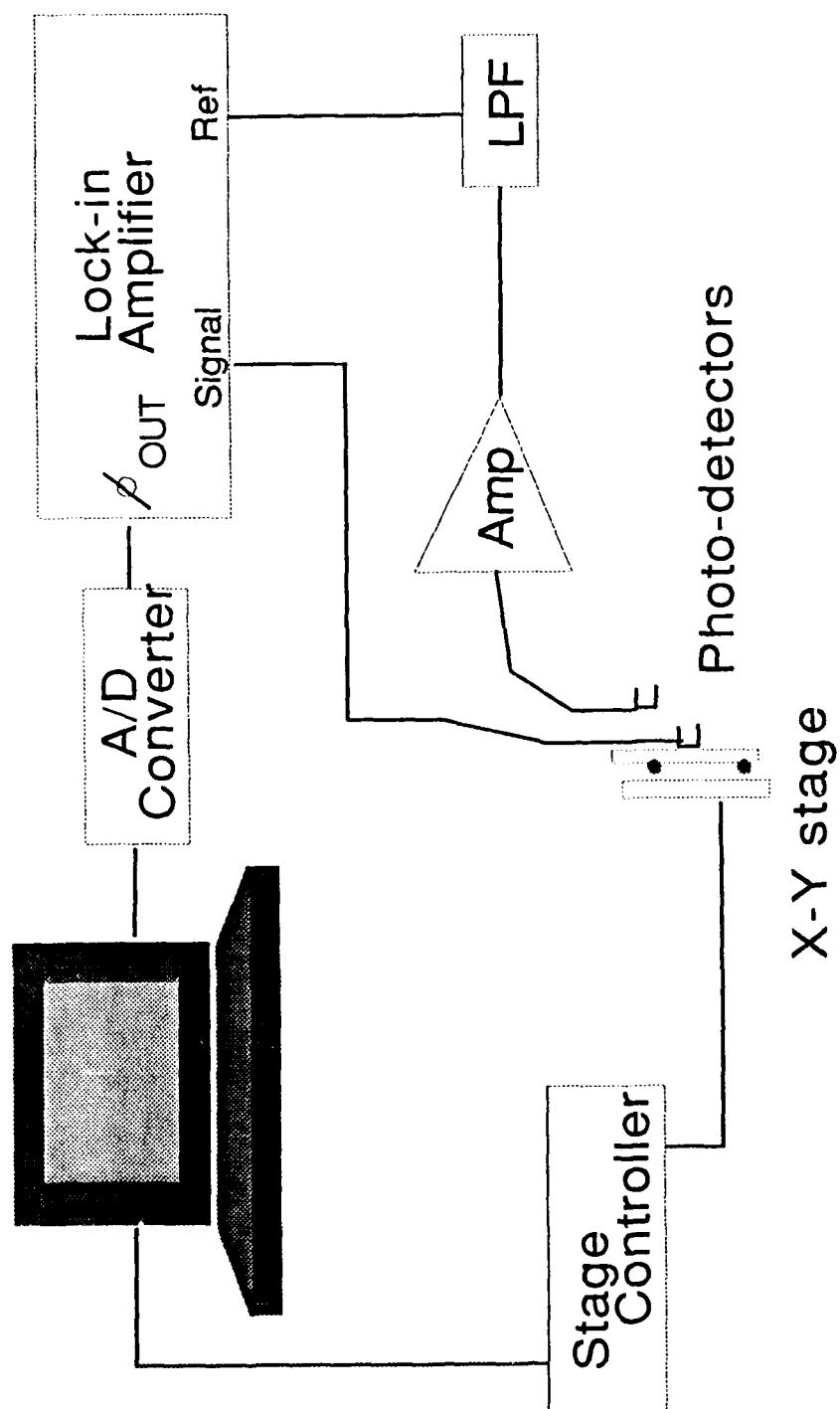
The saving grace for this technique occurs when $O_2 = O_3$, making the measured phase difference one half the actual value and thus a linear transformation. Therefore, although the phase sensitivity has been reduced to $\frac{\lambda}{1000}$, this still provides adequate resolution for imaging acoustic waves.

The optical configuration used in performing the heterodyne analysis is shown in figure #8.8. The two reference beams were again collimated with a shearing interferometer. Precise adjustments were made later with the hologram in position with one of the collimating lenses mounted on a micrometer stage with an electronic micrometer controlling the position (Newport 850-1). The angular alignment was adjusted by rotating the hologram and the horizontal translation of the reconstruction mirrors. This system was very similar to the one described for cw analysis with the only exception being the wide separation of the reference beams, approximately 8° in the construction stage. This corresponded to an angular change between the reference beams of about 0.33° . The phase detection electronics for the heterodyne read-out, employing an A-O cell in each reference beam, was the same as used previously in the cw configuration and is diagramed in figure #8.9. The entire optical system was contained in an baffled box in order to reduce air turbulence.

The quasi-heterodyne system employed the same optical system as did the heterodyne analysis system with only the substitution of the necessary electronics. Quasi-heterodyne holographic interferometry is based on calculating the phase difference for a series of intensity measurements taken at known incremental phase positions of the interference pattern (Eq. #3.21). The relative phase steps between



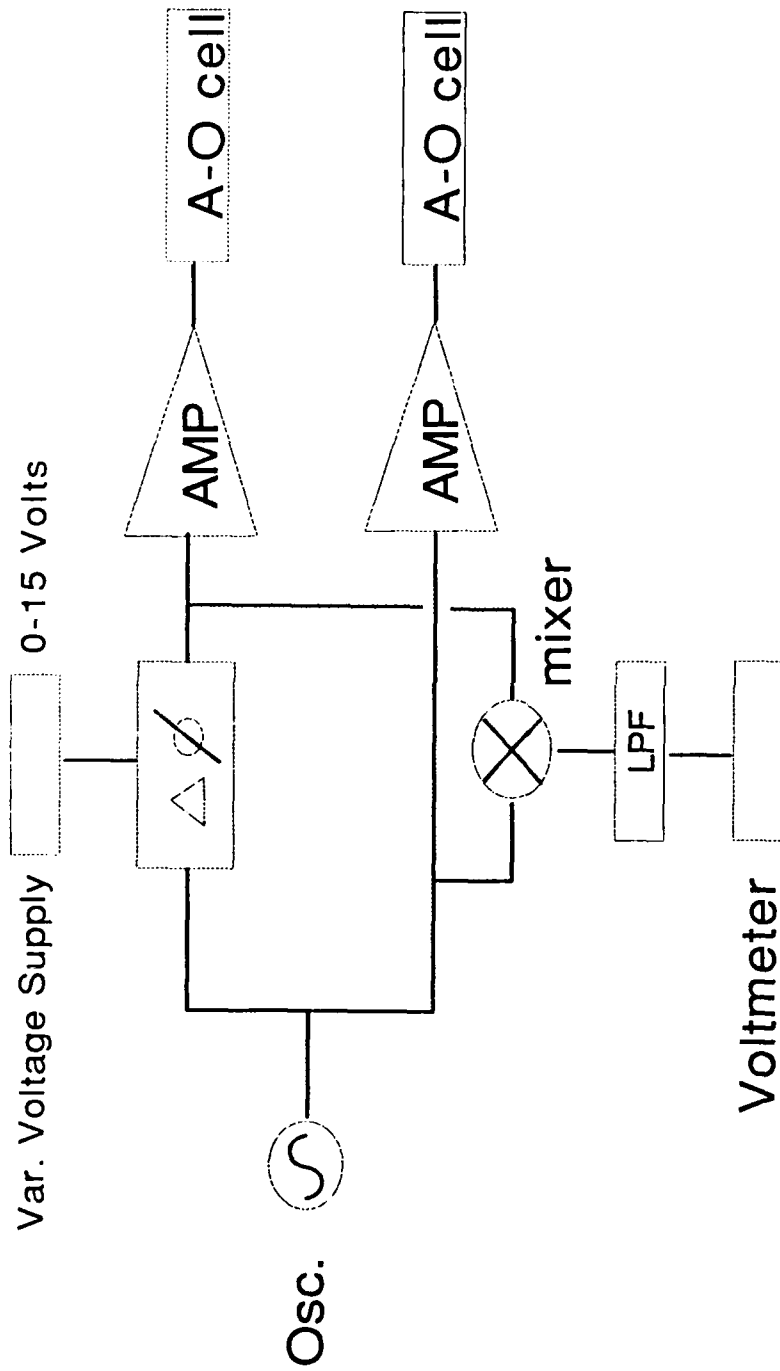
Heterodyne Readout System
Figure #8.8



Electronic Configuration for Heterodyne Analysis

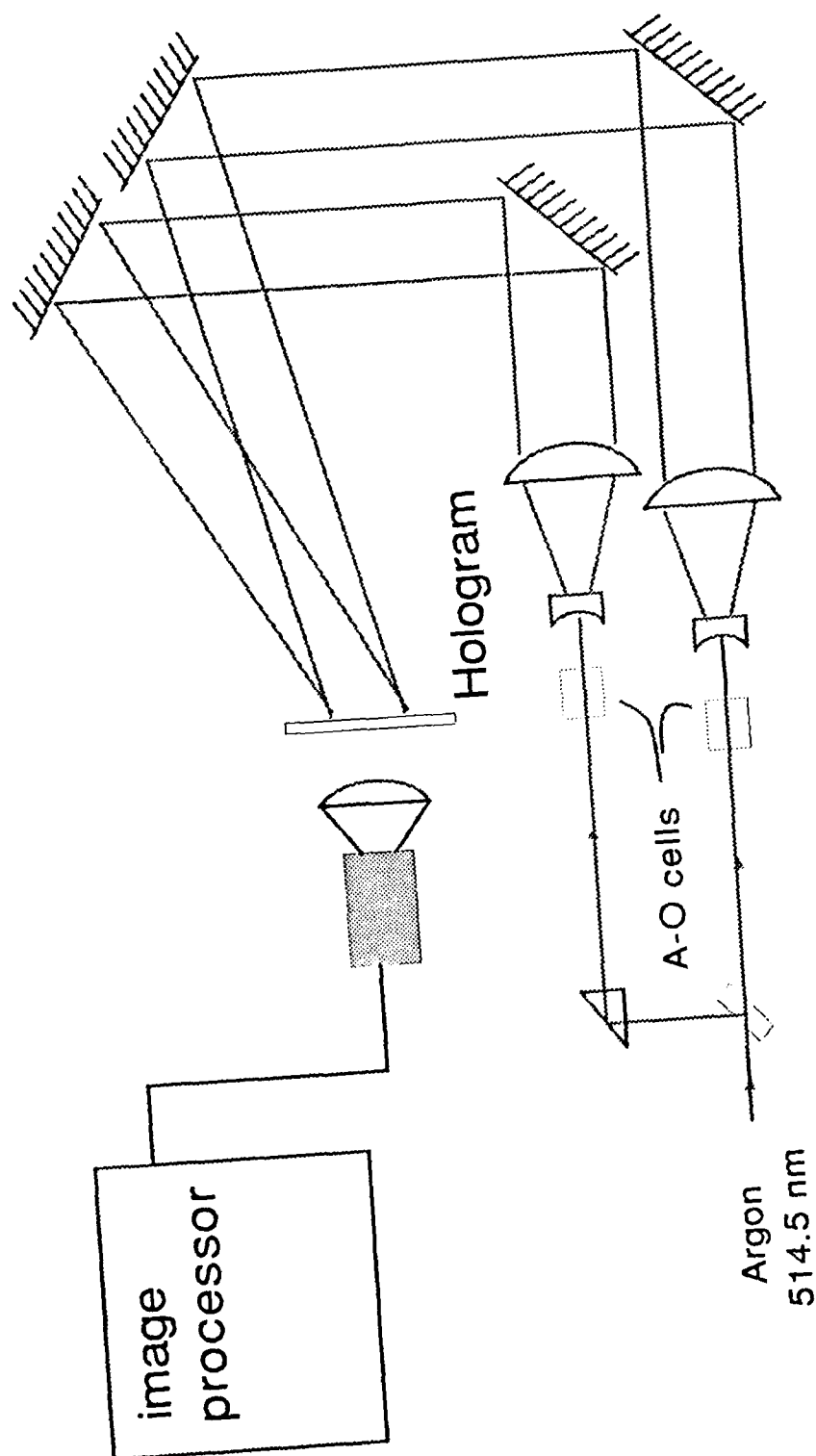
Figure #8.9

the two reference beams were created by driving the two A-O cells at the same frequency while imposing a phase delay between the two drive signals. The A-O drive signals of 29.3 MHz were derived from the same crystal oscillator (International crystal OT-124) with one path being phase delayed by a voltage controlled phase shifter (Merrimac 12457). RF power amplifiers from TRW (CA2833) were used to boost the 29.3MHz signal to drive the A-O cells. The relative phase delay was measured by mixing the two signals, lowpass filtering, and then measuring the output (Fig. #8.10). The output of the lowpass filter was directly related to the cosine of the phase delay, $\cos \theta_i$ and for $0^\circ, 90^\circ, 180^\circ$ phase steps the voltmeter measured $V_{\max}, -V_{\max}, V = 0$. The intensity data was acquired with a Fairchild CCD camera at these three increments. The pixels of the camera were $12\mu m \times 18\mu m$ with an $18\mu m$ dead zone between pixels and the array measured 180×162 . The frame grabbing capabilities of the image processor (Vicom 1850) captured the data and performed the subsequent processing to determine the actual phase difference (Fig. #8.11).



Quasi-heterodyne Phase Shifting Circuit

Figure #8.10



Quasi-Heterodyne Read-out of
the Triple Exposure Hologram
Figure #8.11

9 Experimental Results

9.1 Real Time Heterodyne Holographic Interferometry

The real time heterodyne holographic system was constructed for the purpose of investigating the effects of collimation deviation on the image registry. The development in section 5 showed that a change in the collimation optics could cause a detrimental image magnification and hence a reduction in the phase sensitivity. In this experiment before the hologram was constructed the reference beam was repeatedly collimated using a shearing interferometer. An electronic micrometer driven translation stage was used to measure the resulting positional error. The micrometer was reported by the manufacturer to have a positional accuracy of $0.1 \mu m$; the reported flatness of the shearing interferometer was $\frac{\lambda}{10}$. The standard deviation for the position of the collimating lens was found to be 20 microns, which corresponds to a beam radius of 6000m. The lens was positioned at the mean and the hologram was constructed.

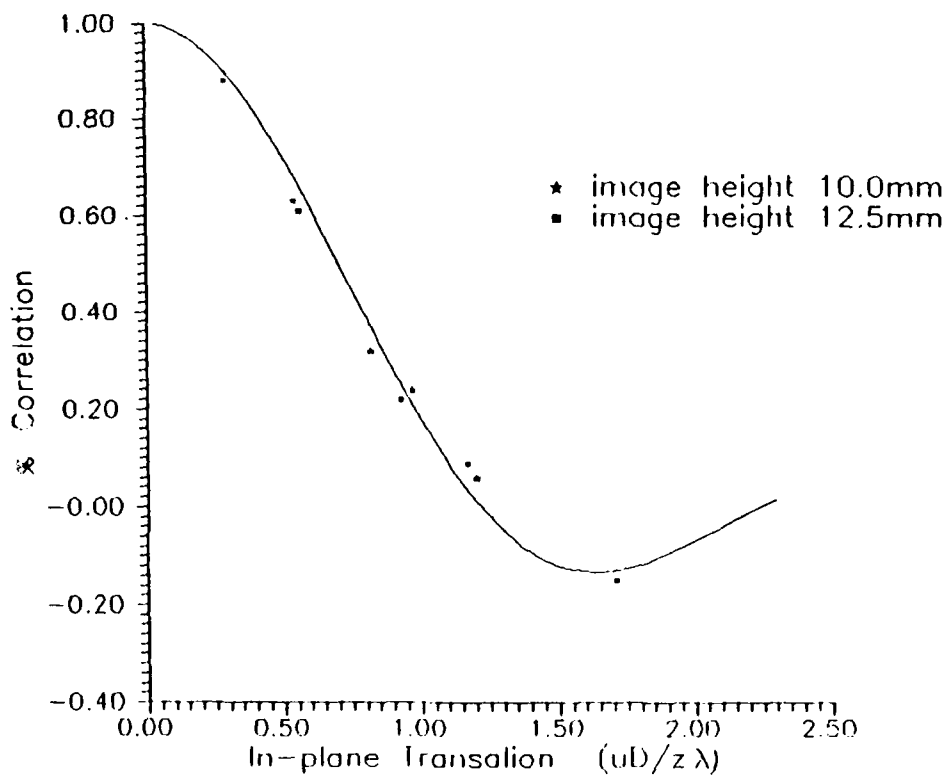
After the hologram was developed, the two interfered images were modulated at 100KHz, the frequency difference between the two A-O cells. A photo-detector positioned in the center of the image monitored the modulation depth of the fringe contrast as minor optical misalignments were corrected. The image translation was predicted to be a function of the lateral extent of the object and of the reconstruction wavefront curvature. The photo-detector was positioned at observation points 10.0mm and 12.5mm away from the central position. The depth of modulation was monitored as the collimation lens was translated, which induced a magnification of the reconstructed image. Wavefront curvature was estimated by measuring the relative change in position of the collimating lens. Based on this measurement, and

using Eq. #5.7 and #5.13, an estimate of the in-plane image translation was obtained relative to the lateral object extent which is graphically compared to the measured correlation values (Fig. #9.1). As demonstrated by figure #9.1, the data showed good agreement with the theoretical predictions of percent correlation versus in-plane image translation. This information was paramount in determining the amount of object area over which one could expect to have sufficient correlation in order to perform heterodyne analysis.

9.2 CW Double Exposure Heterodyne Holographic Interferometry

The cw heterodyne study was conducted to help determine the ability to size small displacement perturbations and to characterize the heterodyne analysis read-out system. The inconel test specimens were provided by General Electric Corporation with fatigue cracks ranging in size from 0.41mm to 6.25mm in length. The test specimens were subjected to three point bending stress while double exposure, dual reference beam holograms were recorded. The object beam illuminated the specimen from such an angle so that the in-plane displacements were accentuated in the experiment. A step increase of 1500lbs (a 10% increase in the initial force) was applied between exposures. The underlying principle making this a useful technique for heterodyne analysis was that the cracked region would have a larger displacement field associated with it than the uncracked portion.

To analyze the spatial resolution of the scanning system, an experiment was performed to determine the location and size of previously characterized fatigue cracks holographically. The scanning system covered an area of 1cm x 1cm in 0.5mm increments. The diameter of the scanning detector was 0.5mm. The output from the lock-in amplifier was the relative phase difference between the reference

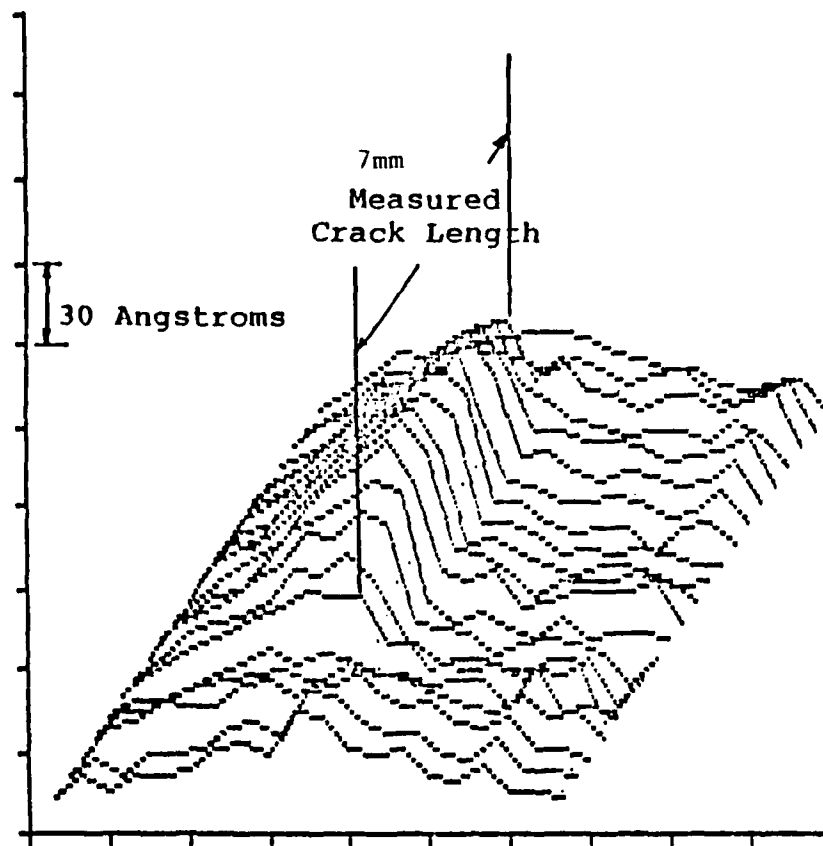


Percent image correlation vs. the in-plane image translation owing to the collimation error.

FIGURE #9.1

detector and the scanning detector. This detected output was found to have a large biased slope owing to the gross body motion involved with the applied load. Processing the data required that this slope be subtracted out in order to reveal the subtle changes near the cracked regions. In figure #9.2, the surface displacements are displayed; the abrupt discontinuity near the crack region was measured to be 7.0mm. The specified crack length of 6.25mm compared favorably. The next largest crack of 1.27mm was not detected with heterodyne analysis nor with an eddy current probe. The position of this crack was reported by GE corp. as was the size. Neither this, nor any smaller cracks could be detect with either Heterodyne analysis or eddy current methods.

Characterization of the heterodyne analysis read-out system was performed by scanning a reconstructed image of two stationary object states. Subsequent noise analysis for the heterodyne system was of interest towards the goal of building a detection system for imaging acoustic waves. The temporal phase error was found to be better than 0.2° . The resulting spatial phase error was measured to be 1.0° . This value was higher than desirable for the imaging of acoustic waves and certain system modifications were necessary. The first improvement was a larger separation of the reference beams which removed the overlapping image condition. This decreased the phase error by one half. The second obvious improvement was to increase the optical resolution for the system. The film plate for the system was only 25mm x 25mm - the use of a larger aperture decreased the speckle size and improved the sensitivity of the system by an order of magnitude.



Heterodyne analysis of a 1cm x 1cm
area around the fatigue crack

Figure #9.2

9.3 Double Exposure Pulsed Holographic Interferometry

The purpose of the experiment was to record, in full field, the surface perturbations resulting from the interaction of a surface acoustic wave with a surface defect using double-pulsed holography. The photograph of the reconstructed image displayed in figure #9.3 shows an acoustic wavefront as it appeared $40\mu s$ after an explosive charge was detonated. An explosive charge was necessary to achieve the needed displacement amplitudes on the order of a wavelength of light. The fringes in the photograph correspond to displacements greater than $\frac{\lambda}{2}$. An unfortunate aspect of this technique is that the direction of motion is ambiguous without any type of heterodyne analysis. However, one can observe from the interferogram that the leading wavefront was delayed as it propagated through the slotted region as evidenced by the change of curvature of the wavefront. Also, there is a strong reflected component traveling in the opposite direction. Although a large amplitude wave was used, the successful results of this experiment lead one to expect similar results for low amplitude waves when applying heterodyne analysis.

9.4 Interferometric Detection of Laser Generated Ultrasound

A fiber-optic interferometer was used to detect laser generated ultrasound. This study served to estimate the timing for the pulsed hologram as well as measure the amplitude displacements. The use of laser generated ultrasound as an acoustic source was restricted to investigating Rayleigh waves and Lamb waves. These wave types have been reported to have out-of-plane displacements large than bulk acoustic waves and therefore are more likely to be detected with heterodyne holographic interferometry. As described in the experimental section, the interferometer probe



Double pulsed interferogram of a surface
acoustic wave interacting with a slotted defect

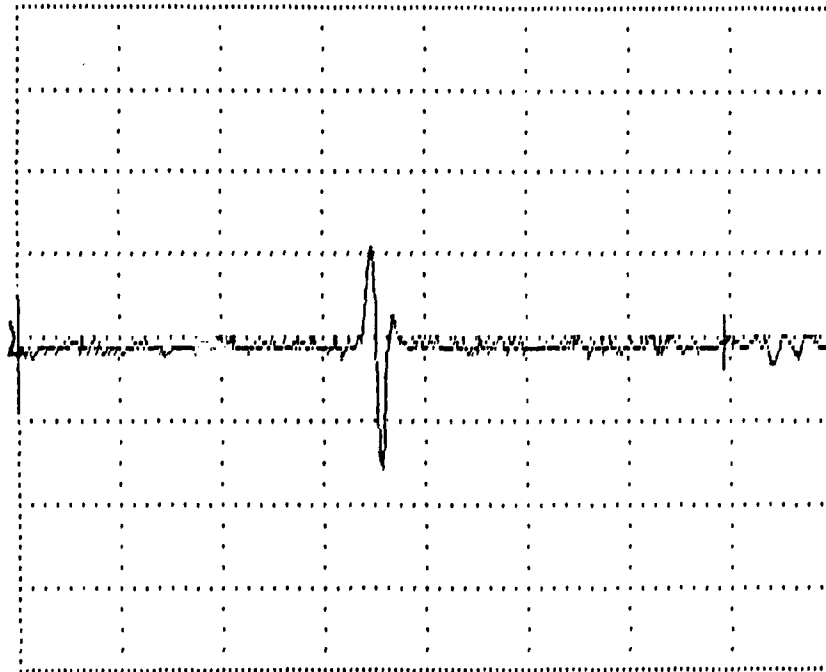
Figure #9.3

beam was positioned 50mm downstream from the laser line source. A calibration scale for the interferometer was obtained by applying a relative large rapid force (a "thwack") which permitted the determination of the maximum excursions of the interferometer output. The peak-to-peak output voltage corresponded to a 360° phase change or a $\frac{\lambda}{2}$ displacement. Data for the Rayleigh pulse was taken for incident energies of 40mJ and 125mJ, while the Lamb wave data corresponds to 40mJ and 70mJ (Fig. #9.4a&b, #9.5a&b). An incident energy of 12 mJ was attempted in the Lamb mode case, but did not produce any displacements large enough to exceed the noise level of the interferometer. The other two energy levels for the Lamb wave specimen of 40mJ and 70mJ produced amplitudes that differed by almost a factor of 2. The Rayleigh wave pulses produced had no amplitude gain for an increase in incident energy. For all the waves recorded, ablation of the surface was observed. The rapid rise time for the Rayleigh pulses, in some cases 100ns, made it an unlikely candidate to be imaged by heterodyne holographic interferometry. Although it had sufficient amplitude, the spatial width of 0.3mm would have been difficult to detect. The Lamb data appeared to have sufficient amplitude and spatial widths ranging from 5mm to 10mm, and was therefore deemed to be the best candidate for heterodyne holographic detection.

9.5 Full Field Imaging of a Laser Generated Lamb Wave

The following analysis demonstrates that heterodyne holographic interferometry may be used to image sub-fringe displacements associated with high speed events. The optical configuration described in the previous experimental design section used two well separated reference beams in constructing the hologram. This insured that the 50mm x 40mm illuminated area of the object would not have any

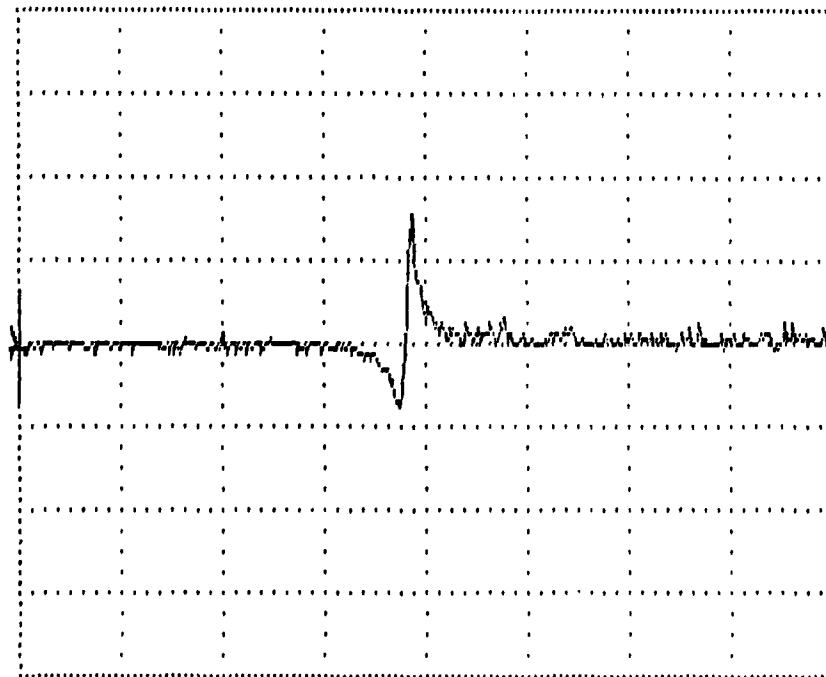
FIGURE #9.4a

 $28 \frac{\text{nm}}{\text{div}}$ 

Rayleigh wave spike, incident energy
40 mJ.

 $1 \frac{\text{u sec}}{\text{div}}$

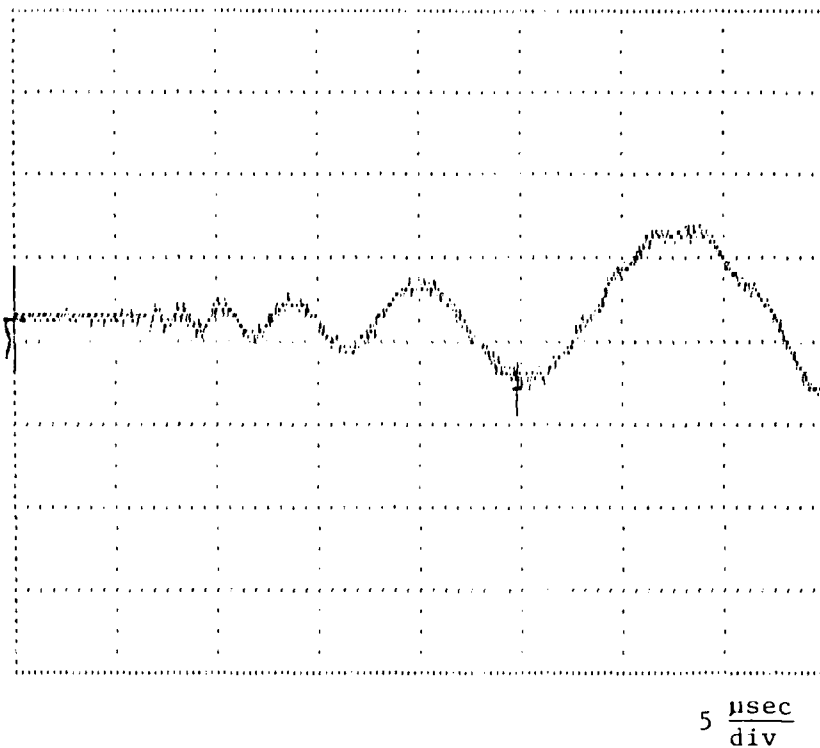
FIGURE #9.4b

 $28 \frac{\text{nm}}{\text{div}}$ 

Rayleigh wave spike, incident energy
125 mJ.

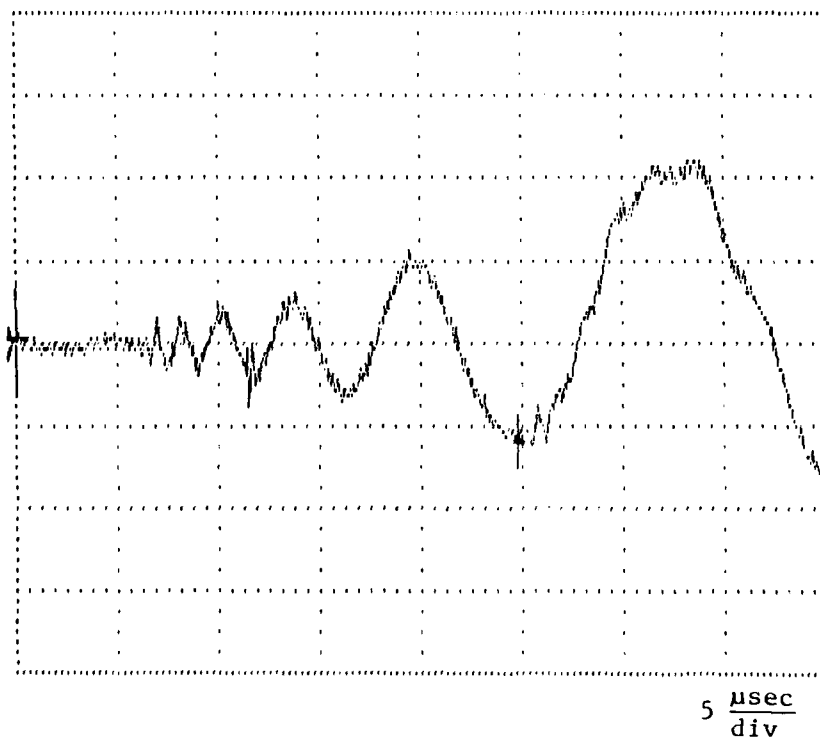
 $1 \frac{\text{u sec}}{\text{div}}$

FIGURE #9.5a

56 $\frac{\text{nm}}{\text{div}}$ 

Lamb wave generated from a laser pulse,
9 msec, incident energy 40 mJ.

FIGURE #9.5b

56 $\frac{\text{nm}}{\text{div}}$ 

Lamb wave generated from a laser pulse,
incident energy 70 mJ.

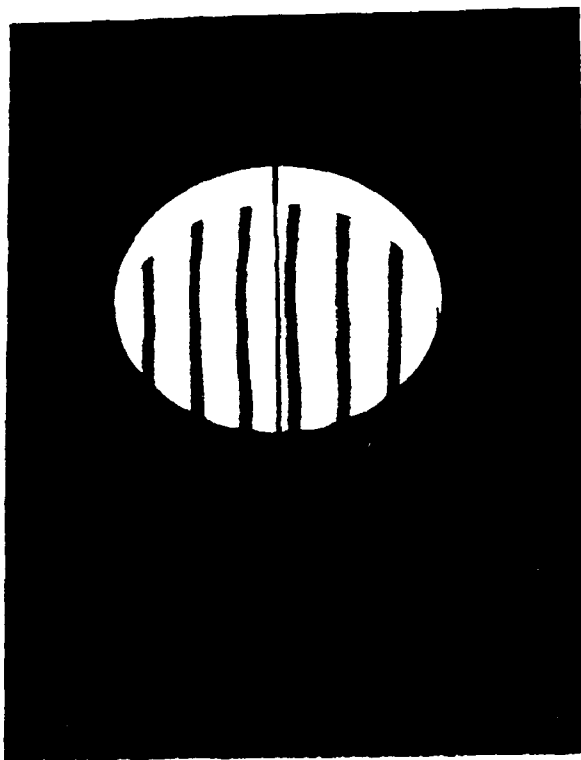
overlapping images. The imaging system employed had a f-number of 5 and produced a reduced image half the original size. The diameter of the photo-detector was 0.75mm, giving an effective diameter on the object coordinates of 1.5mm. Unfortunately, the speckle size remains the same independent of magnification changes, so the 0.75mm dimension of the photo-detector was used in the theoretical calculations.

The experimental determination of the system phase error was performed with a stationary object for determining the spatial noise. The temporal stability was found to be extremely sensitive to minor room temperature fluctuations. An equilibrium condition was usually reached around sunset for approximately a 2 hour period. It was assumed that the same condition existed at sunrise, but it was never tested. During the stable periods in the evenings, the temporal phase error was found to be less than 0.2° . The spatial phase error, however, was found to vary depending upon the manner in which the object was scanned. A square scan of 6x6 independent points produced a local phase error of 0.26° , while a linear scan produced a spatial phase error of 0.9° . The linear scan also appeared to have an inherent curvature. The wavefront from the Nd:YAG laser is observed to have a non-uniform phase front and this was felt to be the contributing factor in the effective image curvature. This is demonstrated in figure #9.6b. A perfectly collimated wavefront would produce perfectly horizontal fringes (Fig. #9.6a). However, since the phase error on a local basis could be predicted, it was felt that the wavefront variation would not be too detrimental.

After proper alignment of the hologram, a 20mm x 16mm area was scanned with a horizontal increment of 0.4mm and a vertical increment of 0.8mm. This produced 1071 data points, which took the system about one and a half hours to scan. The results are shown as a three dimensional perspective in figure #9.7; figure #9.8

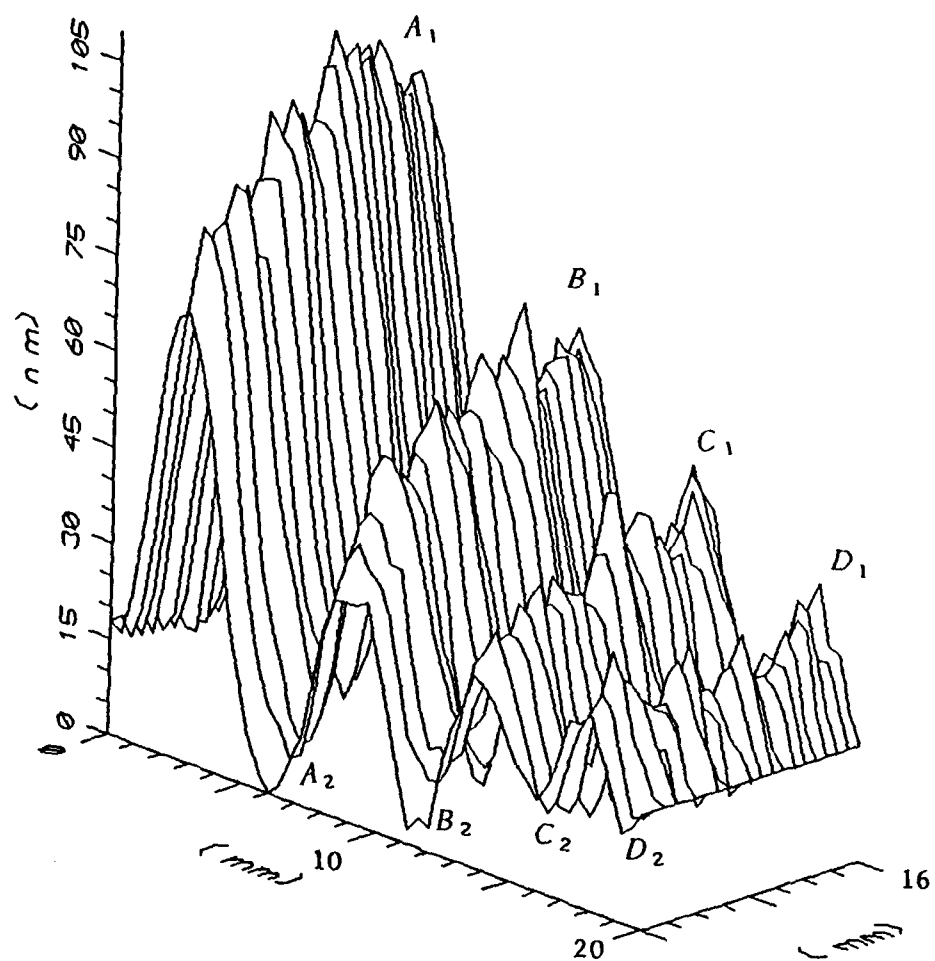


Nd:YAG collimated wavefront
Figure #9.6b



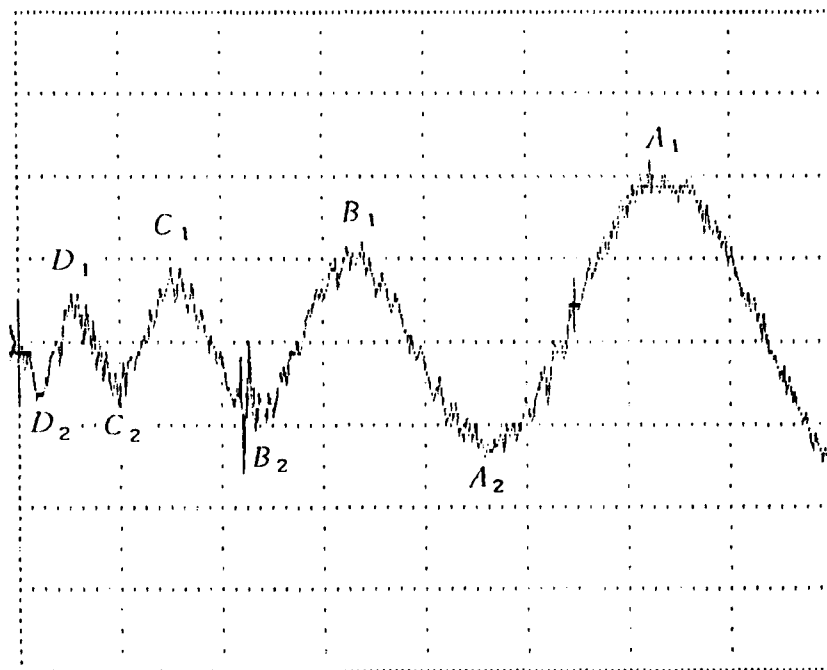
FL = 35 cm 508L
Argon collimated wavefront
Figure #9.6a

1003LET



A 20 X 16 mm mapping of a laser generated Lamb wave using heterodyne holographic interferometry.

FIGURE #9.7



Lamb wave generated with a 9 nsec pulse, 70 mJ Nd:Yag. Peaks and valleys are marked for comparison to the heterodyne holographic scan.

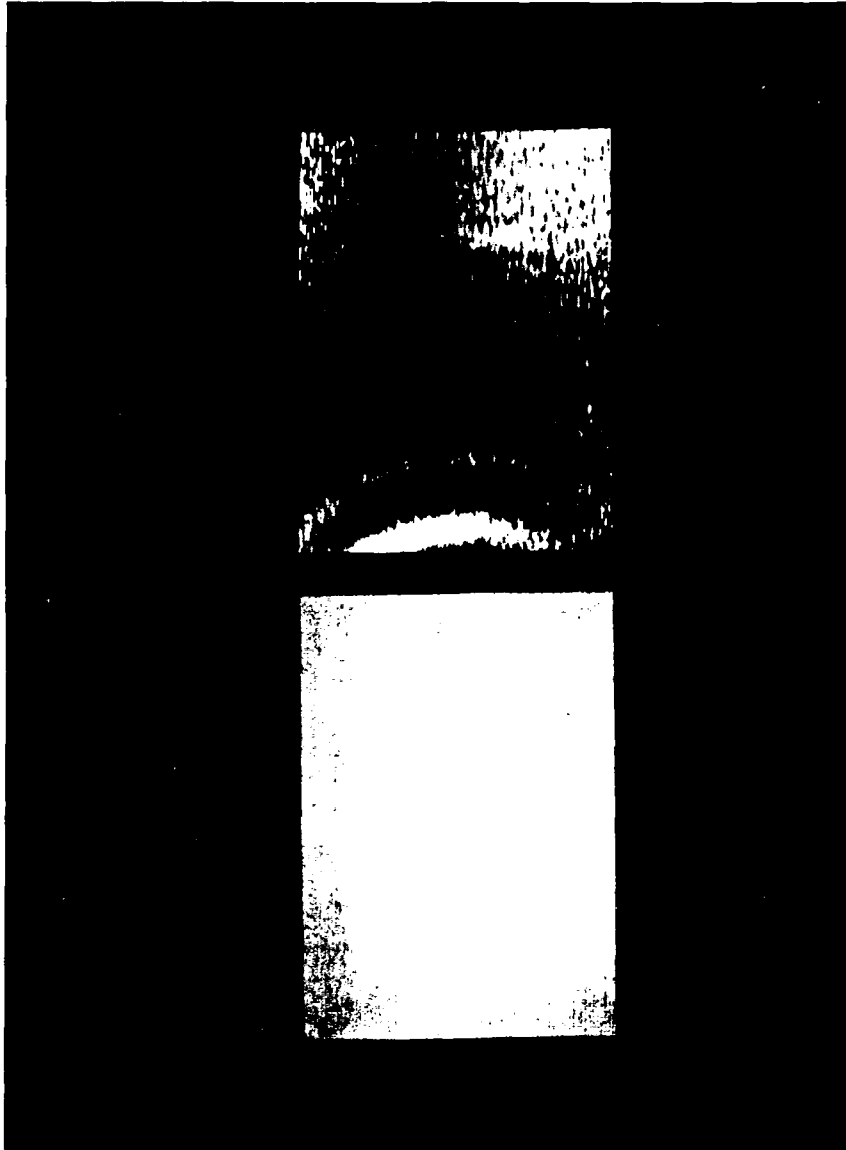
FIGURE #9.8

| Position | Fiber-Optic Interferometry Measurement | Heterodyne Holographic Interferometry Data | % Error |
|-------------|--|--|---------|
| $A_1 - A_2$ | 83.5nm | 77.2nm | 7.5 |
| $B_1 - B_2$ | 53.6nm | 41.0nm | 23.5 |
| $C_1 - C_2$ | 30.0nm | 25.7nm | 14 |
| $D_1 - D_2$ | 26.4nm | 16.4nm | 37.8 |

Table #9.1
Comparison of the Fiber-Optic Interferometry Measurements
to the Heterodyne Holographic Data

is the interferometer tracing included again for comparison. The corresponding displacement measurements for the identified peaks and valleys is given in table #9.1. In all cases, the heterodyne holographic interferometry data underestimated the out-of-plane displacements relative to the interferometer. This was expected since the finite area of the detector in the holography system acted to smooth or average the data as it scanned. The fiber-optic interferometer better approximated a point source detector.

Using quasi-heterodyne analysis the lengthy scan time involved with heterodyne analysis was avoided. The frame grabbing capabilities of quasi-heterodyne analysis reduced the data acquisition to a few seconds. The image processor then took only four to five minutes to process the comparable data. The processing routine was written in Pascal and the computing time could have been reduced further by using the machine source code. The resultant image is displayed in figure #9.9. The theoretical sensitivity for this configuration was calculated to be $\frac{\lambda}{50}$ based on the f/#-5 imaging system and a detector area of $0.22mm^2$. The experimental resolution was determined to be $\frac{\lambda}{25}$. This discrepancy probably resulted from two different problems. The first source of error involved the incomplete use of the A/D bit range of the camera. The second source of error resulted from condensation continually forming on the detector head. The camera was borrowed, so internal modifications of the camera did not seem appropriate. However, despite the shortcomings of the camera, the images in figure #9.9 adequately display the larger amplitudes of the Lamb wave and shows encouraging prospects for future endeavors.



Left: Standard holographic interferogram of the same image

Right: Image of laser-generated Lamb wave; quasi-heterodyne analysis reveals sub-fringe displacements

Figure #9.9

10 Conclusion

As previous researchers have shown, heterodyne holographic interferometry (HHI) can be a powerful technique in the accurate measurement of imaging full field object displacements. Aprahamian first demonstrated it was possible to image acoustic waves holographically. His experiments were limited to analyzing large amplitude waves, however. Gogosz showed that normal holographic interferometry could be used in imaging conventional acoustic sources, but lacked sufficient sensitivity to provide quantitative results. Six years later Dandliker developed both the technique and theoretical ability to perform HHI. Since then, various other authors have been successful at using HHI and pulsed recording systems in studying high speed events in transparent materials. Wagner was able to perform high speed HHI analysis of an acoustic wave on an opaque object, but required a mirrored surface finish. Also, his analysis was limited to a finite region (3cm in diameter) of the specimen over which there was adequate fringe visibility. Prior to this treatise, no one had yet demonstrated the use of HHI on the imaging sub-fringe acoustic waves of diffusely reflecting objects, a requirement to make HHI a practical method in ultrasonic nondestructive testing.

In this body of work, four preliminary experiments were conducted to make the final experiment possible - demonstrating the imaging of a laser generated acoustic wave with sub-fringe displacement amplitudes. The first two experiments provided confirmation of theoretical predictions. In the first, in order to use HHI in analyzing a large area it was necessary to overcome the inherent error introduced by both wavefront curvature the wavelength shift between lasers. By using precise collimating procedures and high quality optics these obstacles were overcome. The second experiment was performed to characterize the heterodyne read-out system.

This gave an accurate measure of the out-of-plane displacement resolution and the spatial sensitivity of the system used. The third experiment was necessary to demonstrate the application of holographic interferometry to the imaging of acoustic interaction with a known defect. Although large amplitude waves were used in this study, the results lead one to believe that similar analysis could be performed using HHI of sub-fringe displacements. The fourth experiment was designed to both assist in locating the wave holographically and in confirming the holographic amplitude measurement. Using all the previously acquired data, the fifth experiment was performed.

HHI has the potential to be a powerful technique in the nondestructive evaluation of materials. Current ultrasonic methods require contact with the specimen and are therefore limited by geometry. HHI would not have such a limitation. However, previous experimental obstacles have made HHI an impractical method for ultrasonic measurement on a diffusely reflecting object. The design of the fifth experiment described in this paper was able to overcome past limitations of high speed applications of HHI. The imaging of sub-fringe displacement amplitudes from pulsed holograms permit full field quantitative measurement of a standard acoustic source. Two features of this experiment could be improved upon. First, if an electro-optics switch were used in place of the diverting prism to separate the pulses, the sensitivity of the system would be doubled. Second (and more problematical) if one could create a speckle-free image, the phase sensitivity would be dependent only upon the incident power at the photo-detector rather than the statistics of a coherent diffusely reflecting object. In light of these problems, this treatise demonstrates that it is possible to use heterodyne holographic interferometry as a broad range non-contact ultrasonic measurement technique.

11 References

- A.M. Aindow, R.J. Dewhurst, D. A. Hutchins, and S.B. Palmer,
J. Acoust. Soc. Am. 69(2),(1981)
- A.M. Aindow, R.J. Dewhurst, S.B. Palmer, and C.B. Scurby, NDT International,
Dec. 1984, 329
- R. Aprahamian, D.A. Evensen, J.S. Mixson, and J.E. Wright,
Exp., Mech. 11,357 (1971)
- H. Arsenault, Opt. Comm., 4 (4), 267 (1971)
- A.N. Bonderanko, Y.B. Drobot and S. B. Kruglov, Sov. J. NDT 12, 655 (1976)
- J.E. Bowers, R.L. Jungerman, B.T. Khuri-Yakub, and G.S. Kino,
J. Lightwave Tech. Vol. LT-1, No.2, June (1983)
- J.H. Bruning, D.R. Herriott, J.E. Gallagher, D.P. Rosenfeld, A.D. White, and
D.J. Brangaccio, Appl. Opt., 13 (11), 2693, (1974)
- C.A. Calder and W.W. Wilcox, Rev. Sci. Instrum., 45(12),1557, Dec. (1974)
- C.A. Calder and W.W. Wilcox, Mat. Eval., 38, 86, (1980)
- P. Cielo, F. Nadeau and M. Lamontagne, Ultrasonics, March (1985), 55-62
- R. Crane, Appl. Opt., 8 (3), 538 (1969)
- R. Dandliker, B. Ineichen and F.M. Mottier, Opt. Comm. 9(4), 412, (1973)
- R. Dandliker and B. Ineichen, Opt. Comm, 19 (3), 365 (1976)
- R. Dandliker, E. Marom and F.M. Mottier, J Opt. Soc. Am. 66, 23-30, (1976)
- R. Dandliker, in Prog. in Optics, Vol. XVII, E. Wolf, ed. (North Holland,
Amsterdam, 1980), pp. 1-84
- R.J. Dewhurst, D.A. Hutchins, S.B. Palmer, and S.B. Scruby,
J. Appl. Phys., 53(6), June (1982)
- R.J. Dewhurst, C. Edwards, A.D. McKie, and S.B. Palmer,
Appl. Phys. Lett 51(14), 1066, (1987)
- M.J. Ehrlich, L.C. Phillips and J.W. Wagner,
Rev. Sci. Instrum, 59 (11), 2390 (1988)
- L.M. Frantz, A.A. Sawchuk, and W. von der Ohe, Appl. Opt. 18(19), 3301, (1979)
- A.A. Friesem, A. Kozma and G.F. Adams, All. Opt. 6(5), 851, (1967)
- Gabor, Nature 161, 777 (1948)

- D. Gabor, Proc. Roy. Soc., A197:454 (1949)
- D. Gabor, Proc. Roy. Soc., B64:449 (1951)
- R.M. Gagosz, "Holographic Nondestructive Testing", ed. by R.K. Erf (Academic Press 1974), pp 62-84
- L.I. Goldfischer, J. Opt. Soc Am., 55 (3), 247 (1965)
- J.W. Goodman, "Intro. to Fourier Optics", McGraw-Hill 1968
- J.W. Goodman, "Laser Speckle and Related Phenomena", ed. J.C. Dainty (Springer, Heidelberg) pp.56-81
- J.W. Goodman, "Statistical Optics", New York: Wiley, (1985)
- P. Hariharan, B.F. Oreb, and N. Brown, Appl. Opt. 22(6), 876, (1983)
- P. Hariharan, Opt. Eng., 24 (4), 632 (1985)
- E. Hecht and A. Zajac, "Optics", Addison-Wesley (1979)
- B.P. Hildebrand, K.A. Haines, J. Opt. Soc. Am., 57 (2), (1967)
- D.C. Holloway, A.M. Patacca, W.L. Fournery, Exp. Mech., 17 (8), 281 (1977)
- D.A. Hutchins, R.J. Dewhurst, and S.B. Palmer, Appl. Phys. Lett., 38(9), 677, 1 May 1981
- D.A. Hutchins and K. Lundgren, Review of Progress in Quantitative NDE, Vol. 7A, Edited by D.O. THompson & D.E. Chimenti, 79-84, Plenum Press (1988)
- D.A. Hutchins, F. Nadeau and P. Cielo, Can J. Phys. 64, 1334, (1986)
- D.A. Hutchins, Can. J. Phys. 64,1247, (1986)
- D.A. Hutchins, Physical Acoustics, Vol.XVIII, 12-123, (1988)
- R.L. Jungerman, B.T. Khuri-Yakub, and G.S. Kino, J. Acoust. Soc. Am. 73(5), 1838, May (1983)
- A. Kozma and J.S. Zelenka, J. Opt. Soc. Am. 60(1), 34, (1970)
- B.P. Lathi, "Random Signals and Communication Theory", International Textbook Company Scranton Pennsylvania (1968)
- H.M. Ledbetter & J.C. Moulder, J.Acoust. Soc. Am. 65(3), 840 (1979)
- S. Lowenthal and H. Arensault, J. Opt Soc. Am. 60, 1478 (1970)
- J.P. Monchalin, IEEE Trans. Ultra. Ferr. freq., UFFC-33(5),495 (1986)
- C.H. Palmer and R.E. Green, Appl. Opt. 16, 2333, (1977)

- J.F. Ready, J. Appl. Phys. 36(2),462, Feb 1965
- I.S. Reed, IRE Trans. Info. Theory, IT-8, 194, (1962)
- L.R F. Rose, J. Acoust. Soc. Am. 75(3),723, March 1984
- J.L. Rose and A. Pilarski, Mat. Eval., 46,598, April (1988)
- J.Schwider, R. Burow, K.-E. Elssner, J. Grzanna, R. Spolaczyk, and K. Merkel, Appl Opt, 22 (21), 3241 (1983)
- U. Schleicher, M. Paul, B. Hoffmann, K.J. Langenberg and W. Arnold, Proc. Photoacoustic and Photothermal Inter., July 27-30 (1987), edited by P. Hess & J Delzl (Springer Verlag, 1988)
- C.B. Scruby, R.J. Dewhurst, D.A. Hutchins, and S.B. Palmer, Res. Tech in NDT, vol. V, 281-327, (1982)
- C.B. Scruby, R.J. Dewhurst, D.A. Hutchins, S.B. Palmer, J. Appl. Phys., 51(12), 6210, (1980)
- H. Sontag and A.C. Tam, IEEE Trans. Utras. Ferr. Freq. Contr. UFFC-33,500 (1986)
- R. Thalmann and R. Dandliker, J. Opt. Soc. Am. A, 3(7), 972, (1986)
- I.A. Viktorov, "Rayleigh and Lamb Waves", Plenum Press New York 1967
- J.W. Wagner, Mat. Eval., 44, Sept (1986), 1238-1243
- J.W. Wagner, Phd. Dissertation, The Johns Hopkins University (1984)
- J.W. Wagner, Appl. Opt. 25,3159 (1986)
- R.M. White, J. Appl. Phys. 34(12),3559, Dec 1963
- J.C. Wyant, Appl. Opt., 14 (11), 2622 (1975)
- J.S. Zelenka and J.R. Varner, Appl. Opt., 7 (10), 2107 (1968)

12 Appendix

c Program SCAN.FOR

c
c
c
c
c
c
c
c
c
c

This program uses the AT&T 6300 for scanning control of the Newport 855 actuators and data acquisition from the HP 3478A multimeter over the GPBI interface. The GPIB was manufactured by Metrabyte and it is not recommended by this user.

character*50 linex
character*25 msg,echo1,echo2,msg1
character*12 fname,vel,step1,step2
character dvm(15),dec1,dec2
integer num1,num2,row,col,icheck,flg
real data

c

flg = 0

c

c INITIALIZE SYSTEM

c

write (*,'(A/)',) ' Do you need to initialize '
write (*,'(A/)',) ' the system ?'
write (*,'(A/)',) ' y = yes n = no'
read (*,'(A/)',) msg
if (msg.eq.'n') goto 90
call init (msg1,echo1,echo2,flg)
linex = ' initialization ERROR'
if (flg.ne.0) goto 8000

c

c

90 write (*,'(A/)',) ' Do you need new'
write (*,'(A/)',) ' scanning parameters?'
read (*,'(A/)',) dec2
if (dec2.eq.'n') go to 200

c

c Input Movement Parameters

c

100 call param(step1,step2,num1,num2,vel)

c

c Send data to the 855

c

call send855 (vel,echo1,flg)
linex = ' send velocity error'
if (flg.ne.0) goto 8000
write (*,610) vel,echo1

c

call send855 (step1,echo1,flg)

```

        linex = ' send step1 error'
        if (flg.ne.0) goto 8000
        write (*,610) step1,echo1
c
        call send855 (step2,echo1,flg)
        linex = ' send step2 error'
        if (flg.ne.0) goto 8000
        write (*,610) step2,echo1
c
c
200    icheck = 0
c
c ENTER FILE NAME
c
        write (*,'(A/)') ' Specify filename '
        read (*,'(A)') fname
        open (3,FILE=fname,ACCESS='SEQUENTIAL',STATUS='NEW')
c
c
c
300    do 700 i = 1,num1
c
c
c Take data from HP
c
        call readhp (dvm,flg)
        call trans (dvm,data)
        write (*,660) i,icheck
        write (*,600) data
        write (3,640) data
c
c Increment Horizontal Position
c
        msg = "I1"
        call send855 (msg,echo1,flg)
c
c PAUSE
c
        nsec = 7
        call ppause (nsec)
c
600    format (' data =',F8.4,/)
610    format (2x,A12,A25)
620    format (2x,2A25)
640    format (F8.4,)
660    format (' i =',I3,'  icheck =',I3)
c
c
c
700    continue
c
c

```

c Take data from HP

```
c
    call readhp (dvm,flg)
    call trans (dvm,data)
    icheck = icheck + 1
    write (*,660) i,icheck
    write (*,600) data
    write (3,640) data
```

c
c check vertical increment

```
c
    if (icheck.le.num2) then
        msg = "H1"
        call send855 (msg,echo1,flg)
        write (*,620) msg,echo1
```

```
c
        msg = "I2"
        call send855 (msg,echo1,flg)
        write (*,620) msg,echo1
        nsec = 35
        call ppause (nsec)
        goto 300
```

```
    else
    endif
```

c
c
c Send actuators home

```
    msg = "H2"
    call send855 (msg,echo1,flg)
    write (*,620) msg,echo1
```

```
c
    msg = "H1"
    call send855 (msg,echo1,flg)
    write (*,620) msg,echo1
```

c
c
c print info

```
    row = num2 + 1
    col = num1 + 1
    write (*,850) row,col,fname
850    format (2x,I4,' rows and',I4,' columns in ',A12)
```

c
c SCAN AGAIN ???

```
c
    write (*,'(A/)') 'Do you wish to scan again?'
    write (*,'(A/)') ' y = yes n = no'
    read (*,'(A)') decl
    if (decl.eq.'y') then
        write (*,'(A/)') 'Do you need new'
        write (*,'(A/)') 'scanning parameters?'
        write (*,'(A/)') 'and'
        write (*,'(A/)') 'please wait for the actuators'
```

```

        write (*,'(A/)',) to return home before'
        write (*,'(A/)',) answering'
        read (*,'(A)') dec2
        if (dec2.eq.'y') then
            goto 100
        else
            goto 200
        endif
    endif
else
endif
c
    goto 9000
8000 write (*,8010) linex
8010 format (A50)
c
c query did not work consistently
c
c    call query (msg,echo2,flg)
c    write (*,630) echo1,echo2
c
9000 continue
c
c
c    stop
c    end
c
c
c-----
c
c
c
c    subroutine init (msg1,echo1,echo2,flg)
c
c
c
c    integer*2 flg,brd,ivar,delay
c    character*127 syscon,remote,out855,linex
c    character*25 msg,echo1,rec855,echo2,tout
c
c    character*25 HPmsg,msg1,recvhp,outhp,clear
c
c
c    delay = 100
c    brd = 0
c    flg = 0
c    ivar = 0
c    syscon = "SYSCON MAD=3, CIC=1, NOB=1, BA0=896"
c    remote = "REMOTE 17,21"
c    tout = "TIMEOUT"
c
c
c    out855 = "OUTPUT 17[$+]"
c    rec855 = "ENTER 17[$]"
c    msg = "Q2"

```



```

        echo1 = '          '
        echo2 = '          '
c
        clear = "CLEAR 21"
        outhp = "OUTPUT 21[$]"
        HPmsg = "F1R0N3"
        recvhp = "ENTER 21[$]"
        msg1 = '
c
c Initialization
c
        call ie488 (syscon,ivar,flg,brd)
        linex = syscon
        if (flg .ne. 0) goto 5000
c
c Remote 855 address 17,21
c
        call ie488 (remote,ivar,flg,brd)
        linex = ' remote'
        if (flg .ne. 0) goto 5000
c
c USE TIMEOUT FEATURE
c
        call ie488 (tout,delay,flg,brd)
        linex = ' timeout'
        if (flg .ne. 0) goto 5000
c
c Output "F1RAN4" to HP
c      set-up for taking data
c
        call ie488 (outhp,HPmsg,flg,brd)
        linex = ' outhp initialize'
        if (flg .ne. 0) goto 5000
c
c Enter data from HP 3478A
c
        call ie488 (recvhp,msg1,flg,brd)
        linex = ' enter hp initialize'
        if (flg .ne. 0) goto 5000
c
c Clear HP
c
        call ie488 (clear,ivar,flg,brd)
        linex = ' clear'
        if (flg .ne. 0) goto 5000
c
c
c      Output to 855
c
c
        call ie488 (out855,msg,flg,brd)
        linex = ' out855 init'

```

```

        if (flg .ne. 0) goto 5000
c
c Enter data from controller
c
        call ie488(rec855,echo1,flg,brd)
        linex = ' enter1 init'
        if (flg .ne. 0) goto 5000
c
c Enter data from controller
c
        call ie488(rec855,echo1,flg,brd)
        linex = ' enter1a init'
        if (flg .ne. 0) goto 5000
c
c Enter data from controller
c
        call ie488(rec855,echo2,flg,brd)
        linex = ' enter2 init'
        if (flg .ne. 0) goto 5000
c
        write (*,'(A\\)') ' Initialization complete'
c
        go to 9000
5000 write (*,'(A\\)') linex
        write (*,'(i7)') flg
9000 continue
        return
        end
c
c
c-----
c
c
c
        subroutine send855 (msg,echo1,flg)
c
c
c
        integer*2 flg,brd
        character*127 out855,linex
        character*25 msg,echo1,rec855
c
c
c
        brd =0
        flg =0
        out855 = "OUTPUT 17[$+]"
        rec855 = "ENTER 17[$]"
        echo1 = '
c
c Output to 855
c
        call ie488 (out855,msg,flg,brd)

```

```

        linex = ' SEND855 output error '
        if (flg .ne. 0) goto 5000
c
c Enter data from controller
c
        call ie488(rec855,echo1,flg,brd)
        linex = ' SEND855 input error'
        if (flg .ne. 0) goto 5000
c
c
c
        go to 9000
5000    write (*,'(A\\)') linex
        write (*,'(i7)') flg
9000    continue
        return
        end
c
c
c-----
c
c
c      subroutine readhp (dvm,flg)
c
c
c      character*25 recvhp,linex,clear,outhp,HPmsg
c      integer*2   flg,brd,ivar
c      character    dvm(15)
c
c
c      ivar = 0
c      brd = 0
c      flg = 0
c      clear = "CLEAR 21"
c      outhp = "OUTPUT 21[$]"
c      HPmsg = "F1R0N3"
c      recvhp = "ENTER 21[$]"
c
c
c      do 10 i=1,15
c          dvm(i) = ''
10      continue
c
c Output "F1R0N4" to HP
c      set-up for taking data
c
c      call ie488 (outhp,HPmsg,flg,brd)
c      linex = ' outhp error'
c      if (flg .ne. 0) goto 5000
c
c Enter data from HP 3478A
c

```

```

      call ie488 (recvhp,dvm,flg,brd)
      linex = ' enter hp'
      if (flg .ne. 0) goto 5000
c
c
c
      call ie488 (clear,ivar,flg,brd)
      linex = ' clear'
      if (flg .ne. 0) goto 5000
c
c
c
      goto 9000
5000 write (*,'(A\\)') linex
      write (*,'(i7)') flg
9000 continue
      return
      end
c
c
c-----
c
c
c
      subroutine trans (dvm,data)
c
c
c      dimension x(6)
      character dvm(15)
c
c
c
      data = 0.0
c
      do 500 i=1,6
c
      if (dvm(i).eq.'+') x(i) = 1.0
      if (dvm(i).eq.'-') x(i) = -1.0
      if (dvm(i).eq.'1') x(i) = 1.0
      if (dvm(i).eq.'2') x(i) = 2.0
      if (dvm(i).eq.'3') x(i) = 3.0
      if (dvm(i).eq.'4') x(i) = 4.0
      if (dvm(i).eq.'5') x(i) = 5.0
      if (dvm(i).eq.'6') x(i) = 6.0
      if (dvm(i).eq.'7') x(i) = 7.0
      if (dvm(i).eq.'8') x(i) = 8.0
      if (dvm(i).eq.'9') x(i) = 9.0
      if (dvm(i).eq.'0') x(i) = 0.0
c
500  continue
c
c
c

```

```

data = x(2)
data = data + (x(4) * 0.1)
data = data + (x(5) * 0.01)
data = data + (x(6) * 0.001)
data = ((data * x(1)) + 1.8) * 100.
c
c
return
end
c
c
c-----
c
c
subroutine param(step1,step2,num1,num2,vel)
c
c
character*11 vel,step1,step2
integer num1,num2
c
write (*,120)
write (*,(A/)) ' input the step size for actuator #1'
write (*,(A/)) ' as "S1nn.nnnn" including the'
write (*,(A/)) ' QUOTES'
read (*,(A/)) step1
write (*,120)
write (*,(A/)) ' enter the number of incremental '
write (*,(A/)) ' steps for actuator #1'
read (*,110) num1
write (*,120)
write (*,(A/)) ' input the step size for actuator #2'
write (*,(A/)) ' as "S2nn.nnnn"'
read (*,(A/)) step2
write (*,120)
write (*,(A/)) ' enter the number of incremental '
write (*,(A/)) ' steps for actuator #2'
read (*,110) num2
write (*,120)
write (*,(A/)) ' input the scanning velocity'
write (*,(A/)) ' "V0.nnnn"'
read (*,(A/)) vel
110 format (I7)
120 format (//)
c
return
end
c
c
c-----
c
c
subroutine query (msg,echo1,flg)

```

```

c
c
c
    integer*2 flg,brd
    character*127 out855,linex
    character*25 msg,echo1,echo1a,rec855
c
c
c
    brd =0
    flg =0
    out855 = "OUTPUT 17[$+]"
    rec855 = "ENTER 17[$]"
    echo1 = '
    echo1a = '
c
c Output to 855
c
    call ie488 (out855,msg,flg,brd)
    linex = ' QUERY output error'
    if (flg .ne. 0) goto 5000
c
c Enter data from controller
c
    call ie488(rec855,echo1a,flg,brd)
    linex = ' QUERY input error 1'
    if (flg .ne. 0) goto 5000
c
c Enter data from controller
c
    call ie488(rec855,echo1,flg,brd)
    linex = ' QUERY input error 2'
    if (flg .ne. 0) goto 5000
c
c
c
    go to 9000
5000 write (*,'(A\\)') linex
    write (*,'(i7)') flg
9000 continue
    return
    end
c-----
c
c
c
    subroutine ppause (nsec)
c
    integer nsec,ksec
c
c
c
    do 200 i = 1,nsec

```

```
do 100 j = 1,14300
x = 1*1
100 continue
200 continue
return
end
```

Vita

Louis Carlyle Phillips was born on March 9, 1958 in Louisville, Kentucky. He graduated from Jeffersontown High School in Jeffersontown, Kentucky in 1976 and received a Bachelors of Electrical Engineering degree from Purdue University in 1981. During his undergraduate career, he was part of the cooperative education program at Purdue University and was employed by first the Ophthalmology Department of the University of Louisville Medical School and subsequently by the Center for Medical Device Analysis. Since 1981, he has been a full time graduate student in the Materials Science and Engineering Department at The Johns Hopkins University, where in 1985, he received a Master of Science Degree.